

MR IMAGING OF UVEAL MELANOMA AND ORBIT

TERESA GONÇALVES FERREIRA



**MR IMAGING OF
UVEAL MELANOMA AND ORBIT**

Teresa Gonçalves Ferreira

Colophon

Cover designed by: Sara Antunes | saraantunesc@gmail.com

Layout designed by: Wouter Aalberts | wouter@persoonlijkproefschrift.nl

Printed by: Ridderprint | www.ridderprint.nl

ISBN: 978-94-6483-106-1

Copyright © 2023, Teresa Gonçalves Ferreira

All rights reserved. No part of this book may be reproduced, stored in a retrieval system, or transmitted in any form or by any means, electronic, mechanical, photocopying, recording, or otherwise, without the prior written consent of the author.

Financial support for the printing of this thesis was provided by Stichting Leids Oogheelkundig Ondersteuningsfonds, Stichting Blindenbelangen, Stichting Blindenhulp, Landelijke Stichting voor Blinden en Slechtzienenden, Sectra and Chipsoft.

MR IMAGING OF UVEAL MELANOMA AND ORBIT

Proefschrift

ter verkrijging van
de graad van doctor aan de Universiteit Leiden,
op gezag van rector magnificus prof.dr.ir. H. Bijl,
volgens besluit van het college voor promoties
te verdedigen op dinsdag 27 Juni 2023
klokke 15.00 uur

door

Teresa Gonçalves Ferreira
geboren te Lissabon, Portugal

Promotoren: Prof dr AG Webb
Prof dr GPM Luyten

Copromoter: dr JWM Beenakker

Promotiecommissie: Prof dr M van Buchem
Prof dr ir MJP van Osch
Dr THK Vu
Prof dr JW Casselman (AZ Sint-Jan Brugge)
Prof dr JF Kiilgaard (Rigshospitalet Kopenhagen)

For my grandmother Ilda

CONTENTS

Chapter 1	Introduction, aims and outline of the thesis	9
1.1	History of ocular imaging	11
1.2	Personal background	11
1.3	Aims and outline of the thesis	12
1.4	Uveal melanoma	12
1.5	Orbital inflammation	15
1.6	Eyelid	16
Chapter 2	Uveal melanoma	19
2.1	MRI of uveal melanoma <i>Cancers 2019; 11(3):377</i>	21
2.2	MR imaging characteristics of uveal melanoma with histopathological validation <i>Neuroradiology 2022; 64(1):171-184</i>	45
Chapter 3	Orbital inflammation	67
3.1	CT and MR imaging in the diagnosis of scleritis <i>American Journal of Neuroradiology 2016; 37(12):2334-2339</i>	69
3.2	CT and MR imaging of orbital inflammation <i>Neuroradiology 2018; 60(12):1253-1266</i>	87
Chapter 4	Eyelid	
4.1	MR and CT imaging of the normal eyelid and its application in eyelid tumors <i>Cancers 2020; 12(3):658</i>	113
Chapter 5	Summary, discussion, future perspectives and conclusion	135
5.1	Uveal melanoma	137
5.2	Orbital inflammation	141
5.3	Eyelid	143
	Nederlandse samenvatting	151
	Acknowledgements	157
	List of publications	159
	Curriculum Vitae	161

1

Introduction, aims and outline of the thesis



1.1 HISTORY OF OCULAR IMAGING

While the eyelid and anterior part of the eye are easily accessible to physical examination, the inside and posterior part of the eye, as well as the retrobulbar structures are inaccessible to clinical observation.

In 1847, Charles Babbage, an English mathematician, developed an instrument thought to resemble an ophthalmoscope, but it was in 1851 that the ophthalmoscope was invented by Hermann von Helmholtz, a German physician and physicist. This revolutionized the field of ophthalmology, as it made feasible the examination of the inside of the eye. Intra-ocular masses, the retina and retinal vessels, and the optic disc could then be evaluated. The possibility of visualizing the retinal vasculature is unique in the human body, and has the advantage that it can reveal impending systemic or cerebrovascular disease [1,2]. Likewise, the retina and optic disc are the only portions of the central nervous system we can observe noninvasively.

In 1895, Wilhelm Conrad Roentgen, a German mechanical engineer and physicist, invented X-ray roentgenography, which was grasped immediately by the medical community. However, the first real uses of X-ray by the ophthalmic community were only in 1912 [3].

In 1956, Ian Donald, an English obstetrician, together with engineer Tom Brown, invented ultrasound (US), and in that same year the first application of diagnostic ultrasound in the eye was reported [4].

In 1971 magnetic resonance imaging (MRI) was invented by an American chemist, Paul Lauterbur. A year later, in 1972 computer tomography (CT) was invented by Godfrey Hounsfield, an English engineer, and by Allan Cormack, a South Africa-born physicist working in Massachusetts. Ophthalmologists soon got interested in CT and MRI, with the first articles where CT and MR images of the orbit were published in 1977 [5] and 1983 [6], respectively.

Since the development of US, CT and MRI, improvements in these techniques have led to important progress in ophthalmologic imaging [7,8].

1.2 PERSONAL BACKGROUND

Before the start of this research project, CT and MRI were already widely used to evaluate the orbit, CT being the first line in trauma and infection, MRI being preferred for orbital masses. However, the MRI protocol consisted only of anatomical T1 and T2 weighted images (WI), and often no distinction between the benign or malignant etiology of an orbital lesion was possible.

Concerning ocular masses, in a way ophthalmologists have been ahead compared with other disciplines, being able to assess them well with optical techniques and ultrasound,

and therefore for a long time they did not need more complicated, and non-optimized MRI. However, before we started our research, retinoblastomas were already being assessed with MRI, with high-resolution images obtained with a child under general anesthesia or sedated [9]. But in an awake patient, besides the magnetic susceptibility effects at the air-bone interface, eye motion is also a challenge [10], and before this current research project, due to non-optimized protocols, uveal melanoma was seldom evaluated with MRI. Similarly, no optimized protocol to evaluate the eyelid was available, and as a result MRI was rarely performed to characterize eyelid lesions.

In 2008 I was invited by Alexandra Borges to give a lecture about MRI of the orbit and eye on the Erasmus Course on Magnetic Resonance Imaging which was held in Lisbon. There began my passion for the orbit. I started collating orbital pathology. I kept participating in several Congresses and Courses giving lectures about the orbit and the eye, mainly concerning MRI. All this triggered my interest in the field of orbital research. And agreeing with Juan M. Taveras, a Dominican neuroradiologist, who could be considered the father of neuroradiology:

“We have a responsibility not only to get the best results in a given case but also to advance the field, and this requires continuing research”.

In: Taveras J. M.: International neuroradiology symposium on preoperative embolization. AJNR. 7 (1986) 926.

1.3 AIMS AND OUTLINE OF THE THESIS

The main aims of the research described in this thesis are first, to implement MRI as a diagnostic imaging technique in uveal melanoma (UM), by developing a dedicated eye MRI protocol and extensively evaluating the MR imaging characteristics of UM. Second, to improve the diagnosis and differential diagnosis on imaging of orbital inflammation. Finally, to further develop the dedicated eye MRI protocol into a protocol dedicated for the eyelid and assess whether the different eyelid layers are possibly to identify on MRI (as well as CT), in order to improve the evaluation of the local extension of an eyelid tumor. This thesis is therefore divided in three different parts: the first part regards uveal melanoma, the second part orbital inflammation, and the third part the eyelid.

1.4 UVEAL MELANOMA

The first part of this thesis concerns uveal melanoma, the most common primary malignant ocular tumor in adults [11-14]. In the past, enucleation was the main treatment, but over the last decades various eye- and vision-saving treatments have become available, including

episcleral brachytherapy, proton beam radiotherapy and stereotactic radiotherapy [12,13]. Despite the significant progress in the management of uveal melanoma its prognosis has only slightly improved, 20% of patients dying of metastatic disease within 10 years [15].

The ideal imaging technique for the evaluation of UM needs firstly to aid to differentiate UM from other intra-ocular lesions. Secondly, it needs to be capable to accurately delineate the limits of the tumor and to measure them, since these are the main determinants for the choice of the type of treatment, and in case of radiotherapy for the radiotherapy planning. Thirdly, noninvasive markers that can predict treatment response and prognosis are needed [13,16] in order to adjust the frequency and type of screening according to whether the patient is at high or low risk of developing disseminated disease, and because even if a biopsy is performed, it may be not representative, due to UM being heterogeneous in terms of chromosomal aberrations [17,18]. Finally, it should be able to early assess tumor response to radiotherapy. Ultrasound, ultrasound biomicroscopy, fundoscopy, fluorescein angiography, indocyanine green angiography and optical coherence tomography are the most frequently used techniques to evaluate UM for the diagnosis, pre-treatment planning, and follow-up after radiotherapy [13,14]. Based on these techniques, an ophthalmologist specialized in ocular oncology can make the diagnosis of UM in 95% of cases, and therefore the diagnosis of UM is generally not verified by cytological or histopathological examination, which is unique among cancers. However, diagnosis with these conventional ophthalmic imaging modalities is difficult in smaller uveal melanomas/melanocytic lesions, in atypical tumors, in lesions behind the iris and in case of opacification of the ocular media. Furthermore, US has limitations in pre-treatment planning of UM and during follow-up, only being able to evaluate dimensional changes of the lesion.

Another option for imaging the globe is magnetic resonance imaging, which has been challenging because of eye motion and/or magnetic susceptibility effects at the air-bone interface [10,19]. However, recent developments on MRI, have made it a promising diagnostic imaging modality in ophthalmology, due to its excellent soft tissue contrast and spatial resolution, as well as the possibility to generate 3D volumetric and functional images such as diffusion weighted-imaging (DWI) and perfusion weighted-imaging (PWI), and MR was increasingly being used to evaluate uveal melanoma. Clinical MR protocols were, however, not optimized for ocular masses and therefore lacked the quality for accurate assessments.

Jan-Willem Beenakker is a physicist specialized in ophthalmic MRI, who works both for the Ophthalmology and Radiology Departments in LUMC. He developed a new MRI-based method at the 7T MRI to quantitatively characterize the full three-dimensional retinal shape, which is useful for refractive surgery and will ultimately lead to the development of a new type of intra-ocular lens for cataract treatment [20]. This offered new ophthalmologic possibilities, such as for the characterization of UM with MRI [21]. As the LUMC is the National Reference

Center for UM in The Netherlands, it was logical to start evaluating UM with MRI. At this point, as a neuro and head and neck radiologist with a special interest in orbit and eye, I got involved, as suggested by Mark van Buchem, and started, together with Jan-Willem Beenakker and the ophthalmologists, to develop a dedicated eye MRI protocol to evaluate UM.

Technical/clinical developments in radiology are not easy. Back in 1975, the remarkable and inspiring Italian American neuroradiologist, Giovanni di Chiro stated:

“Only “innocent” practitioners, however, may delude themselves that the age of easy radiographic diagnosis has arrived”.

In: DI CHIRO G.: Of CAT and other beasts (editorial). AJR. 122 (1975) 659-61.

And indeed, the creation of this dedicated UM MRI protocol would not be easy.

Our first developments of high-resolution ocular MRI were performed at 7 Tesla (7T) because its high-field strength enabled an increased signal-to-noise ratio (SNR) and spatial resolution without an increase in acquisition time. Furthermore, this research-orientated 7T MRI provided the platform needed to develop new acquisition strategies to resolve eye-specific challenges, such as eye-motion and an inhomogeneous magnetic field present in the orbit [21]. In a group of UM patients where there were doubts about the conventional US measurements, the 3D evaluation of the tumor with 7T MRI had a direct implication on the chosen therapy, enabling eye-preserving therapy in 2 of the 10 included patients [12]. This supported our idea that MRI would have an important role in the evaluation of UM. Also, from a diagnostic point of view, the additional information available via MRI, in terms of location, dimensions and local extension, was proving to be very useful for the ophthalmologists. As a result, an increasing number of UM patients started receiving an MR, either as part of their clinical care or in the context of scientific studies.

Despite our progressions at ocular MRI at 7T, with often beautiful high-resolution T1 and T2-WI achieved and being able to perform dynamic contrast-enhanced perfusion (DCE), severe artefacts were sometimes hindering the evaluation of tumor and sclera limits and we were not successful to perform clinically valuable DWI of the globe. Moreover, as a clinical neuro and head and neck radiologist, I thought we should translate these ocular techniques to 3 Tesla (3T) MRI, as it would make ocular MRI more accessible to regular clinical care. This was the beginning of my research in uveal melanoma resulting in this thesis. In **chapter 2.1**, using our experience on 7T, I developed a dedicated eye 3T MRI protocol for uveal melanoma, including both anatomical and functional scans. This protocol would be suitable to evaluate not only UM but also other ocular lesions.

Once having a dedicated eye MRI protocol for uveal melanoma, the MRI characteristics of UM needed to be evaluated, due to their importance at diagnosis, but also to their

clinical implications for treatment planning, and potentially being able to provide prognostic information. However, until then, the evaluation of the MR characteristics of UM had been scarce, with few original studies addressing it and with no full evaluation of UM characteristics with MRI performed, including diffusion and quantifiable perfusion parameters. As a result, the added value of MRI was not known in many centers, UM being frequently only evaluated with ultrasound. In **chapter 2.2** the MRI characteristics of UM were comprehensively assessed. This evaluation included not only anatomical parameters, such as the origin, configuration, signal intensities on T1- and T2-weighted images (WI), dimensions, local extension and presence of retinal detachment, but also functional parameters, such as the apparent diffusion coefficient (ADC) and quantifiable perfusion characteristics. Furthermore, the clinical parameters related to treatment and/or prognostication, such as tumor dimensions, pigmentation and involvement of nearby structures, were compared between MRI and conventional ophthalmic techniques, including fundoscopy and US. These findings were validated with histopathology when available. Finally, attention was given to potential MRI prognostic markers, which would help to identify high-risk UM.

1.5 ORBITAL INFLAMMATION

The second part of this thesis regards orbital inflammation. Scleritis is an inflammation or infection of the sclera. It is a rare, often treatable vision-threatening condition. Correctly diagnosing scleritis is important given the potential for complications, the frequent association with systemic disease, of which scleritis might be the presenting manifestation [22,23], and in order not to misdiagnose it as a malignant tumor which can lead to unnecessary enucleations [24-26]. Clinical assessment and ultrasonography are the criterion standards in diagnostic imaging of this condition, but are often insufficient, with posterior scleritis being one of the most underdiagnosed diseases in ophthalmology [27]. Moreover, sonography is of limited value in evaluating other intraorbital structures, often involved in the presence of scleritis. The use of CT and MRI could potentially improve the diagnostic accuracy of scleritis, but studies on the diagnostic value of these imaging techniques on scleritis have been lacking. In **chapter 3.1**, the role of CT and MRI in the diagnosis of scleritis was evaluated, emphasizing the array of CT and MR imaging findings in scleritis.

Orbital inflammation can involve different anatomical orbital structures and it can be idiopathic or in the context of a specific disease. The diagnosis of orbital inflammation is made through combining the radiological findings, laboratory data and characteristics of other organ involvement, and if the diagnosis still remains unclear, then tissue characterization is needed. Possibly due to the fact that no systematic evaluation of orbital inflammation on CT and MRI had been published, imaging findings of orbital inflammation are often mistaken for

infection and tumor [28-32] and their underlying inflammatory disease is often overlooked. This often delays the adequate treatment and it can lead to unnecessary biopsies/enucleations. It was important to improve the diagnosis and treatment of orbital inflammation. In **chapter 3.2** the imaging protocols and characteristics of orbital inflammation were reviewed and a systematic approach for the radiological evaluation of these patients was proposed.

1.6 EYELID

The third and final part of this thesis regards the eyelid. Diseases of the eyelid are easily accessible to the ophthalmologist, making the diagnosis straightforward or easily determined with a biopsy. The treatment planning of eyelid malignancies is based on the tumor-node-metastasis (TNM) staging system, with the T-staging including determination of tumor dimensions, the invasion of eyelid structures such as the tarsal plate and orbital septum, and the invasion of nearby structures namely the orbit, globe, lacrimal sac/nasolacrimal duct, orbital walls, paranasal sinuses and brain [33-35]. The evaluation of deeper extensions in the orbit, globe, orbital walls, paranasal sinuses and brain has already been investigated and published. However, normal eyelid MRI anatomy had rarely been published, possibly because of being challenging, and therefore it was not known whether the different layers of the eyelid were possible to identify. The invasion of the tarsal plate and of the orbital septum has however direct clinical implications. On the one hand, in a tumor confined to the eyelid, which is treated with local resection and reconstructive surgery [33,36,37], knowledge about the presence of tarsal invasion preoperatively can be indispensable in planning surgical reconstruction and adequate information cannot be obtained solely by physical examination. On the other hand, when orbital invasion is present, an orbital exenteration must be considered [37-39]. The visualization of these small anatomical structures in the eyelid, both on MRI and CT, is therefore crucial in order to evaluate whether they are invaded by an eyelid tumor, not clinically accessible, and needed to be investigated. Strangely, unlike the other head and neck tumors, for eyelid malignancies T-staging according to TNM staging system is based on clinical evaluation only, which is clearly insufficient. American Joint Committee (AJCC) staging system regarding the T-staging already considers CT for evaluating extension inside the orbit, nasal cavity, paranasal sinuses and skull base, and MRI for perineural spread. Both TNM and AJCC do not consider image for evaluation of tumor extension inside the eyelid [34,35]. In **chapter 4.1** the normal eyelid anatomy on MRI and CT was evaluated, and knowledge gained subsequently applied to the evaluation of the extension of eyelid tumors and validated via histopathology.

REFERENCES

1. Rim TH, Teo AWJ, Yang HHS, Cheung CY, Wong TY. Retinal vascular signs and cerebrovascular diseases. *J Neuroophthalmol*. 2020 Mar;40(1):44-59.
2. Grein H-J. What do retinal vessels reveal about systemic disease? Retinal vessels and systemic disease - basic findings. *Coll Antropol*. 2013 Apr;37 Suppl 1:71-74.
3. Tawfik HA, Abdelhalim A, Elkafrawy MH. Computed tomography of the orbit – a review and an update. *Saudi J Ophthalmol*. 2012 Oct;26(4):409-418.
4. Lizzi FL, Coleman DJ. History of ophthalmic ultrasound. *J Ultrasound Med*. 2004 Oct;23(10):1255-1266.
5. Hollenhorst Jr RW, Hollenhorst Sr RW, MacCarty CS. Visual prognosis of optic nerve sheath meningiomas producing shunt vessels on the optic disk: the Hoyt-Spencer syndrome. *Trans Am Ophthalmol Soc*. 1977;75:141-163.
6. Moseley I, Brant-Zawadski M, Mills C. Nuclear magnetic resonance imaging of the orbit. *Br J Ophthalmol*. 1983 Jun;67(6):333-342.
7. Mafee MF, Karimi A, Shah JD, Rapoport M, Ansari SA. Anatomy and pathology of the eye: role of MR imaging and CT. *Magn Reson Imaging Clin N Am*. 2006 May;14(2):249-270.
8. de Keizer RJ, Vielvoye GJ, de Wolff-Rouendaal D. Nuclear magnetic resonance imaging of intraocular tumors. *Am J Ophthalmol*. 1986 Oct 15;102(4):438-441.
9. de Graaf P, Goricke S, Rodjan F, Galluzzi P, Maeder P, Castelijns JA, Brisse HJ. Guidelines for imaging retinoblastoma: imaging principles and MRI standardization. *Pediatr Radiol*. 2012 Jan; 42(1):2-14.
10. Lemke, A.-J.; Alai-Omid, M.; Hengst, S. A.; Kazi, I.; Felix, R. Eye imaging with a 3.0-T MRI using a surface coil – a study on volunteers and initial patients with uveal melanoma. *Eur Radiol*. 2006 May; 16(5):1084–1089.
11. Weis E, Salopek TG, McKinnon JG, Larocque MP, Temple-Oberle C, Cheng T, McWhae J, Sloboda R, Shea-Budgell M. Management of uveal melanoma: a consensus-based provincial clinical practice guideline. *Curr Oncol*. 2016 Feb;23(1):e57-64.
12. Beenakker J-WM, Ferreira TA, Soemarwoto KP, Genders SW, Teeuwisse WM, Webb AG, Luyten GPM. Clinical evaluation of ultra-high-field MRI for three-dimensional visualisation of tumour size in uveal melanoma patients, with direct relevance to treatment planning. *MAGMA*. 2016 Jun;29(3): 571–577.
13. Foti PV, Longo A, Reibaldi M, Russo A, Privitera G, Spatola C, Raffaele L, Salamone V, Farina R, Palmucci S, Musumeci A, Caltabiano R, Ragusa M, Mariotti C, Avitabile T, Milone P, Ettorre GC. Uveal melanoma: quantitative evaluation of diffusion-weighted MR imaging in the response assessment after proton-beam therapy, long-term follow-up. *Radiol Med*. 2017 Feb;122(2)131-139.
14. Singh M, Durairaj P, Yeung J. Uveal melanoma: a review of the literature. *Oncol Ther*. 2018 Jun;6(1):87-104.
15. iknl.nl.
16. Kamrava M, Sepahdari AR, Leu K, Wang P-C, Roberts K, Demanes DJ, McCannel T, Ellingson BM. Quantitative multiparametric MRI in uveal melanoma: increased tumor permeability may predict monosomy 3. *Neuroradiology*. 2015 Aug;57(8):833-840.
17. Dopierala J, Damato BE, Lake SL, Taktak AFG, Coupland SE. Genetic heterogeneity in uveal melanoma assessed by multiplex ligation-dependent probe amplification. *Invest Ophthalmol Vis Sci*. 2010 Oct;51(10):4898-4905.

18. Schoenfield L, Pettay J, Tubbs RR, Singh AD. Variation of monosomy 3 status within uveal melanoma. *Arch Pathol Lab Med.* 2009 Aug;133(8):1219-1222.
19. Herrick RC, Hayman LA, Taber KH, Diaz-Marchan PJ, Kuo MD. Artifacts and pitfalls in MR imaging of the orbit: a clinical review. *Radiographics.* 1997 May-Jun;17(3):707-724.
20. Beenakker J-WM, Shamonin DP, Webb AG, Luyten GPM, Stael BC. Automated retinal topographic maps measured with magnetic resonance imaging. *Invest Ophthalmol Vis Sci.* 2015 Jan 15;56(2):1033-1039.
21. Beenakker J-WM, van Rijn GA, Luyten GPM, Webb AG. High-resolution MRI of uveal melanoma using a microcoil phased array at 7T. *NMR Biomed.* 2013 Dec;26(12):1864-1869.
22. Benson WE. Posterior scleritis. *Surv Ophthalmol.* 1988 Mar-Apr;32(5):297-316.
23. Kafkala C, Daoud YJ, Paredes I, Foster CS. Masquerade scleritis. *Ocul Immunol Inflamm.* 2005 Dec;13(6):479-482.
24. Babu N, Kumar K, Upadhayay A, Kohli P. Nodular posterior scleritis – the great masquerader. *Taiwan J Ophthalmol.* 2021 Jul 19;11(4):408-412.
25. Khadka S, Byanju R, Pradhan S. Posterior scleritis simulating choroidal melanoma: a case report. *Beyoglu Eye J.* 2021 Jun 8;6(2):133-139.
26. Benson WE, Shields JA, Tasman W, Crandall AS. Posterior scleritis. A cause of diagnostic confusion. *Arch Ophthalmol.* 1979 Aug;97(8):1482-1486.
27. Biswas J, Mittal S, Ganesh SK, Shetty NS, Gopal L. Posterior scleritis: clinical profile and imaging characteristics. *Indian J Ophthalmol.* 1998 Dec;46(4):195-202.
28. Gordon LK. Orbital inflammatory disease: a diagnostic and therapeutic challenge. *Eye (Lond).* 2006 Oct;20(10):1196-1206.
29. Pakdaman MN, Sepahdari AR, Elkhamary SM. Orbital inflammatory disease: pictorial review and differential diagnosis. *World J Radiol.* 2014 Apr 28;6(4):106-115.
30. Rubinstein A, Riddell CE. Posterior scleritis mimicking orbital cellulitis. *Eye (Lond).* 2005 Nov;19(11):1232-1233.
31. Radhakrishnan R, Cornelius R, Cunnane MB, Golnik K, Morales H. MR imaging findings of endophthalmitis. *Neuroradiol J.* 2016 Apr;29(2):122-129.
32. Provenzale JM, Mukherji S, Allen NB, Castillo M, Weber AW. Orbital involvement by Wegener's granulomatosis: imaging findings. *AJR Am J Roentgenol.* 1996 Apr;166(4):929-934.
33. Silverman N, Shinder R. What's new in eyelid tumors. *Asia Pac J Ophthalmol (Phila).* 2017 Mar-Apr;6(2):143-152.
34. TNM classification of malignant tumours. Eighth edition 2017.
35. AJCC cancer staging manual. Eighth edition 2017.
36. Wójcicki P, Zachara M. Surgical treatment of eyelid tumors. *J Craniofac Surg.* 2010 Mar;21(2):520-525.
37. Yin VT, Merritt HA, Sniegowski M, Esmaeli B. Eyelid and ocular surface carcinoma: diagnosis and management. *Clin Dermatol.* 2015 Mar-Apr;33(2):159-169.
38. Sun MT, Wu A, Figueira E, Huilgol S, Selva D. Management of periorbital basal cell carcinoma with orbital invasion. *Futur Oncol.* 2015 Nov;11(22):3003-3010.
39. Donaldson MJ, Sullivan TJ, Whitehead KJ, Williamson RM. Squamous cell carcinoma of the eyelids. *Br J Ophthalmol.* 2002 Oct;86(10):1161-1165.

2

Uveal melanoma



2.1

MRI of uveal melanoma

Teresa A Ferreira, Lorna G Fonk, Myriam G Jaarsma-Coes, Guido GR van Haren,
Marina Marinkovic, Jan-Willem M Beenakker

Cancers 2019; 11(3):377

ABSTRACT

Uveal Melanoma (UM) is the most common primary malignant ocular tumor. The high soft tissue contrast and spatial resolution, and the possibility of generating 3D volumetric and functional images, make Magnetic Resonance Imaging (MRI) a valuable diagnostic imaging technique in UM. Current clinical MR protocols, however, are not optimized for UM and therefore lack the quality for accurate assessments. We therefore developed a dedicated protocol at a 3 Tesla MRI, using an eye-coil, consisting of multi-slice 2D sequences, different isotropic sequences and diffusion and perfusion weighted images. This protocol was evaluated in 9 uveal melanoma patients. The multi-slice 2D sequences had the highest in-plane resolution, being the most suited for lesion characterization and local extension evaluation. The isotropic 3D Turbo-Spin Echo (TSE) sequences were the most suitable for accurate geometric measurements of the tumor and are therefore important for therapy planning. Diffusion and perfusion weighted images aid in differentiating benign from malignant lesions and provide quantitative measures on tumor hemodynamics and cellularity, which have been reported to be effective on predicting and assessing treatment outcome. Overall, this dedicated MR protocol provides high quality imaging of UM, which can be used to improve its diagnosis, treatment planning and follow-up.

INTRODUCTION

Uveal melanoma (UM) is the most common primary intraocular malignancy in adults, although with an incidence of about 6 cases per million person-years [1,2]. UM arises in 85% of cases from the choroid, the remainder originating from the ciliary body or iris.

In the past enucleation was the main treatment, but in the last decade(s) various eye- and vision-saving treatments have become available, having the purpose to achieve local tumor control, conserving the eye and useful vision. This is of significant benefit to the quality of life for many patients. These eye preserving therapies include various forms of radiotherapy, such as episcleral brachytherapy, proton beam radiotherapy and stereotactic radiotherapy [3,4].

The ideal imaging technique for the evaluation of UM needs to be capable to accurately delineate the limits of the tumor, to do accurate measurements and to evaluate the presence of extrascleral extension, since these are the main determinants for the choice of the type of treatment, and in case of radiotherapy for the radiotherapy planning. Additionally, noninvasive markers that can predict treatment response and prognosis are needed [5,6], in order to adjust the frequency and type of screening according to whether the patient is at high or low risk of developing disseminated disease, and because even if a biopsy is performed, it can be not representative, due UM being heterogeneous in terms of chromosomal aberrations [7,8]. Finally, it should be able to early assess tumor response to radiotherapy.

UM has traditionally been evaluated with ultrasound, funduscopy and fluorescein angiogram (FA). Imaging the eye with MRI is a challenge due to eye motion and to the magnetic susceptibility effects at the air-bone interface. However, recent developments on MRI, make it a promising diagnostic imaging modality in ophthalmology, due to its excellent soft tissue contrast and spatial resolution, as well as its possibility to generate functional images such as diffusion weighted imaging (DWI) and perfusion weighted imaging (PWI)[5,6,9]. UM is therefore more and more being evaluated with MRI[5,6,9-11]. The purpose of our study was to optimize the MR imaging technique of the globe and in particular of uveal melanomas.

MATERIAL AND METHODS

This single-center prospective study was carried out according with the Code of Ethics of the World Medical Association (Declaration of Helsinki) for experiments involving humans and in accordance with recommendations of the local Ethic Committee. Informed Consent was obtained from all individual participants. A multiparametric ocular MRI protocol – Study Protocol - was prospectively evaluated at a 3T MRI (wide bore Ingenia 3T, Philips Healthcare, Best, The Netherlands) on nine consecutive patients with the diagnosis of UM. All patients were examined by an ocular oncologist, and the final diagnosis was made on the basis of fundoscopic, ultrasonographic and fluorescein angiographic imaging. Seven of the subjects

were male, they had a median age of 62 years old (range 31-81) and 89% of the lesions were located in the right eye. Table 1 shows the data regarding patients' sex, age, eye involved, American Joint Committee on Cancer (AJCC) tumor class [12], treatment and histology results in case of enucleation.

Table 1. Patients' data regarding sex, eye involved, treatment, histology in case of enucleation and classification according to the AJCC.

Patients	Gender	Eye	Treatment	Histology	Classification (AJCC)
1	Female	OD	PBT		T3b
2	Male	OD	Enucleation	Melanoma	T2b
3	Male	OD	Brachytherapy		T1a
4	Male	OD	Brachytherapy		T1a
5	Male	OS	Brachytherapy		T2a
6	Female	OD	Enucleation	Melanoma	T4b
7	Male	OD	Brachytherapy		T3a
8	Male	OD	Enucleation	Melanoma	T4a
9	Male	OD	Enucleation	Melanoma	T3a

OD – oculus dexter

OS – oculus sinister

PBT – proton beam therapy

AJCC - American Joint Committee on Cancer

General MRI setup

A 4.7 cm surface receive coil (Philips Healthcare, Best, The Netherlands), in combination with the body-coil for transmit, was used to image the eye, in order to maximize the signal-to-noise (SNR) of the MR-images [13]. A pair of goggles, made from a thermoplastic material (Orfit industries, Wijnegem, Belgium), was constructed and covered with Velcro® (Alfatex N.V., Deinze, Belgium), the latter permitting the attachment of the local receive coil to the goggles (Figure 1). Since the sensitivity of the coil decays as a function of the distance to the coil, image quality will depend strongly on the positioning of the coil and this system allows a good, easy and reproducible positioning of the eye coil [14]. Although a surface coil results in a higher SNR compared to the head coil, the absence of tight support of the head makes the scans much more vulnerable to motion. After preliminary experiments using different fixation methods, including cushions, sandbags and strapping the subject to the MRI table, a radiotherapy head support (MaxSupport™ wide shaped, red variant, 117000 HSSETW, Medeo, Schöftland, Switzerland), supported by sandbags proved to be the optimal balance between stability, patient comfort and ease of use. To mitigate eye-motion related artefacts in ocular MRI different methods have been proposed, such as cued blinking approaches [15,16]. These methods, however, rely on modifications to the MR-scanner and/or MR-sequences,

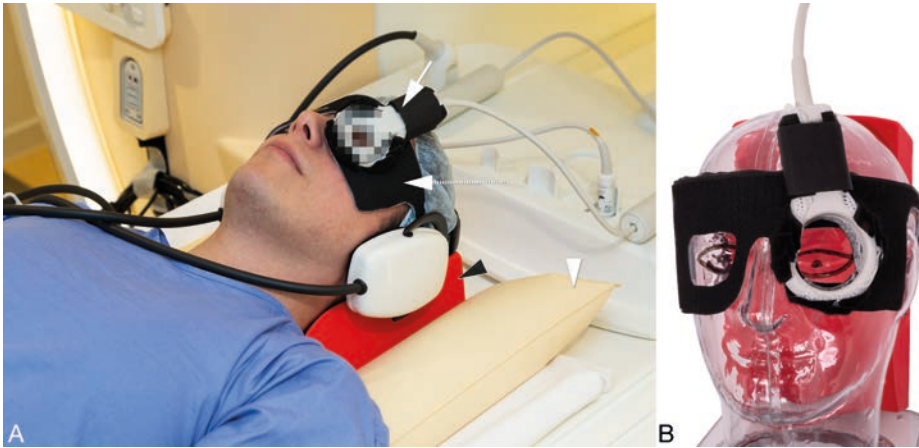


Figure 1. A-B. Clinical setup for ocular MRI.

A - The patients' head is supported by a radiotherapy head support (black arrowhead) which is stabilized by two sandbags (arrowhead). To aid an easy mounting of the eye coil (arrow) a pair of goggles (dashed arrow) is used on which the coil can be attached with Velcro.

B - Positioning of the eye coil and of the pair of goggles exemplified on a phantom to better show their relationship with respect to the eye.

which are difficult to use in clinical practice. We therefore decided to make no modifications to the conventional setup and only ask patients to close their eyes and to try to minimize their eye movement.

MRI sequences

The purpose of our study was to design a MRI protocol optimized for the evaluation of uveal melanomas. The requirements for imaging in UM include: 1) origin of the lesion. 2) dome, mushroom or lentiform shape. 3) local extension, in particular sclera, extrascleral or the ciliary body invasion. 4) solid or necrotic structure. 5) signal intensity on T1 and T2 weighted imaging sequences (WI). 6) contrast enhancement. 7) DWI characteristics. 8) PWI with evaluation of the Time-Intensity Curve (TIC). 9) dimensions – tumor prominence and largest basal tumor diameter (LBD). The tumor prominence is the tumor thickness and the sclera thickness was included in our series since in brachytherapy a radioactive source is sutured to the episcleral surface overlying the tumor. 10) presence of retinal detachment.

Multiple MR sequences for imaging the eye had been developed previously by imaging eyes of healthy volunteers to find the optimal balance between SNR, field-of-view (FOV), minimal artefacts and scan-time. These sequences had subsequently been evaluated on four UM patients to optimize the scans in terms of tumor contrast. A multiparametric ocular MRI protocol - Study Protocol, consisting both of anatomical and functional sequences, was then developed and subsequent prospectively evaluated in nine consecutive patients with the diagnosis of UM. This Study Protocol is described below and summarized in Table 2 and Figures 2 and 3.

Table 2. Scans' parameters of the anatomical and functional sequences from the Study Protocol and of the 3D TSE T1 SPIR, the latter not part of the Study Protocol, but lately added to the Clinical Protocol. Both the multi-slice (MS) 2 mm and the diffusion-weighted imaging sequences are planned perpendicular to the tumor, using the 3D scans as a reference. During the DCE scan, the contrast agent is administered and afterwards the contrast enhanced (Gd) scans are acquired.

Purpose	Scan name	voxel size (mm ³)	FOV (mm ³)	Oversampling (mm)	Echo train length	TE(ms)/TR(ms)/ Flip or ref. angle (deg)	Fat supr.	Avg. Scan time (mm:ss)	Additional parameters	
3D measurements	MS TSE 1 mm T1	0.9x0.9x1.0	80x80x40	70 mm	8	8.0/718/180	-	1	02:35	
	MS TSE 1 mm T1 SPIR	0.9x0.9x1.0	80x80x40	60 mm	6	8/636/180	SPIR	1	02:27	
	MS TSE 1 mm T2	0.9x0.9x1.0	80x80x40	20 mm	17	90/4436/120	-	2	02:04	
	3D TSE T1	1.0x1.0x1.0	80x80x40	40 mm	14	9.4/350/180	-	1	03:23	
	3D TSE T1 SPIR	1.0x1.1x1.0	80x80x40	45 mm	14	9.4/350/180	SPIR	1	03:23	
	3D TSE T2 SPIR	0.8x0.8x0.8	50x81x40	4 REST slabs	117	293/2500/35	SPIR	2	03:35	
	3D TFE T1	0.8x0.8x0.8	80x80x40	4 REST slabs	100	2.5/5/10	-	1	03:21	T _{inv} : 1000 ms
	MS TSE 1 mm T1 SPIR Gd	0.9x0.9x1.0	80x80x40	60 mm	6	8/636/180	SPIR	1	02:27	
	3D TSE T1 SPIR Gd	1.0x1.1x1.0	80x80x40	45 mm	14	9.4/350/180	SPIR	1	03:23	
	3D TFE T1 PROSET Gd	0.8x0.8x0.8	80x80x40	4 REST slabs	100	4.8/8.4/10	Proset 1331	1	03:22	
Tumor origin & extension	MS TSE 2 mm T1	0.5x0.5x2.0	100x100x24	-	6	8/718/180	-	1	01:16	
	MS TSE 2 mm T1 SPIR Gd	0.5x0.5x2.0	100x100x24	-	6	80/764/180	SPIR	1	01:16	
	MS TSE 2 mm T2	0.4x0.4x2.0	100x100x24	-	17	90/1331/120	-	2	01:25	
Functional scans	DWI (TSE)	1.25x1.4x2.4	100x100x24	24 mm	single shot	64/5759/50	SPIR	5	03:21	B=0,400,800 s/mm ²
	DCE	1.25x1.5x1.5	80x80x32			2.3/4.5/5	Proset 11	1	04:20	2 sec/dynamic

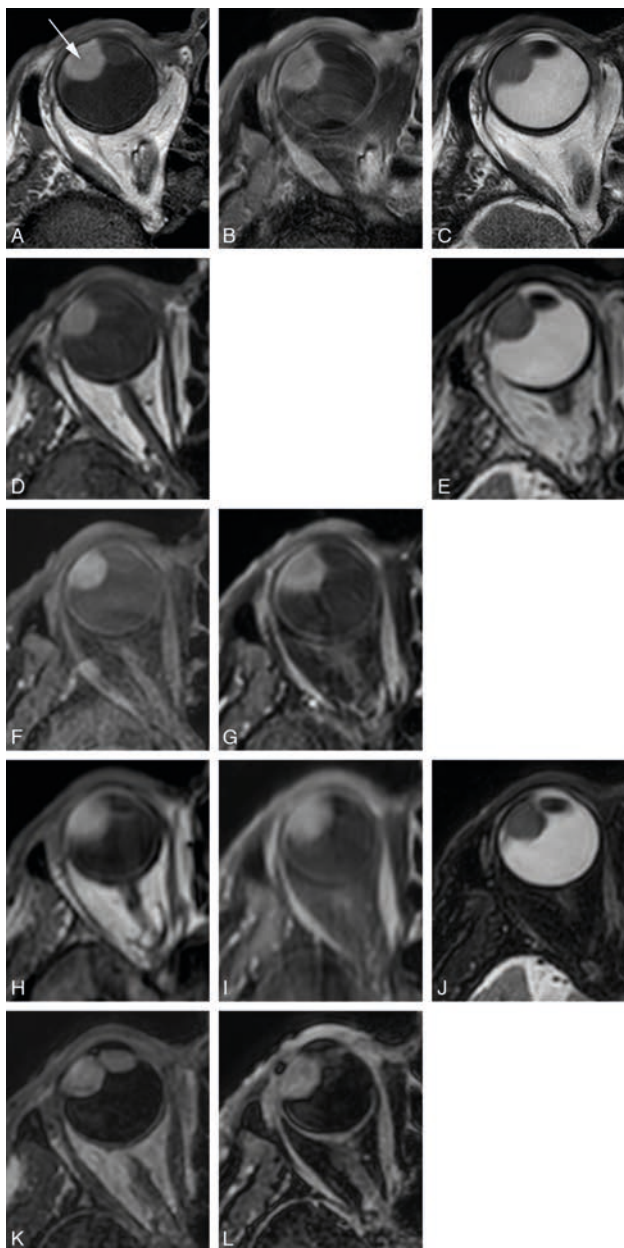


Figure 2.

A-L. Study protocol: Multiple anatomical axial MRI sequences in a patient with an uveal melanoma of the right eye (arrow).

A - MS 2 mm T1. B - MS 2 mm enhanced T1 with fat signal suppression. C - MS 2 mm T2.

D - MS 1 mm T1. E - MS 1 mm T2.

F - MS 1 mm T1 with fat signal suppression. G - MS 1 mm enhanced T1 with fat signal suppression.

H - 3D TSE 1 mm T1. I - 3D TSE 1 mm enhanced T1 with fat signal suppression. J - 3D TSE 0.8 mm T2 with fat signal suppression.

K - 3D TFE 0.8 mm T1. L - 3D TFE PROSET 0.8 mm enhanced T1 with fat signal suppression.

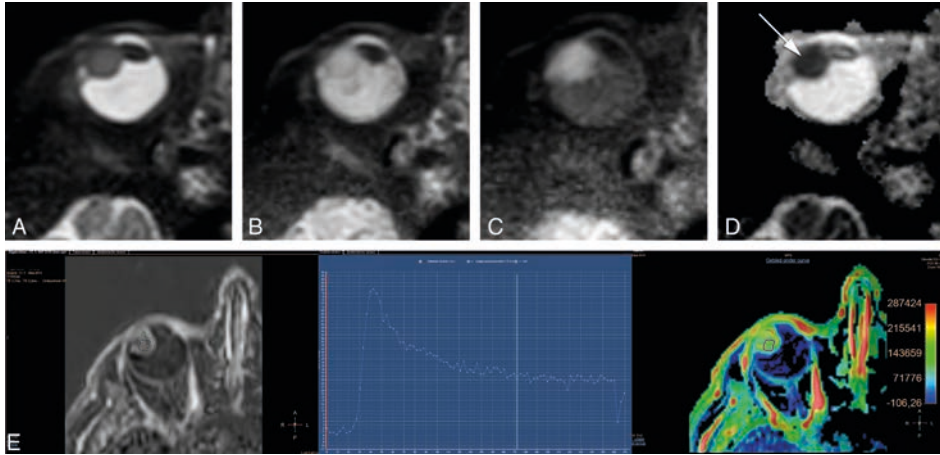


Figure 3.

A–E. Study protocol: Functional axial MRI sequences in the same patient as in Figure 2.

A–D - TSE DWI, with b values of 0 s/mm^2 (A), 400 s/mm^2 (B), 800 s/mm^2 (C) and Apparent Diffusion Coefficient (ADC) (D). Restricted diffusion in the uveal melanoma (arrow).

E - Dynamic Contrast-Enhanced (DCE) with a good quality, no movement artefacts, showing a wash-out TIC pattern.

Anatomical MR-sequences

The anatomical sequences of our Study Protocol are shown in Figure 2 and described in Table 2. We evaluated two different types of anatomical sequences. On one hand, MS multi-slice (MS) sequences with a slice thickness of 2 mm and a high in-plane resolution of approximately 0.5 mm were performed, which are mainly important for the evaluation of tumor origin and extension. These MS 2 mm sequences, due to their relatively thick slices, prevent multiplanar reconstructions being considered 2D sequences. On the other hand, isotropic sequences were performed, with an isotropic resolution of approximately 1 mm and therefore allowing multiplanar reconstructions, needed for accurate measurements. To assess the optimal sequence to acquire a 3D MR-image of the eye three different isotropic sequences were tested, namely MS sequences with 1 mm slices, 3D turbo spin-echo (TSE) sequences and 3D turbo field-echo (TFE) sequences. While on a 3D-sequence the complete volume is acquired simultaneously, on a MS-sequence multiple adjacent thin 2D slices are acquired. Furthermore, for the 3D sequences both gradient-echo and spin-echo techniques can be used. The gradient-echo sequences allow for a slightly higher resolution per imaging time than spin-echo sequences, but spin-echo sequences are less affected by the magnetic field inhomogeneities caused by the tissue-air interfaces around the globe. Both the MS 2 mm 2D and the isotropic sequences included T1-WI and T2-WI sequences, with or without fat suppression, and T1-WI sequences after contrast medium administration with fat suppression. Although, ideally all different combinations would have been evaluated, only a representative subset, listed in Table 2 and Figure 2, was acquired, to limit the total scan time to less than 45 minutes.

Preliminary evaluations in healthy subjects showed a different susceptibility to fold-over artefacts for the different scans, resulting on different field-of-views (FOV) for the different scans. To ease the planning, however, a single FOV, $80 \times 80 \times 40 \text{ mm}^3$, was set for most of the 3D scans and additional oversampling was added to prevent fold-over.

As the isotropic 3D sequences allow for retrospective reformatting in all directions they were acquired on the axial plane non-angulated. In contrast, the MS 2 mm 2D sequences were acquired perpendicular to the main axis of the tumor, to allow for an optimal discrimination between the tumor, retina-choroid and sclera.

Given that the posterior aspect of the globe is surrounded by orbital fat, attention had to be given to the water-fat-shift (WFS), since, depending on the direction of the WFS, the displaced fat might overlay the sclera/tumor or might lead to overestimating sclera thickness. Especially for the MS 2 mm 2D sequences, special care had to be given to the WFS during planning, since this scan has a relatively high WFS of 2.3 pixels whose direction depends on the, patient specific, angulation of the slice.

Functional MR-sequences

The functional sequences of our Study Protocol, shown in Figure 3 and described in Table 2, included DWI and PWI.

The tumor microstructure was assessed through DWI. Our preliminary evaluation on the first group of four UM patients showed that a diffusion weighting of $b=1000 \text{ s/mm}^2$, commonly used for neuro-imaging, resulted in a too strong attenuation of the signal from the tumor. We therefore evaluated two different levels of diffusion weighting, 400 s/mm^2 and 800 s/mm^2 . The DWI acquisition was acquired in the same orientation as the MS 2 mm 2D sequences, although at a lower resolution, using a non-Echo Planar Imaging (EPI) Turbo Spin Echo (TSE) readout, since the EPI readout is too sensitive to B_0 -inhomogeneities, prevalent in the orbit. To assess the tumor perfusion, a Dynamic Contrast-Enhanced (DCE) scan was included in the protocol, in which multiple images are acquired sequentially before, during and after intravenous administration of 0.1 mmol/kg gadoterate meglumine (gd-DOTA, DOTAREM, Guerbet, Roissy CdG Cedex, France). To achieve an increased temporal resolution key-hole imaging is often implemented [17], in which only the central part of k-space, which encodes for most of the contrast of the image, is acquired for all dynamics, and the peripheral k-space is only acquired in the first or last dynamic and subsequently used as a reference for all dynamics. Although the resulting increase in temporal resolution is certainly beneficial to assess inflow of the contrast agent, the sharing of k-space data makes the images very susceptible to eye-motion, since a drift in gaze direction between the reference acquisition and the other acquisitions, will result in significant motion artefacts in all images. We therefore employed the TWIST (Time-resolved angiography With Stochastic Trajectories) methodology [18], in which the acquisition of the peripheral k-space is split between adjacent

dynamics. As a result, the time difference between the central and peripheral k-space data is substantially reduced, resulting in a significant reduction of eye motion-related artefacts.

Evaluation

Images were evaluated by a Neuro and Head and Neck Radiologist with more than 20 years of experience and by an Ophthalmic MRI Specialist with 7 years of experience. Image quality, contrast and 3D geometrical accuracy were evaluated. The final decision was achieved by consensus.

RESULTS

Despite the challenges of susceptibility artefacts and eye motion when imaging the eye with MRI, multiparametric MRI of the eye is feasible, good quality images can be obtained and MRI can be used for the evaluation of UM. The clinical diagnosis of UM was confirmed by histology on all of the four enucleated cases. Table 3 shows the results of the evaluation of the several anatomical sequences of the Study Protocol. The in-plane image quality was evaluated for general image quality, contrast, identification of the sclera and of the tumor limits and differentiating the tumor from retinal detachment. Furthermore, the 3D sequences were evaluated regarding geometrical accuracy and identification of the sclera.

The MS 2 mm 2D sequences were the sequences with the highest in-plane resolution in our series (Figure 4). They are therefore most suited to evaluate details such as, normal eye anatomy, differentiating the layers of the globe wall and for a better delineation of the tumor boundaries. Regarding UM, this is needed for the evaluation of the layer of origin of the tumor, important for the differential diagnosis, and for the evaluation of UM extension, in particular scleral invasion, extrascleral extension or invasion of the ciliary body. Moreover, the MS 2 mm 2D sequences were the most suitable for evaluating the borders and shape of the tumor. Even quite flat UM with a prominence of 1-2 mm could be characterized (Figure 4 D-F). UM arising in small structures such as ciliary body and iris could be visualized well, as long as the sequences were planned perpendicular to the main axis of the tumor (Figure 4 G-I). Multiplanar reconstructions are needed for evaluating the tumor in different planes, to assess tumor geometry, for accurate measurements[9] and also play a role on the assessment of sclera/extrascleral extension. Multiplanar reconstructions are not feasible with the MS 2 mm 2D sequences as the relatively thick slices prevent perpendicular reconstructions. Multiplanar reconstructions were possible with all isotropic sequences, but in general we noticed a better quality of the multiplanar reconstructions from the 3D sequences when compared to the MS 1 mm sequences (Figure 5). The geometrical accuracy from the 3D sequences was very good, while the geometrical accuracy from the MS 1 mm sequences ranged sufficient to good (Table 3). Due to the relatively large acquisition time differences between subsequent

Table 3. Comparison of the anatomical sequences.

	Isotropic sequences									2D sequences perpendicular to the tumor – MS 2 mm		
	T2-weighted		T1-weighted before contrast				T1-weighted after contrast			MS	MS	MS T1 SPIR Gd
	MS TSE	3D TSE	MS TSE	MS TSE	3D TSE	3D TFE	MS TSE	3D SPIR	3D PROSET			
In-plane image quality												
General image quality	++	+	+	+	+/-	+/-	+	+/-	+	+	+	++
Contrast	+	++	+/-	+	+/-	+	++	+	++	++	+	++
Outer limit of sclera	++	+	+	+	+	-	+	+	-	++	++	+
Outer limits of tumor	+/-	+/-	+	+	+/-	-	++	+	-	+	+	+
Differentiate tumor vs RD							++	++	+			++
3D analysis												
Geometrical accuracy												
Good of complete eye	75%	78%	44%	44%	77%	100%	50%	88%	100%			
Small local artefacts	25%	22%	33%	55%	11%	0%	25%	13%	0%			
Not usable	0%	0%	22%	0%	11%	0%	25%	0%	0%			
Outer limit of sclera	++	+	+/-	+/-	+	-	+/-	+	-			

++ very good

+ good

+/- sufficient

- insufficient

RD – retinal detachment

slices in MS sequences, eye motion results in significant deformations, preventing accurate measurements (Figure 5B). 3D sequences are less sensitive to eye movement and therefore the reconstructions were of good quality, although small ghosting artefacts could be seen due to eye-motion (Figures 5D,F).

Comparison between 3D spin-echo (SE) and 3D gradient-echo (GE) sequences showed that the wall of the eye, in particular the outer limit of the sclera, is best identified on the SE sequences, while on the GE sequences, the outer limit of the sclera cannot be identified clearly. Contrast resolution on the other hand, was higher on the GE sequences, allowing better characterization of the tumor structure, in particular of tumor heterogeneity due to necrosis (Figure 6).

In our protocol the post-contrast T1-weighted scans were acquired with fat suppression, allowing for a better visualization of potential extra-scleral extension of the tumor. For pre-contrast T1 and T2 scans both fat-suppressed and unsuppressed scans were performed and have advantages. On one hand, in general pre-contrast T1 without fat suppression and T2 with fat suppression make infiltration of fat more conspicuous, but in case of UM that will also depend on its melanotic content and therefore on its signal intensity on T1 and T2. On

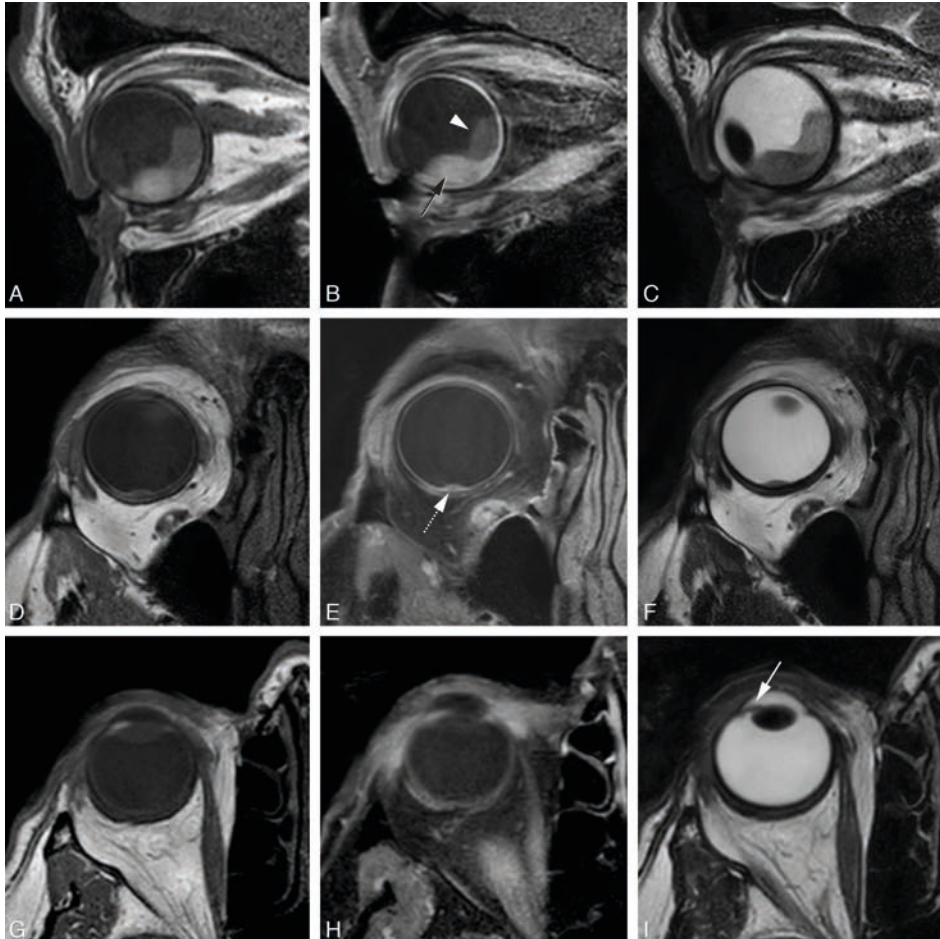


Figure 4.

A-I. MS 2 mm sequences in three different patients.

A-C - MS 2 mm sagittal T1 (A), enhanced sagittal T1 with fat signal suppression (B) and sagittal T2 (C), in a patient with a large choroidal melanoma of the right eye (black arrow), with retinal detachment (arrowhead) associated.

D-F - MS 2 mm axial oblique T1 (D), enhanced axial oblique T1 with fat signal suppression (E) and axial oblique T2 (F), in a patient with a small choroidal melanoma of the right eye (dashed arrow).

G-I - MS 2 mm axial T1 (G), enhanced axial T1 with fat signal suppression (H) and axial T2 (I), in a patient with a small iris melanoma of the right eye (arrow).

Notice that the MS 2 mm sequences have a high spatial resolution and therefore good for the evaluation of very small melanomas (D-F & G-I), even located at the iris.

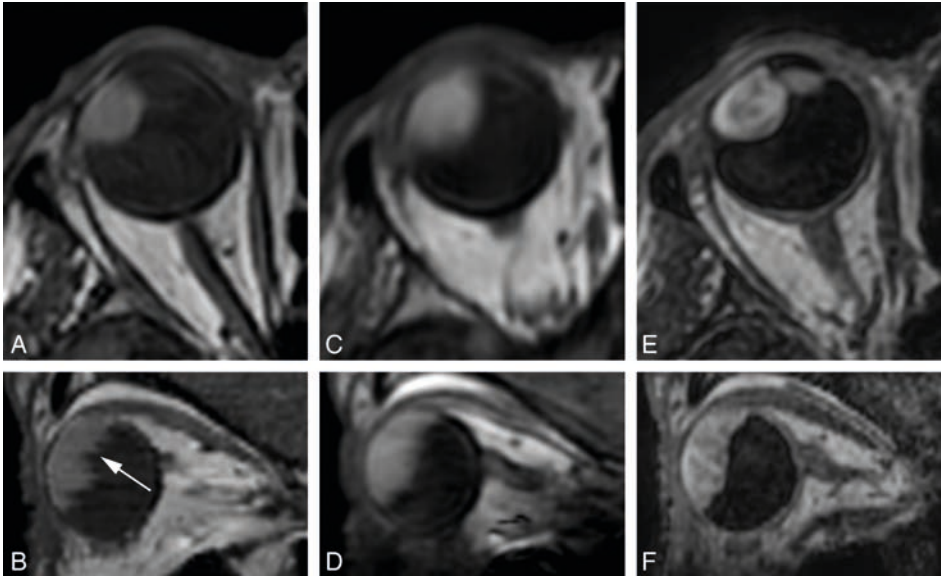


Figure 5.

A-F. MS 1 mm *versus* 3D sequences in a patient with an uveal melanoma of the right eye.

A-B - MS 1 mm axial T1 (A) and sagittal reconstruction (B).

C-D - 3D TSE 1 mm axial T1 (C) and sagittal reconstruction (D).

E-F - 3D TFE 0.8 mm axial T1 (E) and sagittal reconstruction (F).

Notice the stripes and wall deformation on the 3D reconstructions from the MS 1 mm sequence (B) (arrow), a frequent problem encountered when there is eye motion. This effect is not present in the 3D reconstructions from the 3D TSE or 3D TFE sequences, although some mild blurring is visible in the 3D TSE reconstruction.

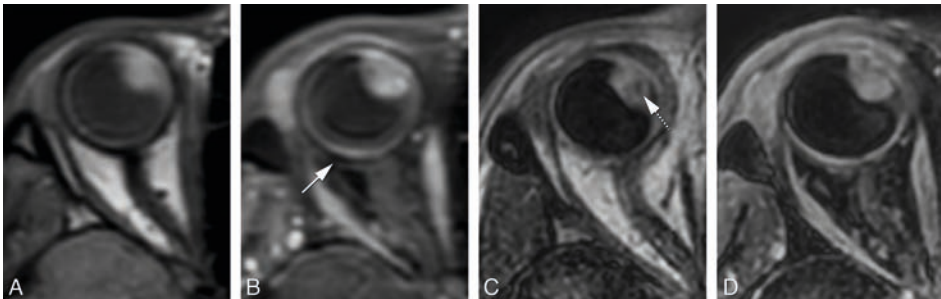


Figure 6.

A-D. 3D SE *versus* 3D GE sequences in two different patients.

A-D - 3D TSE 1 mm axial T1 (A), 3D TSE 1 mm enhanced axial T1 with fat signal suppression (B), 3D TFE 0.8 mm axial T1 (C) and 3D TFE 0.8 mm enhanced axial T1 with fat signal suppression (D), in a patient with a large uveal melanoma of the right eye. On one hand, on the SE sequences the outer limit of the sclera is better visualized (arrow), while on the GE sequences the outer limit of the sclera is more difficult to identify. On the other hand, the contrast resolution is better on the GE sequences, where a small area of necrosis is seen within the tumor (dashed arrow).

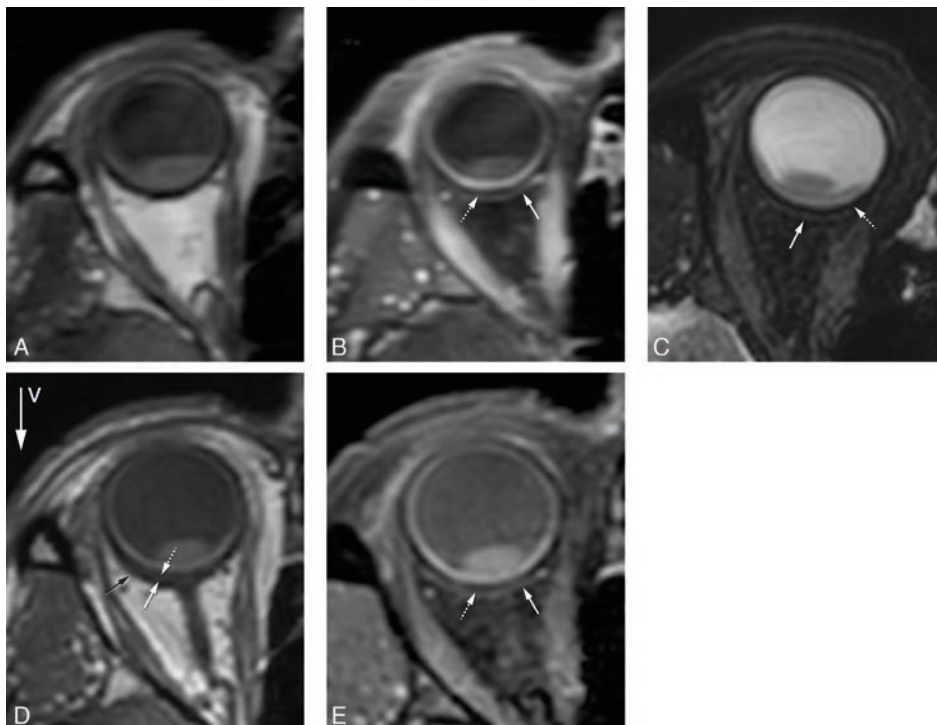


Figure 7.

A-E – Water fat shift artefact and “extra layer” outside sclera. 3D TSE 1 mm T1 (A), 3D TSE 1mm enhanced T1 with fat signal suppression (B), 3D TSE 0.8 mm T2 with fat signal suppression (C), MS 1 mm T1 (D) and MS 1 mm enhanced T1 with fat signal suppression (E) in the same patient. The water fat shift artefact is prominent on the MS sequence (D) (black arrow), seen as a signal void crescent area at the sclera-orbital fat interface, occurring in the frequency-encoding direction and therefore behind the sclera. It is important to be acquainted with this artefact not to misinterpret it as sclera which would overestimate the sclera thickness. The water fat shift artefact is negligible on the 3D TSE sequence (A) and it is not present on the sequences with fat suppression (B, C, E). Notice, especially on the sequences with fat signal suppression (B, C, E), but also visible on the MS 1 mm T1 (D), the presence of a thin layer slight hyperintense on T1 and T2 (arrows), perhaps corresponding to the Tenon’s space or to a slight layer of fluid outside the globe, allowing a good identification of the outer limit of the sclera (dashed arrows).

the other hand, a pre-contrast T1 with fat suppression allows for a better comparison with the post-contrast T1, also with fat suppression.

The chemical shift artefact at the sclera-fat interface, originating from the wrong spatial encoding of fat protons in the frequency encoding direction, is seen on the sequences without fat suppression, being removed with fat suppression (Figure 7). In our protocol, the water fat shift artefact was more prominent on the MS sequences, compared to the 3D TSE sequences. We noticed, especially on the sequences with fat signal suppression, but also on the MS 1 and 2 mm T1 and T2 sequences, the presence of a thin layer, located just adjacent to the globe, slight hyperintense on T1 and T2, allowing a good identification of the outer limit of the sclera (Figure 7), which was very helpful in measurements of tumor dimensions. This layer likely corresponds to the Tenon’s space or to a slight layer of fluid outside the globe, and can

also be seen on ultrasound A-scan as a small dip in reflectivity between the tumor and the extraocular structures.

Identifying enhancement of the lesion is crucial in order to differentiate UM from hematoma for instance. Because of its melanin content, UM are frequently spontaneously hyperintense on T1, making it difficult to be sure it is enhancing just from the visual evaluation of the post contrast series. For that the perfusion sequence is diagnostic and we did pre-contrast sequences also with fat suppression for an easier comparison.

Although it has been reported that the non EPI TSE DWI is limited by poor SNR relative to the acquisition time[6], we found mostly a good quality, with restriction diffusion easy to appreciate even in small uveal melanomas (Figure 8). We noticed moreover that the DWI sequence with a b value of 400 s/mm² was not as good as the one with a b value of 800 s/mm² and of no additional value.

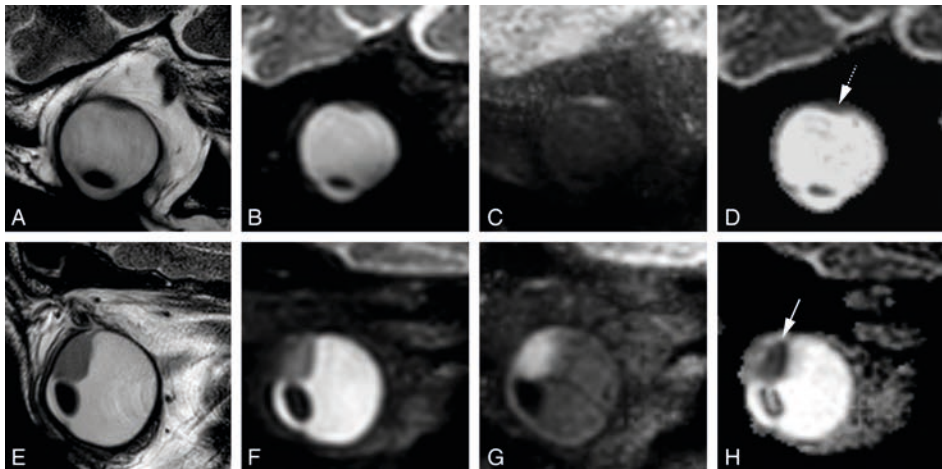


Figure 8.

A-H - TSE DWI in two different patients.

A-D - MS 2 mm sagittal oblique T2 (A), TSE DWI sagittal obliques with b values of 0 s/mm² (B), 800 s/mm² (C) and ADC (D). Restricted diffusion easy to appreciate in a small uveal melanoma (dashed arrow).

E-H - MS 2 mm sagittal oblique T2 (E), TSE DWI sagittal obliques with b values of 0 s/mm² (F), 800 s/mm² (G) and ADC (H). Clear restricted diffusion in the tumor (arrow).

The evaluation of the PWI showed mostly a good quality and a wash-out time-intensity curve (TIC) pattern. Eye motion and associated misregistration artefacts could compromise the evaluation of smaller tumors, but the comparison of the positioning of the region of interest (ROI) at the source images with the timepoint at the TIC curve made it possible to recognize these misregistration artefacts (Figure 9).

The presence of retinal detachment was easy to appreciate and to differentiate from the UM due to lack of enhancement, its typical configuration and attachment at the optic nerve, and the absence of restriction diffusion (unless hemorrhagic) (Figure 10).

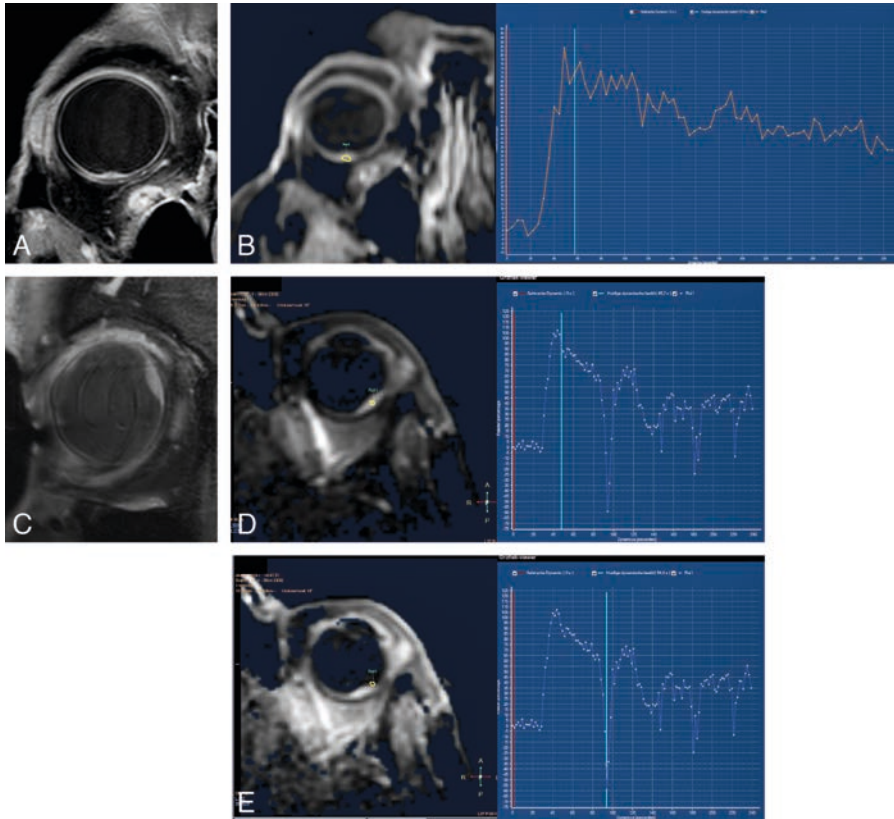


Figure 9.

A-E. DCE in two different patients.

A,B – Good DCE in a small tumor, with few movement artefacts and a wash-out TIC pattern.

C-E – DCE in a small uveal melanoma. Although with movement artefacts, these are possible to recognize by comparing the positioning of the ROI at the source images with the timepoint at the curve and noticing that the outliers in the curve match with ROI's that due to eye movement are located outside the tumor. Also with a wash-out TIC pattern. Notice the intra-ocular lens.

After evaluation of the extensive Study Protocol, a shorter Clinical Protocol was designed and evaluated in three UM patients. This clinical protocol consisted of MS 2 mm 2D sequences and a TSE DWI (b values of 0 and 800 s/mm²) and ADC, acquired perpendicular to the main axis of the tumor. It also included isotropic 3D TSE sequences and a DCE sequence, acquired on the axial plane non-angulated (Figure 11). The total scan time is 27 minutes. Notice that the MS pre-contrast T1 1 mm with fat signal saturation sequence was removed from the final protocol. Therefore to continue having the same pre-contrast, as the post-contrast T1 sequence, which is with fat signal saturation, a 3D TSE T1 with fat signal saturation was added to the Clinical Protocol (Table 2).

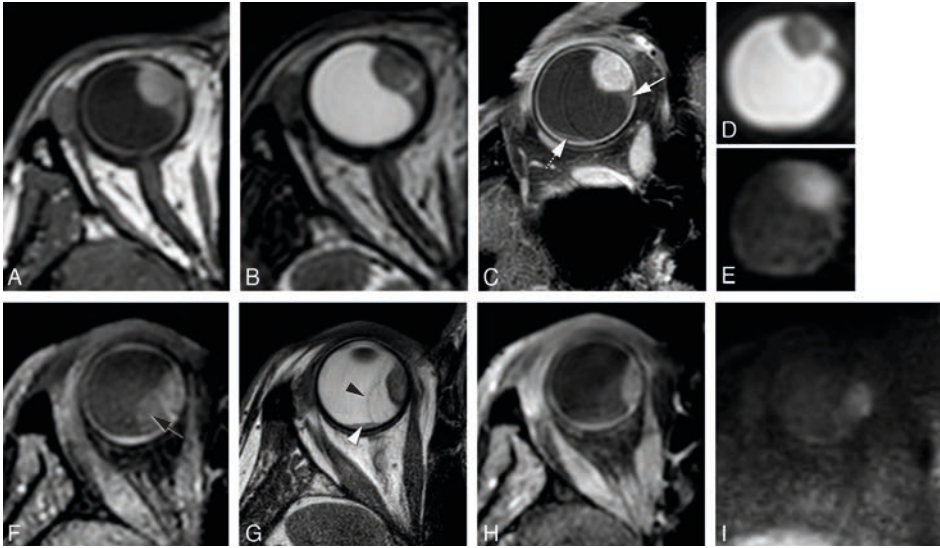


Figure 10.

A-I. Retinal detachment in two different patients.

A-E – MS 1 mm axial T1 (A), MS 1 mm axial T2 (B), MS 2 mm enhanced axial oblique T1 with fat signal suppression (C), DWI with b values of 0 s/mm² (D) and 800 s/mm² (E). Small homogeneous retinal detachment (arrow) located adjacent to the tumor, but also posterior and temporal (dashed arrow). It is distinguished from the tumor due to no enhancement, no diffusion restriction and a lentiform shape.

F-I – MS 1 mm axial T1 (F), MS 2 mm axial T2 (G), MS 1 mm enhanced axial T1 with fat signal suppression (H) and DWI with b value of 800 s/mm² (I). Large heterogeneous retinal detachment. One bigger component which is better seen on T1 without contrast (black arrow), while on T2 only the retina being seen (black arrowhead) and the content being similar to the vitreous. One smaller component better seen on T2 (arrowhead), and due to being hemorrhagic hyperintense on T1 and with slight diffusion restriction.

DISCUSSION

MR imaging of UM can be important for the diagnosis, choice of treatment, radiotherapy planning, potentially can predict treatment response and prognosis, and it should be able to early assess tumor response to radiotherapy. It is important to have a dedicated MRI protocol for the evaluation of uveal melanomas.

General technical requirements for ocular MRI

Ocular imaging requires high spatial resolution, high contrast and an adequate signal to noise ratio. Image quality will depend on the coil and MRI sequences used and on the presence of eye motion artefacts, the latter also related with scan time.

Although a head coil can be used, optimal evaluation of the globe and therefore of UM is achieved by use of a surface coil due to the higher resolution and SNR obtained. Surface coils are less suitable for evaluating the deeper aspect of the orbit and the remainder of the visual pathway. However, visualizing the deeper orbit is not required routinely in the context of

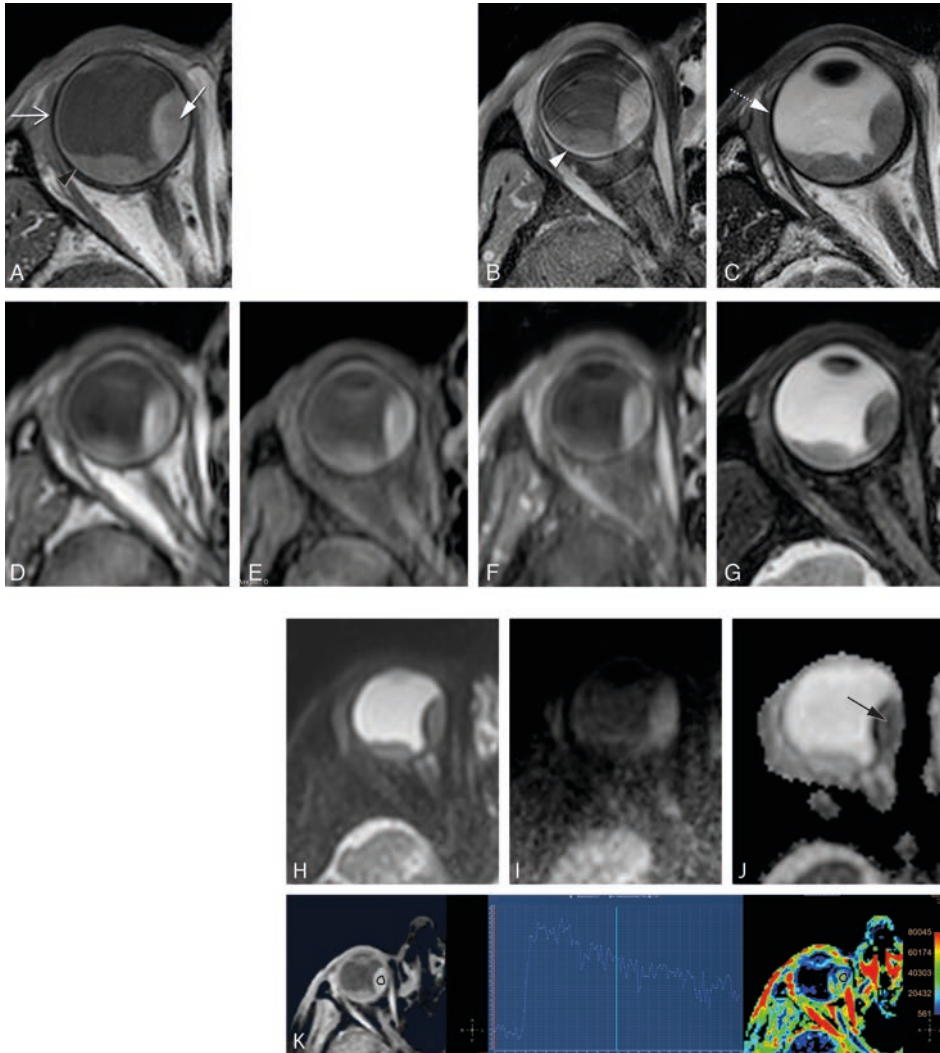


Figure 11.

A-K. Clinical protocol with anatomical and functional sequences in a patient with an uveal melanoma of the right eye (arrow).

A - MS 2 mm T1. B - MS 2 mm enhanced T1 with fat signal suppression. C - MS 2 mm T2.

D - 3D TSE 1 mm T1. E - 3D TSE 1 mm T1 with fat signal suppression. F - 3D TSE 1 mm enhanced T1 with fat signal suppression. G - 3D TSE 0.8 mm T2 with fat signal suppression.

H-J - TSE DWI, with b values of 0 (H), 800 (I) and ADC (J). Restricted diffusion in the uveal melanoma (black arrow).

L - DCE with a good quality, few motion artefacts, showing a wash-out TIC pattern.

Notice that on T2 WI the globe wall appears as a hypointense line (dashed arrow) and the different layers cannot be separated. On T1 the outer hypointense line corresponds to the sclera (open arrow), while the inner hyperintense layer corresponds to both the choroid and retina (black arrowhead). After contrast only the choroid and retina enhance (arrowhead). Anteriorly the ciliary body and iris can also be identified. The aqueous humor and vitreous body have a signal intensity similar to water. On the contrary, the lens is hypointense on T2 and slightly hyperintense on T1.

UM, since even extrascleral extension is usually limited to the tissues in close vicinity to the globe and can be evaluated with a surface coil. In the current setup a single coil is used to receive the MR-signal. The use of a multi-element receive coil would allow for a significant reduction on imaging time as the current images have sufficient SNR for acceleration through parallel imaging techniques such as GRAPPA (GeneRalized Autocalibrating Partially Parallel Acquisition) or SENSE (SENSitivity Encoding) [19,20]. However, at present such a multi-element coil is not available for clinical 3T MRI.

The eye has frequent voluntary and involuntary movements, both seriously degrading the MR images. Several methods have been described to minimize eye motion during the ocular MR examination, including performing the MRI under retrobulbar anesthesia [21,22]. In our study, patients were only instructed to keep their eyes closed during scanning and images devoid or with few artefacts could be obtained. The longer the sequence the bigger the chance of eye motion artefacts and so imaging time should be kept to the minimum needed to ensure quality. In our study, with the exception of the dynamic sequence, sequences lasted a maximum of 3 minutes and 35 seconds.

Another challenge of imaging the eye includes the location of the eye close to the air-tissue and bone-tissue interfaces and thus dealing with severe magnetic field inhomogeneity inducing distortion and signal dropouts. These magnetic susceptibility effects are amplified when using gradient echo as opposed to spin echo sequences. We also noticed that, in particular the GE sequences are not good for the differentiation of the various layers of the globe wall and to identify the outer limit of the sclera and therefore they were removed from the Clinical Protocol.

Anatomical MR imaging of uveal melanoma

The MRI protocol to evaluate an UM should include conventional sequences such as T1 and T2-WI sequences with and without a fat suppression and T1-WI sequences with a fat suppression technique after contrast medium administration. These are important for lesion characterization at diagnosis and in pre-treatment evaluation. To interpret these images the radiologist needs to be acquainted with the characteristics of UM on MRI. Moreover, he/she should be familiar with the normal aspect of the various eye structures on MRI (Figure 11). UM is usually hyperintense on T1, hypointense on T2 and it enhances. It is an uveal based lesion, either with a lentiform, a dome or a mushroom-shape. The chemical shift artefact at the sclera-fat interface, is due to the different resonance frequency of protons in fat and water and results in a spatial displacement of the fat signal in the frequency-encoding direction, while the water signal from the sclera remains correctly placed. It is as though the fat image was cut out, moved a few pixels, and pasted on the background image. On image it appears as a signal void crescent area just adjacent and merging with the sclera. The location of this artefact depends on the frequency-encoding direction, usually chosen to be outside and not inside the globe because that would interfere with the evaluation of the UM. The radiologist needs to

be acquainted with the chemical shift artefact at the sclera-orbital fat not to misinterpret it as sclera, which could result in an overestimation of the sclera thickness. The size of the water fat shift depends on multiple scan parameters, including frequency encoding gradient strength, resolution and magnetic field strength interface and it should be reduced to a minimum. In our sequences, we noticed that the water fat shift artefact is usually more prominent on the MS than on the 3D sequences.

Tumor measurements are crucial for choosing adequate treatment, in particular to decide between enucleation and an eye preserving therapy. Moreover, tumor measurements are important for the planning of the brachytherapy [3], as the plaque size used and the duration of treatment depend strongly on the size of the tumor. UM has been traditionally evaluated with ultrasound, but US tends to overestimate the tumor size [3,9]. The two important measurements that need to be taken are the tumor prominence and the largest basal tumor diameter. For accurate measurements the spatial resolution of the sequences should be high enough to clearly identify the limits of the tumor, but also the outer limit of sclera, as the sclera thickness is also included when assessing the tumor prominence. The tumor prominence and the LBD need to be measured perpendicular and parallel to the main axis of the tumor respectively. The measurement in one or two standardized planes can lead to considerable error in measuring the true tumor height, being the maximum error resulting from measurement in one plane as high as 1.41 times the true size [3]. To avoid this problem 3D sequences with subsequent reconstructions should be performed. Also three-dimensional data on the tumor geometry can be used for a more precise planning of the radiotherapy. In our study several isotropic sequences were evaluated, all permitting multiplanar reconstructions. 3D reconstructions from the MS 1mm sequences were frequently of suboptimal quality, showing stripes and wall deformation in case of motion. On the contrary, the 3D reconstructions of both the 3D TSE and 3D TFE sequences were mostly of good quality and less vulnerable to geometric distortions resulting from eye motion. Measurements should be preferably made on the 3D TSE enhanced T1 with fat signal suppression, since with this sequence good multiplanar reconstructions were possible, tumor is good differentiated from retinal detachment, the outer limit of the sclera is well identified and no water fat shift artifact is present. In case of no retinal detachment the 3D TSE T2 with fat signal suppression could also be used.

The evaluation of the extension of an UM, in particular whether extrascleral extension is present, is also crucial for treatment planning, since the presence of larger extrascleral extension generally implies enucleation. Extrascleral extension is present in 7% of the cases [10]. MRI is a valuable method for the assessment of scleral invasion and extrascleral extension, and is superior to US. In our study the sequences best suited for that purpose were the MS 2 mm 2D sequences, which are acquired perpendicular to the tumor, because they were where the tumor limits and the different layers of the globe were best identified.

Retinal detachment is seen in 65,5% patients[10] and is regarded as a sign of progression of disease. The tumor needs to be differentiated from retinal detachment. This is especially important in a bid not to overestimate the maximal basal diameter. Retinal detachment was better recognized after contrast because retinal detachment does not enhance and tumors do enhance. Others clues for this differentiation were that retinal detachment has a lentiform shape and a typical V shape with the vertex at the optic nerve [23].

Functional MR imaging of uveal melanoma

The MRI protocol to evaluate an UM should include functional images, such as diffusion weighted imaging (DWI) and perfusion weighted-imaging (PWI), which seem to be useful, although few studies have been published in UM [5,6,24,25].

DWI helps in distinguishing benign from malignant lesions, which is important in the differential diagnosis of UM [26]. It also helps in the differentiation between UM and retinal detachment, with UM showing diffusion restriction and with retinal detachment, except when hemorrhagic, with no diffusion restriction. Moreover, DWI seems effective on the pretreatment prediction of treatment outcome, with low ADC being correlated with good response and high ADC with poor response [5]. Finally, in UM treated with proton-beam therapy, ADC variations precede volume changes and early change in ADC value 1 month after therapy significantly correlated with tumor regression [5]. Although generally EPI techniques are used for DWI, the TSE technique is preferable for the orbit as it is less susceptible for the present magnetic field inhomogeneities [27]. Our images showed that this non-EPI technique results in good SNR, good contrast and almost no distortion. We achieved images where, even for tumors as small as 2 mm, restricted diffusion could be appreciated. We found no added value of the DWI images with a b value of 400 s/mm² and therefore it was removed from our Clinical protocol.

PWI provides data in the wash-in and wash-out contrast kinetics within a lesion. In DCE-MRI the qualitative evaluation of the time intensity curve (TIC) pattern seems to be a complementary investigation in distinguishing benign from malignant lesions. In the study from *Yuan et al* [24], a persistent TIC pattern (type I curve) suggests a benign lesion, a wash-out TIC pattern (type III curve) mostly suggests malignancy, and a plateau TIC pattern (type II curve) occurs both in benign and malignant lesions [24,27]. Additionally, PWI seems to give prognostic information, in the study from *Kamrava et al*, with a significant correlation between the k^{trans} and percent of monosomy 3 >33% [6]. Finally, PWI seems to be useful in the follow-up of UM treated with episcleral brachytherapy [28]. Most PWI in the orbit and globe used a dynamic contrast enhanced technique (DCE) in which serial T1-weighted images are acquired before, during and after contrast administration. In our study we also used a DCE technique. The challenge of studying the perfusion of a globe lesion is mainly related to eye motion with its associated misregistration artefacts, but in our study the DCE images were mostly diagnostic. The presence of eye motion is easy to check by looking at the source

images from the perfusion sequence. Eye motion could compromise the evaluation of small UM, where the ROI drawn in the tumor in order to obtain a time-intensity curve would, due to eye motion, fall outside the tumor and in the TIC appear as an outlier. The comparison of the positioning of the ROI at the source images with the timepoint at the TIC curve makes it possible to recognize these misregistration artefacts, obviating this problem.

Clinical MRI protocol for UM

The final Clinical Protocol developed includes MS 2 mm 2D sequences for lesion characterization and local extension evaluation. Isotropic 3D TSE sequences are also performed for accurate geometric measurements of the tumor, being therefore suitable for therapy planning. A TSE DWI sequence, with b values of 0 and 800 s/mm², can be used to confirm the malignancy of the lesion and is furthermore proposed to provide an earlier biomarker for therapy response. Finally, the contrast enhanced scans allow for proper differentiation between tumor and retinal detachment, while the DCE sequence is used to assess the tumor hemodynamics.

CONCLUSIONS

By combining a dedicated MRI protocol with a local receive eye-coil, high resolution MR-images of UM can be obtained. This multiparametric MR should ideally include 2D sequences for the diagnosis and determination of tumor extension, and 3D sequences for therapy planning. Furthermore, DWI and PWI sequences could be included to aid differential diagnosis, potentially giving prognostic information and important for the follow up after radiotherapy.

REFERENCES

1. Weis E, Salopek TG, McKinnon JG, Larocque MP, Temple-Oberle C, Cheng T, McWhae J, Sloboda R, Shea-Budgell M. Management of uveal melanoma: a consensus-based provincial clinical practice guideline. *Curr Oncol*. 2016 Feb;23(1):e57–64.
2. Dieckmann K, Georg D, Zehetmayer M, Bogner J, Georgopoulos M, Pötter R. LINAC based stereotactic radiotherapy of uveal melanoma: 4 years clinical experience. *Radiother Oncol*. 2003 May;67(2): 199–206.
3. Schueller P, Dogan A, Panke JE, Micke O, Willich N. Does the imaging method have an influence on the measured tumor height in ruthenium plaque therapy of uveal melanoma? *Strahlenther Onkol*. 2005 May;181(5):320–325.
4. Afshar AR, Damato BE. Uveal melanoma: evidence for efficacy of therapy. *Int Ophthalmol Clin*. 2015 Winter;55(1):23–43.
5. Foti PV, Longo A, Reibaldi M, Russo A, Privitera G, Spatola C, Raffaele L, Salamone V, Farina R, Palmucci S, Musumeci A, Caltabiano R, Ragusa M, Mariotti C, Avitabile T, Milone P, Ettorre GC. Uveal melanoma: quantitative evaluation of diffusion-weighted MR imaging in the response assessment after proton-beam therapy, long-term follow-up. *Radiol Med*. 2017 Feb;122(2):131–139.
6. Kamrava M, Sepahdari AR, Leu K, Wang P-C, Roberts K, Demanes DJ, McCannel T, Elligson BM. Quantitative multiparametric MRI in uveal melanoma: increased tumor permeability may predict monosomy 3. *Neuroradiology*. 2015 Aug;57(8):833–840.
7. Dopierala J, Damato BE, Lake SL, Taktak AF, Coupland SE. Genetic heterogeneity in uveal melanoma assessed by multiplex ligation-dependent probe amplification. *Invest Ophthalmol Vis Sci*. 2010 Oct; 51(10):4898–4905.
8. Schoenfield L, Pettay J, Tubbs RR, Singh AD. Variation of monosomy 3 status within uveal melanoma. *Arch Pathol Lab Med*. 2009 Aug;133(8):1219–1222.
9. Beenakker J-WM, Ferreira TA, Soemarwoto KP, Genders SW, Teeuwisse WM, Webb AG, Luyten GPM. Clinical evaluation of ultra-high-field MRI for three-dimensional visualisation of tumour size in uveal melanoma patients, with direct relevance to treatment planning. *MAGMA*. 2016 Jun;29(3): 571–577.
10. Lemke AJ, Hosten N, Wiegel T, Prinz RD, Richter M, Bechrakis NE, Foerster PI, Felix R. Intraocular metastases: differential diagnosis from uveal melanomas with high-resolution MRI using a surface coil. *Eur Radiol*. 2001;11(12):2593–2601.
11. Jaarsma-Coes MG, Ferreira TAG, van Haren GR, Marinkovic M, Beenakker J-WM. MRI enables accurate diagnosis and follow-up in uveal melanoma patients after vitrectomy. *Melanoma Res*. 2019 Dec;29(6):655–659.
12. Mellen PL, Morton SJ, Shields CL. American joint committee on cancer staging of uveal melanoma. *Oman J Ophthalmol*. 2013 May;6(2):116–118.
13. de Graaf P, Görlicke S, Rodjan F, Galluzzi P, Maeder P, Castelijns JA, Brisse HJ, European Retinoblastoma Imaging Collaboration (ERIC). Guidelines for imaging retinoblastoma: imaging principles and MRI standardization. *Pediatr Radiol*. 2012 Jan;42(1):2–14.
14. Vokurka EA, Watson NA, Watson Y, Thacker NA, Jackson A. Improved high resolution MR imaging for surface coils using automated intensity non-uniformity correction: feasibility study in the orbit. *J Magn Reson Imaging*. 2001 Nov;14(5):540–546.

15. Berkowitz BA, McDonald C, Ito Y, Tofts PS, Latif Z, Gross J. Measuring the human retinal oxygenation response to a hyperoxic challenge using MRI: Eliminating blinking artifacts and demonstrating proof of concept. *Magn Reson Med.* 2001 Aug;46(2):412–416.
16. Beenakker J-WM, van Rijn GA, Luyten GPM, Webb AG. High-resolution MRI of uveal melanoma using a microcoil phased array at 7T. *NMR Biomed.* 2013 Dec;26(12):1864-1869.
17. van Vaals JJ, Brummer ME, Dixon WT, Tuithof HH, Engels H, Nelson RC, Gerety BM, Chezmar JL, den Boer JA. “Keyhole” method for accelerating imaging of contrast agent uptake. *J Magn Reson Imaging.* 1993 Jul-Aug;3(4):671–675.
18. Tudorica LA, Oh KY, Roy N, Kettler MD, Chen Y, Hemmingson SL, Afzal A, Grinstead JW, Laub G, Li X, Huang W. A feasible high spatiotemporal resolution breast DCE-MRI protocol for clinical settings. *Magn Reson Imaging.* 2012 Nov;30(9):1257–1267.
19. Griswold MA, Jakob PM, Heidemann RM, Nittka M, Jellus V, Wang J, Kiefer B, Haase A. Generalized autocalibrating partially parallel acquisitions (GRAPPA). *Magn Reson Med.* 2002 Jun;47(6):1202–1210.
20. Pruessmann KP, Weiger M, Scheidegger MB, Boesiger P. SENSE: sensitivity encoding for fast MRI. *Magn Reson Med.* 1999 Nov;42(5):952–962.
21. Lemke, A.-J.; Alai-Omid, M.; Hengst, S. A.; Kazi, I.; Felix, R. Eye imaging with a 3.0-T MRI using a surface coil – a study on volunteers and initial patients with uveal melanoma. *Eur Radiol.* 2006 May; 16(5):1084–1089.
22. Malhotra A, Minja FJ, Crum A, Burrowes D. Ocular anatomy and cross-sectional imaging of the eye. *Semin Ultrasound CT MR.* 2011 Feb;32(1):2–13.
23. Lemke AJ, Hosten N, Bornfeld N, Bechrakis NE, Schüller A, Richter M, Stroszczyński C, Felix R. Uveal melanoma: correlation of histopathologic and radiologic findings by using thin-section MR imaging with a surface coil. *Radiology* 1999 Mar;210(3):775-783.
24. Yuan Y, Kuai XP, Chen XS, Tao XF. Assessment of dynamic contrast-enhanced magnetic resonance imaging in the differentiation of malignant from benign orbital masses. *Eur J Radiol.* 2013 Sep;82(9):1506–1511.
25. Jiang X, Asbach P, Willerding G, Dulce M, Xu K, Taupitz M, Hamm B, Erb-Eigner K. Dynamic contrast-enhanced MRI of ocular melanoma. *Melanoma Res.* 2015 Apr;25(2):149–156.
26. Sepahdari AR, Politi LS, Aakalu VK, Kim HJ, Razek AAKA. Diffusion-weighted imaging of orbital masses: multi-institutional data support a 2-ADC threshold model to categorize lesions as benign, malignant, or indeterminate. *Am J Neuroradiol.* 2014 Jan;35(1):170-175.
27. Ferreira TA, Saraiva P, Genders SW, van Buchem M, Luyten GPM, Beenakker J-W. CT and MR imaging of orbital inflammation. *Neuroradiology.* 2018 Dec;60(12):1253–1266.
28. Buerk BM, Pulido JS, Chiong I, Folberg R, Edward DP, Duffy MT, Thulborn KR. Vascular perfusion of choroidal melanoma by 3.0 tesla magnetic resonance imaging. *Trans Am Ophthalmol Soc.* 2004;102:209–15; discussion 215–7.

2.2

MR imaging characteristics of uveal melanoma with histopathological validation

Teresa A Ferreira, Myriam G Jaarsma-Coes, Marina Marinkovic, Berit Verbist, Robert M Verdijk, Martine J Jager, Gregorius PM Luyten, Jan-Willem M Beenakker

Neuroradiology 2022; 64(1):171-184

ABSTRACT

Purpose: To evaluate the Magnetic Resonance Imaging (MRI) characteristics of uveal melanoma (UM), to compare them with funduscopy and Ultrasound (US) and to validate them with histopathology.

Methods: MR-images from 42 UM were compared with US and funduscopy, and on 14 enucleated cases with histopathology.

Results: A significant relationship between the signal intensity on T1 and pigmentation on histopathology was found ($p=0.024$). T1-hyperintense UM were always moderately or strongly pigmented on histopathology, while T1-hypointense UM were either pigmented or non-pigmented. Mean Apparent Diffusion Coefficient (ADC) of the UM was $1.16 \pm 0.26 \times 10^{-3} \text{ mm}^2/\text{s}$. Two-thirds of the UM had a wash-out and the remaining a plateau perfusion time-intensity curve (TIC). MRI was limited in evaluating the basal diameter of flat tumors. US tends to show larger tumor prominence (0.5mm larger, $p=0.008$) and largest basal diameter (1.4mm larger, $p<0.001$). MRI was good in diagnosing ciliary body involvement, extrascleral extension and optic nerve invasion, but limited on identifying scleral invasion. An increase of tumor prominence was associated with lower ADC values ($p=0.030$) and favored a wash-out TIC ($p=0.028$). An increase of tumor ADC correlated with a plateau TIC ($p=0.011$).

Conclusions: The anatomical and functional MRI characteristics of UM were comprehensively assessed. Knowing the MRI characteristics of UM is important in order to confirm the diagnosis, to differentiate UM from other intra-ocular lesions and because it has implications for treatment planning. MRI is a good technique to evaluate UM, being only limited in case of flat tumors or on identifying scleral invasion.

INTRODUCTION

Uveal melanoma (UM) is the most common primary intraocular malignancy in adults [1–4]. UM is very different from cutaneous melanoma in terms of survival, genetic profile and in the lack of effective therapies to prevent metastatic disease [5–7]. In the past, enucleation was the main treatment, but over the last decades, various eye- and vision-saving treatments have become available, including episcleral brachytherapy, proton beam radiotherapy, and stereotactic radiotherapy [2, 3, 8].

Ultrasound (US), funduscopy, and fluorescein angiography are the most frequently used techniques to evaluate UM at the diagnosis, for pre-treatment planning, and for follow-up after radiotherapy [3, 4]. However, the diagnosis with these conventional ophthalmic imaging modalities is difficult in smaller uveal melanomas/melanocytic lesions, in atypical tumors, in lesions behind the iris and in case of opacification of the ocular media. Furthermore, US has limitations in pre-treatment planning of UM and during follow-up, being only able to evaluate dimensional changes of the lesion. Another option for imaging the globe is Magnetic Resonance Imaging (MRI), which has sometimes been challenging because of eye motion and/or susceptibility artifacts [8–10]. However, recent developments on MRI allow good quality images [8]. Moreover, with a high soft tissue contrast and spatial resolution, the possibility of generating 3D volumetric and functional images and the possibility of evaluating UM in eyes of vitrectomized patients with a SiOil tamponade, MRI seems to be of added value in comparison with US [8, 11–13].

In this study, we evaluate the use of MRI in a series of primary UM. Firstly, we will provide a complete description of the radiological characteristics of UM, which can aid in using MRI to differentiate UM from other intra-ocular lesions, as for UM biopsies are generally not performed to confirm the diagnosis. This evaluation will not only include anatomical parameters, such as signal intensities on T1- and T2-weighted images (WI), but also include functional parameters, such as the Apparent Diffusion Coefficient (ADC) and quantifiable perfusion characteristics. Secondly, we will compare clinical parameters related to treatment and/or prognostication, such as tumor dimensions, pigmentation and involvement of nearby structures, between MRI and conventional ophthalmic techniques, including funduscopy and US. These findings will be validated with histopathology when available. Finally, attention will be given to potential MRI prognostic markers, which would help to identify high-risk UM.

METHODS

Forty-two patients with the diagnosis of primary UM were evaluated. The first cohort consisted of thirty consecutive patients, who were prospectively evaluated at the Leiden University Medical Center (LUMC), as part of a single-institution prospective study, carried

out according to the Declaration of Helsinki. Following approval of the protocol by the local Medical Ethical Committee (METC P16.186), Informed Consent was obtained from all participants. The second group consisted of twelve patients, whose eyes were scanned for a clinical reason and that were retrospectively evaluated, with permission from the local Medical Ethical Committee. This group included one case treated with ruthenium brachytherapy, four cases that received proton beam therapy and seven cases that underwent enucleation.

All 42 patients were examined by an ocular oncologist, and the final diagnosis was made on the basis of fundoscopic, fluorescein angiographic, and ultrasonographic findings, prior to the MRI examination.

The mean age of all subjects was 62 years (range 24-90) and sixty-nine percent were male. In 61% of the patients, the lesion was localized in the right eye. The clinical American Joint Committee of Cancer T-Stage of the UM was T1 in 29%, T2 in 31%, T3 in 31% and T4 in 9%. Regarding treatment, 45% of the cases received ruthenium brachytherapy, 21% proton beam therapy and 33% were enucleated. In one patient, the diagnosis was not clear, and, prior to the MRI, a biopsy was performed, disclosing a UM. In all 14 patients who underwent enucleation histopathology confirmed the clinical diagnosis of UM.

All patients underwent a 3T MRI (wide bore Ingenia 3T, Philips Healthcare, Best, The Netherlands), using the ocular protocol that we previously developed [8], with minor adjustments: a higher resolution of the 3D TSE T1 sequences, Diffusion Weighted Imaging (DWI) with B values only of 0 and 800 s/mm² and a higher flip angle of the dynamic scan (Table 1; Figure 1).

Table 1. MRI scans' parameters including both anatomical and functional sequences. The MS and DWI sequences are acquired perpendicular to the main axis of the tumor. The 3D TSE and DCE sequences are acquired on the axial plane non-angulated. During the DCE scan, intravenous administration of 0.1 mmol/kg gadoterate meglumine (gd-DOTA, DOTAREM, Guerbet, Roissy CdG Cedex, France) is administered and afterwards the contrast enhanced (Gd) scans are acquired.

Purpose	Scan name	Voxel size (mm ³)	Echo train length	TE(ms)/ TR(ms)/ Flip or ref. angle (deg)	Fat supr.	Scan time (mm:ss)	Additional parameters
3D measurements	3D TSE T1	0.8x0.8x0.8	20	26/400/90	-	02:07	
	3D TSE T1 SPIR	0.8x0.8x0.8	20	26/400/90	SPIR	02:07	
	3D TSE T2 SPIR	0.8x0.8x0.8	117	305/2500/35	SPIR	02:58	
	3D TSE T1 SPIR Gd	0.8x0.8x0.8	20	26/400/90	SPIR	02:07	
Tumor origin & extension	MS TSE T1	0.5x0.5x2.0	6	8/718/180	-	01:16	
	MS TSE T2	0.4x0.4x2.0	17	90/1331/120	-	01:25	
	MS TSE T1 SPIR Gd	0.5x0.5x2.0	6	80/764/180	SPIR	01:16	
Functional scans	DWI (TSE)	1.25x1.4x2.4	single shot	50/1555/50	SPIR	01:33	B=0,800 s/mm ²
	DCE	1.25x1.5x1.5		2.3/4.5/13	Proset 11	04:20	2 sec/dynamic

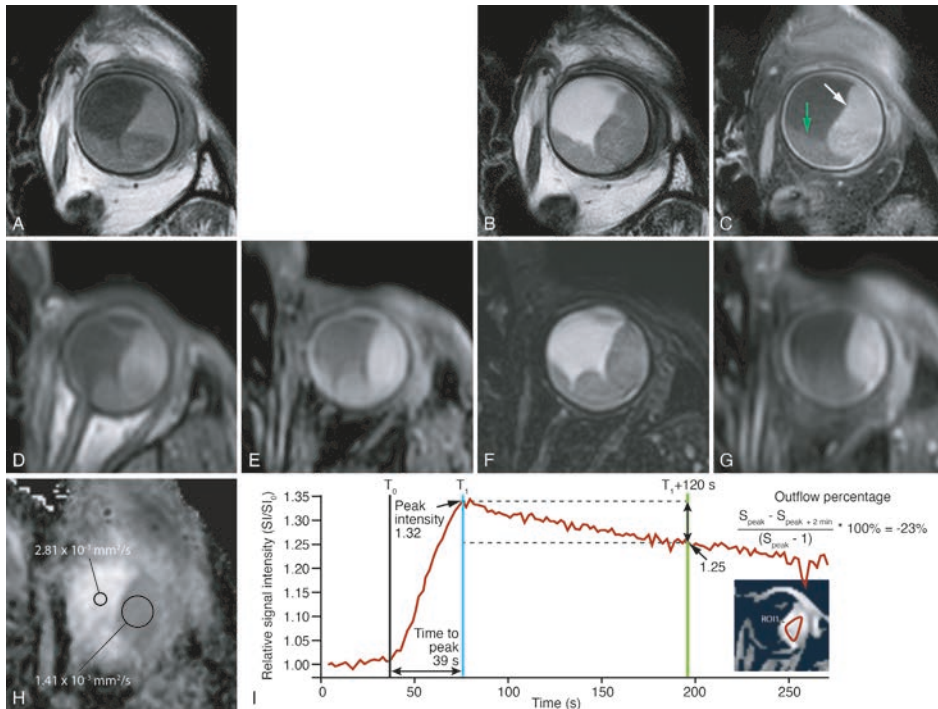


Figure 1. MRI ocular protocol. Uveal melanoma of the left eye (white arrow) with associated retinal detachment (green arrow). ADC of $1.4 \times 10^{-3} \text{ mm}^2/\text{s}$. Wash-out time intensity curve at DCE.

A - MS T1. B - MS T2. C - MS contrast-enhanced T1 with fat signal suppression.

D - 3D TSE T1. E - 3D TSE T1 with fat signal suppression. F - 3D TSE T2 with fat signal suppression. G - 3D TSE contrast-enhanced T1 with fat signal suppression.

H - ADC. I - Quantitative evaluation of the DCE. Black line - Arrival time (T_0) = time-point at which the lesion starts to enhance, determined manually. Blue line - corresponds approximately to the Peak time (T_1) = first time-point when the lesion reached 95% of its maximum intensity, determined automatically and corresponding to the time-point at which Peak intensity (PI) is calculated. Time to peak (TTP)(s) = $T_1 - T_0$. Green line - Outflow percentage at 2 min (OP2,%) = percentage of signal intensity loss at 2 min compared to the intensity at the Peak time. Notice the wash-out time intensity curve. SI - signal intensity at every timepoint. SI_0 - signal intensity at timepoint zero.

Tumor origin (choroid, ciliary body or iris) was assessed on MRI. The presence of a mushroom configuration was evaluated on MRI, when histopathology was available it was correlated with rupture of Bruch's membrane. The signal intensity of UM on MRI was assessed and it was evaluated whether it reflects UM pigmentation, by comparing it both to funduscopy and histopathology. Tumor signal intensity on T1- and T2-WI was classified as hyper-, iso-, or hypointense. When UM were compared to the vitreous on MRI, all were hyperintense on T1- and hypointense on T2-WI, showing the vitreous to be an unsuitable reference for their signal intensity. Better differentiation of signal intensities was obtained when using the signal intensity of the choroid as reference on T1- and of the eye muscles on T2-WI. Tumor pigmentation on funduscopy was categorized as pigmented or non-pigmented. Tumor pigmentation on histopathology was classified according to their macroscopic color as seen in several cuts through the UM: white - no pigmentation; yellow/grey - slight pigmentation;

brown - moderate pigmentation; black - strong pigmentation. We compared UM signal intensity on T1- and T2-WI and clinical pigmentation as seen on fundoscopy in the group of homogeneous or minimally heterogeneous UM (n=36). The six bipartite UM were excluded in this evaluation. We furthermore compared UM signal intensity on T1- and T2-WI with pigmentation on histopathology in the group of the 14 enucleated eyes. On the four enucleated eyes with bipartite UM, both components were separately checked, accounting for a total of 18 evaluable lesions. For the ADC measurements, one representative region of interest (ROI) was drawn by the same neuroradiologist, excluding the tumor edge and potential necrotic parts, and one reference ROI was drawn in the vitreous. The tumor perfusion characteristics: Arrival time (T0)(s), Time to peak (TTP)(s), Peak intensity (PI), Outflow percentage at 2 min (OP2,%) and the type of time-intensity curve (TIC) were evaluated in 3D, all results corresponding therefore to the average from the whole UM. Additionally, the type of TIC was also evaluated in 2D: in homogeneous tumors from a representative 2D image, and in bipartite tumors from both tumor components. The type of TIC was classified according to Yuan et al as persistent, plateau or wash-out pattern [14]. However, to limit the effect of potential eye-movement, the outflow was evaluated at 2 min, instead of the 5 min, being the plateau and wash-out patterns defined as a final intensity at 2 min of 95-100% and below 95% of the Peak intensity respectively (Figure 1) [14]. Tumor dimensions and tumor extension were evaluated on MRI and US and validated with histopathology when available. The presence of retinal detachment (RD) was evaluated with MRI and US. Finally, on the enucleated eyes the presence of extracellular matrix patterns (defined as three adjacent full loops) and of monosomy 3 in the tumor was checked.

RESULTS

Origin and Shape – In 57% of the cases, the UM originated in the choroid, in 38% in either the choroid or ciliary body and in 5% (n=2) in the iris. In five patients (12 %) a mushroom configuration was seen on MRI. All these five patients have undergone an enucleation and Bruch’s membrane rupture was confirmed in all. Histopathology did reveal rupture of Bruch’s membrane in three additional melanomas which had not been classified as mushroom configuration on MRI. However, retrospectively and mainly with the help of multiplanar reconstructions, a mushroom configuration was found on MRI as well. As expected, a mushroom configuration was more prevalent in larger tumors (Figure 2).

Signal intensity - Tables 2 and 3 show the comparison between signal intensity on T1- and T2-WI and fundoscopy and histopathology respectively. A significant relationship between the signal intensity on T1-WI and pigmentation on histopathology was found (Kruskal-Wallis test; chi-square=7.45; p=0.024). No significant relationship between the signal intensity on

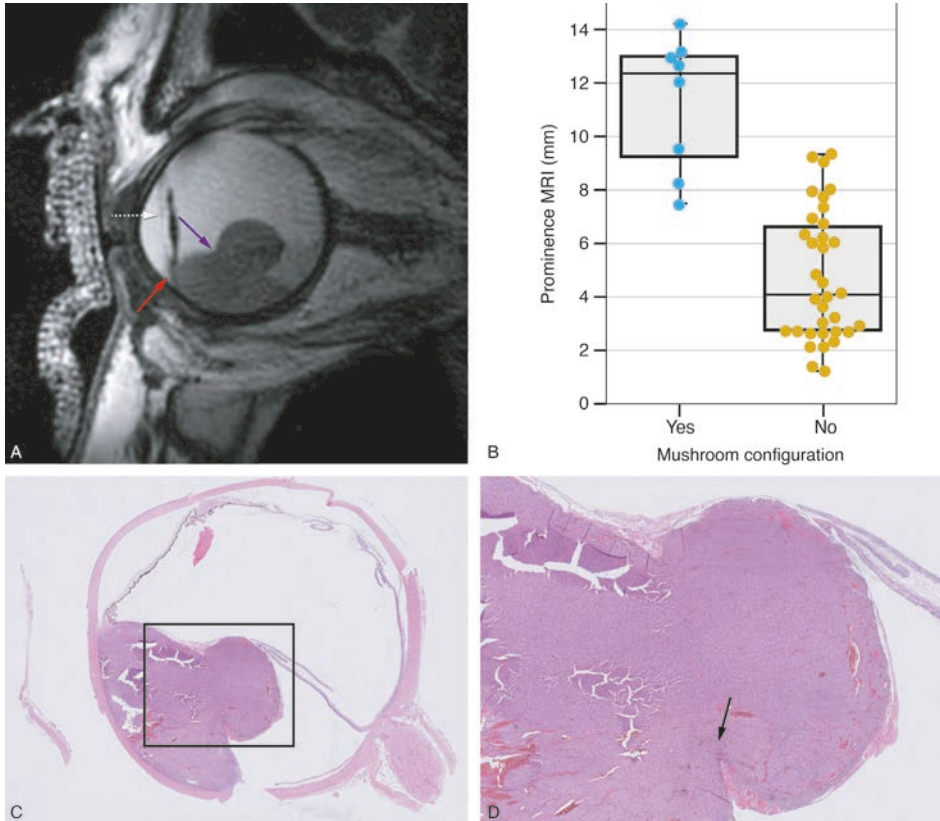


Figure 2. MR image of a mushroom configuration, its corresponding histopathological image and the comparison of tumor prominence between uveal melanomas with and without a mushroom shape.

A - MRI with sagittal MS TSE T2-WI showing a UM with a mushroom configuration (purple arrow). There is invasion of the ciliary body and iris (red arrow). Notice that the iris can be clearly identified (white dashed arrow) and that the patient has an intraocular lens.

B - Boxplot to illustrate the relation between the presence of a mushroom configuration and tumor prominence (n=42). It is evident that a mushroom configuration is more present in tumors with larger prominences, with five patients having a tumor prominence of 12 mm or more.

C-D - Histopathologic examination hematoxylin and eosin stain (H&E). Notice the rupture of the Bruch membrane in the region of the neck of the mushroom (black arrow).

T2-WI and pigmentation on histopathology was found (Kruskal-Wallis test; chi-square=2.03; p=0.36), neither between the signal intensity on T1-WI and pigmentation on funduscopy (chi-square test; chi-square=2.22; p=0.33) nor between the signal intensity on T2-WI and pigmentation on funduscopy (chi-square test; chi-square=0.583; p=0.75) (Figure 3).

DWI - Seven UM were excluded from ADC evaluation, due to unreliable measurement in tumors with a prominence less than 2.5 mm, or due to technical problems. The distribution of UM ADCs (mean: $1.16 \pm 0.26 \times 10^{-3} \text{ mm}^2/\text{s}$) is shown in Figure 4A. Mean ADC of the vitreous was $3.03 \pm 0.17 \times 10^{-3} \text{ mm}^2/\text{s}$.

Table 2. Contingency Table comparing the signal intensity of the homogeneous UM on T1- and T2-WI with the pigmentation at fundoscopy.

		Pigmentation Fundoscopy		
		Yes	No	Total
Signal Intensity T1-WI	Hyperintense	13	1	14 (39%)
	Isointense	11	4	15 (42%)
	Hypointense	5	2	7 (19%)
Signal Intensity T2-WI	Hyperintense	22	6	28 (78%)
	Isointense	5	1	6 (17%)
	Hypointense	2	0	2 (5%)
Total		29 (81%)	7 (19%)	36 (100%)

Table 3. Contingency Table comparing the signal intensity of the UM on T1- and T2-WI with the pigmentation at histopathology.

		Pigmentation Histopathology				Total
		Strong	Moderate	Slight	No	
Signal Intensity T1-WI	Hyperintense	4	3	0	0	7 (39%)
	Isointense		2	2	1	5 (28%)
	Hypointense	1	1	1	3	6 (33%)
Signal Intensity T2-WI	Hyperintense	2	4	3	3	12 (67%)
	Isointense	2	0	0	1	3 (17%)
	Hypointense	1	2	0	0	3 (17%)
Total		5 (28%)	6 (33%)	3 (17%)	4 (22%)	18 (100%)

Perfusion Weighted Imaging (PWI) – Five UM were excluded from the 3D evaluation and three UM were also excluded from the 2D evaluation, due to eye motion in tumors with a prominence of 3.5 mm or less, or due to technical problems. The perfusion quantitative results are shown in Figure 4 C-E.

The 3D evaluation showed in 65% of the cases a wash-out TIC and in 35% a plateau TIC. The 2D evaluation showed in 64% a wash-out TIC, at 28% a plateau TIC and at 8% both a wash-out and a plateau TIC. In seven patients (19%), the qualitative evaluation of the time-intensity curves differed between the 3D and 2D evaluations.

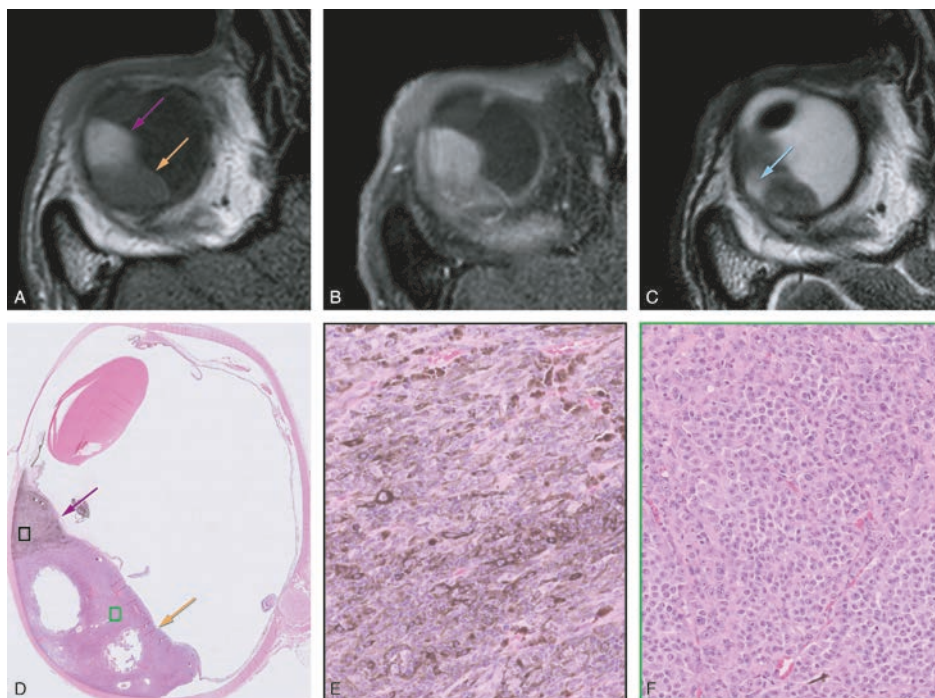


Figure 3. Bipartite uveal melanoma with a good correspondence between signal intensity on T1 and pigmentation on histopathology.

A-C – MRI with axial MS TSE T1-WI (A), contrast-enhanced T1-WI with fat signal suppression (B) and T2-WI (C). D-F - Histopathologic examination H&E.

Bipartite UM of the right eye, with one component which is hyperintense on T1 and on histopathological examination strongly pigmented (pink arrows and E), and a second component which is hypointense on T1 and on histopathological examination non-pigmented (orange arrows and F). Notice that on T2 these two different components are not differentiated, but a small hyperintense area (blue arrow) is seen corresponding to a cystic necrotic area depicted on the histopathological examination. Notice also the presence of both epithelioid and spindle cells on the pigmented component (E), while the non-pigmented part only harbours epithelioid cells (F).

Dimensions – A paired t-test of the mean difference showed that both the tumor prominence (TP) (measured including the scleral thickness) and tumor largest basal diameter (LBD) were significantly higher on US than on MRI (mean TP 6.43 mm and 5.94 mm; SD 3.46 and 3.37; $p=0.008$) (mean LBD 13.70 mm and 12.31 mm; SD 4.38 and 4.03; $p<0.001$). When compared to histopathology, both dimensions were smaller on histopathology than on MRI in 11 out of 14 cases, which is to be expected due to shrinkage. There was one case however where the LBD was 5 mm larger on histopathology than on MRI. This likely was due to a peripheral flat component of the tumor (Figure 5).

Ciliary body involvement - Histopathology and MRI were consistent regarding ciliary body involvement: 57% of the enucleated eyes showed ciliary body involvement on MRI as well as in histopathology (Figure 2).

Scleral invasion – Although not seen on MRI in any of the 42 patients, scleral invasion was present in the histopathologic sections in 10 of the 14 enucleated eyes (71%). Retrospectively, minimal signs of scleral invasion could be observed on MRI in two patients (Figure 6), with an irregular inner contour and slight enhancement of the sclera.

Extrascleral extension - MRI depicted extrascleral extension in three patients (7%), which was confirmed during surgical placement of tantalum markers (one patient) or on histopathology after enucleation (two eyes). In two of these three patients the extrascleral extension was

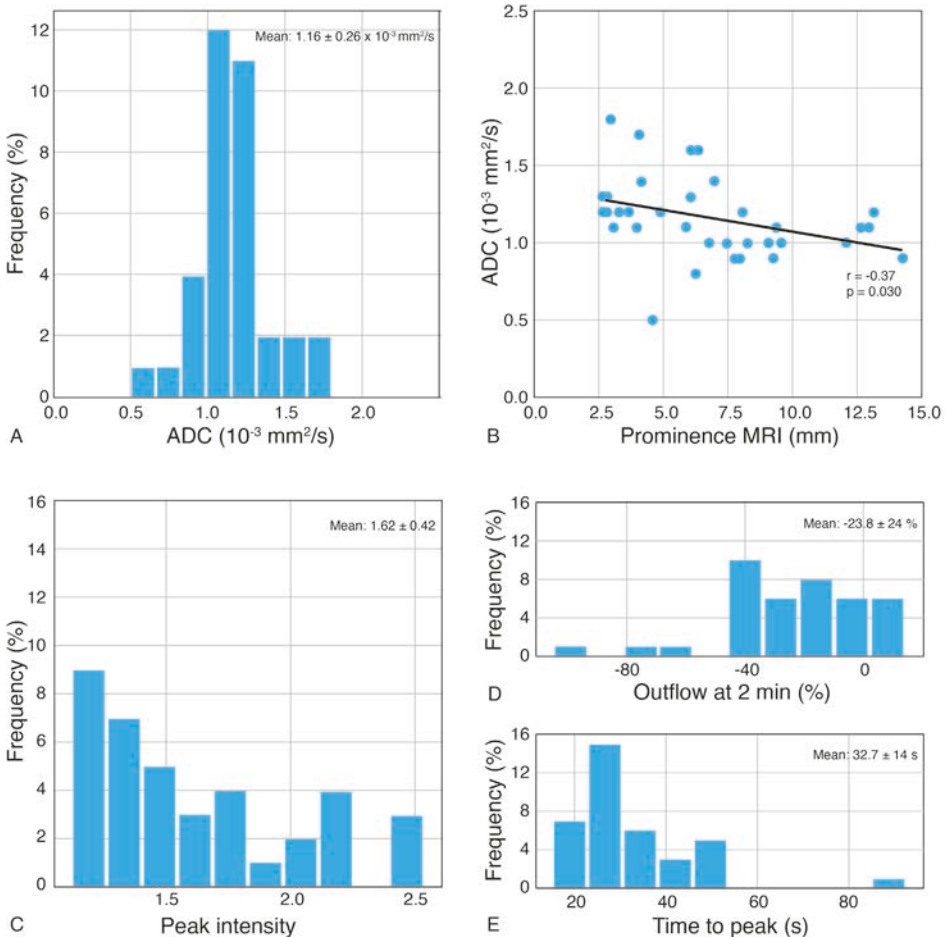


Figure 4. ADC and DCE quantitative results.

A – Histogram with ADC results of the UM (n=35).

B – Scatterplot ADC value *versus* tumor prominence (n=35), showing that larger tumors tend to have lower ADC values ($r = -0.367$; $p=0.03$).

C - Histogram with Peak intensity results.

D - Histogram with Outflow percentage 2 min results.

E - Histogram with Time to peak results.

also seen with B-Scan US. Of the other 12 enucleated eyes, one case of extrascleral extension was diagnosed on histopathology, which had been missed on MRI: this concerned a small anteriorly located lesion (maximal diameter 1.1 mm), which had already been noted clinically during slit lamp examination. Retrospectively, it was visible on MRI (Figure 7).

Optic nerve invasion - On MRI, the tumor approached the optic nerve head in fifteen patients (36%). Invasion of the postlaminal aspect of the optic nerve was seen in one patient (2%), and this was confirmed histopathologically. The invasion had not been visualized with US (Figure

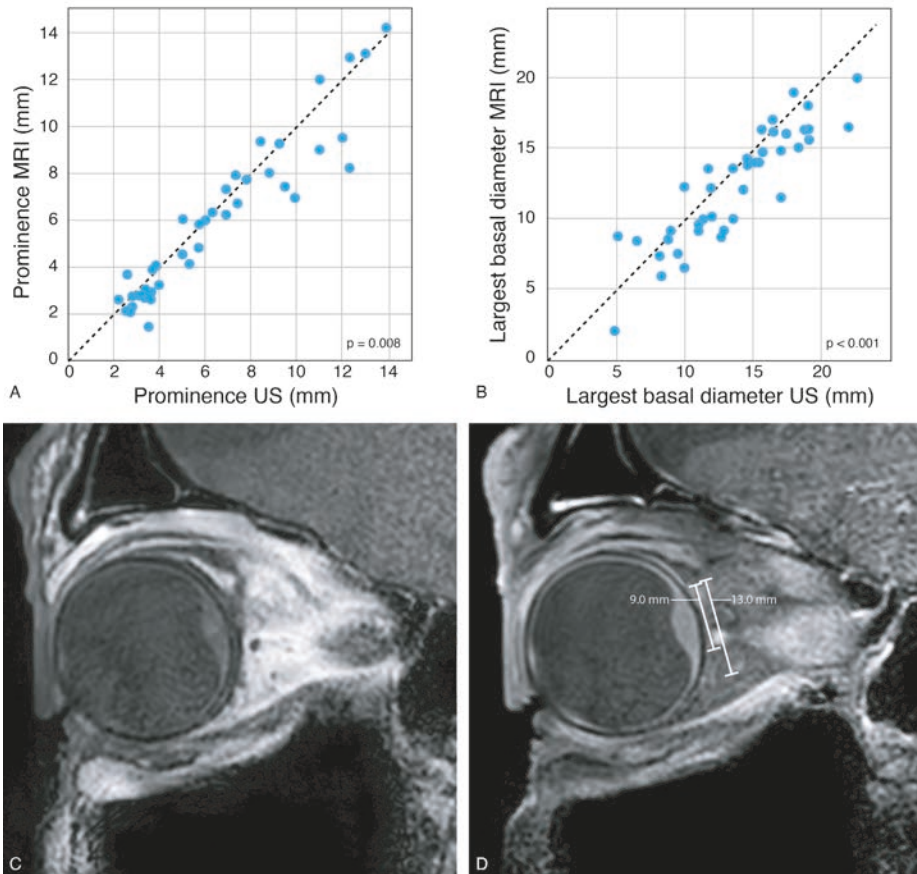


Figure 5. Comparison of tumor prominence and largest basal diameter by MRI and by US measurement with a good correlation found for both dimensions. MRI limitations on measuring the largest basal diameter in flat uveal melanomas.

A – Scatterplot tumor prominence US *versus* MRI.

B – Scatterplot tumor largest basal diameter US *versus* MRI.

C-D. MRI with sagittals MS TSE T1-WI (C) and contrast-enhanced T1-WI with fat signal suppression (D) showing different tumor basal diameters taking the peripheral flat tumor components into account or not. On MRI, a basal diameter of 9 mm was erroneously measured, while histopathology showed 14 mm. Retrospectively and taking the peripheral components of the tumor into account 13 mm were obtained.

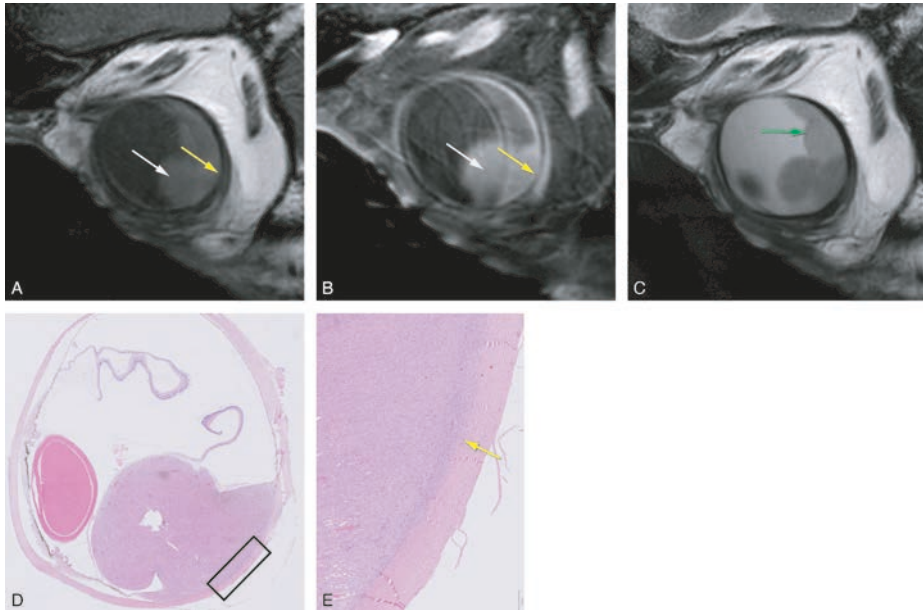


Figure 6. MR and histopathological images of a uveal melanoma with scleral invasion. A-C – MRI with sagittals MS TSE T1 (A), contrast-enhanced T1-WI with fat signal suppression (B) and T2-WI (C). Uveal melanoma (white arrow) with scleral invasion. The scleral invasion (yellow arrow) is seen as sclera enhancement and irregularity. Associated retinal detachment (green arrow). D-E – Histopathologic examination H&E with corresponding findings of scleral invasion (yellow arrow).

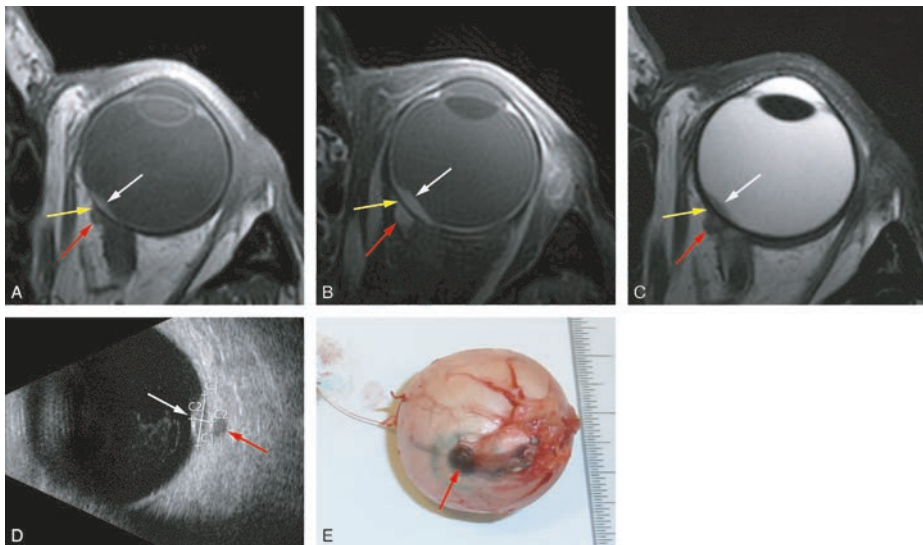


Figure 7. MR and grossing images of a uveal melanoma with extrascleral extension. A-C – MRI with axials MS TSE T1-WI (A), contrast-enhanced T1-WI with fat signal suppression (B) and T2-WI (C). Small lentiform-shape UM of the left eye (white arrow), with the extrascleral extension (red arrow) having, on all sequences, a signal intensity similar to its intraocular component. Notice the sclera, between the intra and extraocular tumor components, with a normal aspect (yellow arrow). D – B-scan Ultrasound showing the small UM (white arrow) and also clearly the extrascleral extension (red arrow). E – Enucleated eye at grossing with visible scleral and extrascleral extension (red arrow).

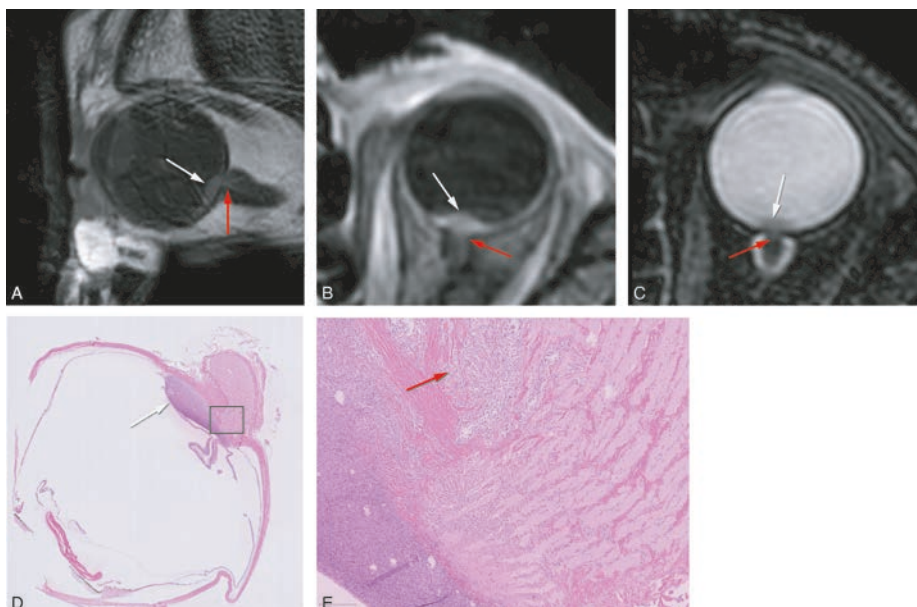


Figure 8. MR and histopathological images of a uveal melanoma with optic nerve invasion.

A-C – MRI with sagittal MS TSE T1-WI (A) and axial 3D TSE contrast-enhanced T1-WI with fat signal suppression (B) and T2-WI with fat signal suppression (C) showing a small lentiform-shape UM of the left eye (white arrow) with minimal invasion of the optic nerve (red arrow).

D-E - Histopathologic examination H&E showing the UM (white arrow) with minimal invasion of the optic nerve (red arrow).

8). In all other patients where histopathology was available (n=13), the non-involvement of the optic nerve on MRI was confirmed histopathologically.

Retinal detachment - RD was present in 62% of the UM-containing eyes on MRI, while on US it was seen in 38%: a difference of 24%. There were no cases in which US noticed RD that was not seen on MRI. RD occurred more frequently in tumors with a large prominence and in tumors with a large basal diameter.

Extracellular matrix patterns (loops) and Monosomy 3 - Ten UM (72%) showed loops, while three UM (21%) had no loops. In one patient (7%), the presence of loops could not be evaluated. All ten tumors with loops had monosomy 3 and all three tumors without loops had disomy 3.

Relation between prognostic markers and functional MRI characteristics - A significant correlation between tumor ADC and TP on MRI was found using the Pearson correlation coefficient ($r = -0.37$; $p=0.030$), with tumors with larger TP tending to have lower ADC values (Figure 4B). A significant relation between TIC type and TP on MRI was found using logistic regression, showing that an increase of the TP favors a wash-out TIC (OR=1.37, $p=0.028$). An increase of tumor ADC significantly correlated with a plateau TIC using logistic regression

(OR=0.001, p=0.011). No significant relationship between TIC type and LBD on MRI was found using logistic regression (OR=1.23, p=0.055).

UM with loops tended to have a shorter Arrival time, a shorter Time to peak and higher Peak intensities. The Outflow percentage at 2 min does not differ much in tumors with or without loops (Figure 9). There was however one UM without loops which perfusion values were similar to the ones of UM with loops. This concerned a very inflammatory and highly vascularized tumor, which probably accounted for its perfusion results.

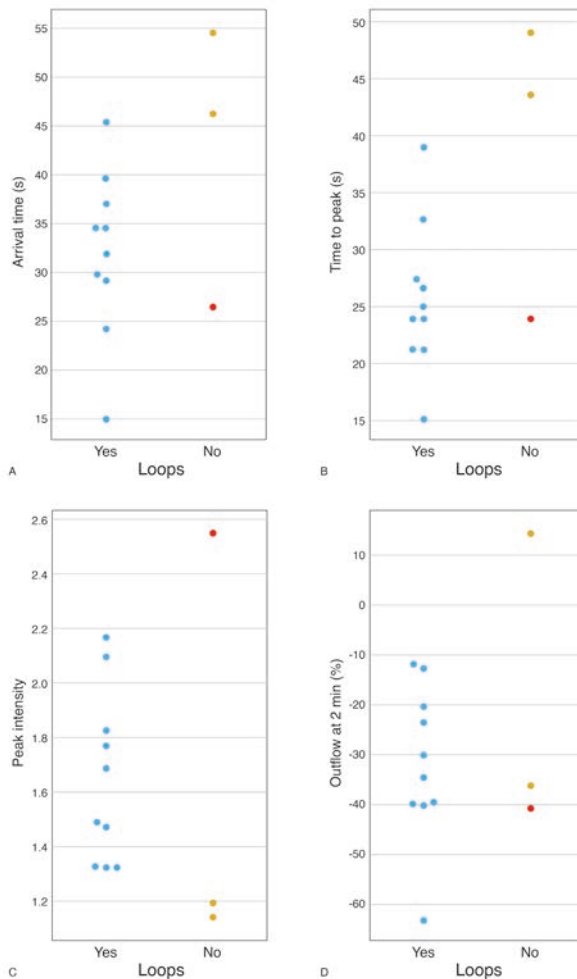


Figure 9. Comparison between the presence of loops (extracellular matrix patterns “vascular loops”) in histopathology and the perfusion parameters.

A–D. Scatterplots showing the relation between the presence of loops in histopathology and AT (A), TTP (B), PI (C) and OP2,% (D). Notice one UM without loops that, probably due its high vascularization, had perfusion values similar to the ones of UM with loops (red dots).

DISCUSSION

Imaging UM with MR requires a dedicated eye protocol consisting of: 2D MS TSE sequences, which are indispensable for delineating tumor boundaries; 3D TSE sequences, which allow retrospective reformatting in all directions and 3D reconstructions, and are essential to assess tumor geometry and accurate measurements; DWI and PWI sequences, which aid in the differential diagnosis, and potentially, provide prognostic information, predict treatment response and permit earlier assessment of tumor response to radiotherapy than US [3, 8, 11, 14–18].

UM arises in the uveal tract. Ninety percent of the UM were described to arise in the choroid, 7% in the ciliary body and the remaining in the iris [4]. However, while in small tumors the epicenter of the lesion clearly points to the origin of a UM, in larger UM, which involve the choroid as well as the ciliary body, it can be difficult to determine the primary site of the tumor. Therefore, in our study 38% of UM were classified as choroidal/ciliary body tumors. In one series with 200 UM, UM were reported to have a dome-shape in 38%, a mushroom-shape in 36% and a flat-lentiform shape in 27% [19]. It is important to be aware that the limits of flat tumors are difficult to determine with both US and MRI. Moreover, the radiotherapy planning of UM with complex tumor-shapes, such as some tumors with a mushroom configuration, is more difficult and deserves special attention [20]. The mushroom configuration is associated with breaks in Bruch's membrane [11, 21]. Our study was consistent, we showed the importance of multiplanar reconstructions with MRI in recognizing the mushroom configuration of UM and noticed a mushroom configuration mainly in large tumors.

The amount of pigmentation in UM is variable, and although pronounced pigmentation has been associated with a less favorable prognosis [19], the accurate prognostic significance of pigmentation warrants further analysis [22]. When pigmented, the distribution of melanin within the tumor can be either homo- or heterogeneous [11, 19]. When heterogeneous, frequently two different tumor components, with a different melanin content, exist and the tumor is called bipartite. Fundoscopy can only evaluate the visible superficial ventral part of the tumors [11, 19], being not representative in case of heterogeneous UM, and assessment of tumor pigmentation maybe difficult in case of retinal detachment. MRI has the advantage that it enables assessment of the distribution of the signal intensity within the whole tumor [19]. We showed that the signal intensity on T1-WI significantly correlates with tumor pigmentation, which is largely consistent with Lemke et al [19]. T1-hyperintense UM were always moderately or strongly pigmented on histopathology, while T1-hypointense UM were either pigmented or non-pigmented.

We used a non-EPI DWI TSE technique for the orbit, as it is less susceptible to the present magnetic field inhomogeneities [8], and we used a small slice thickness (2.4 mm) in order to reduce partial-volume averaging effects to a minimum. In the present study, we found a mean

ADC of $1.16 \times 10^{-3} \text{ mm}^2/\text{s}$, which is consistent with the reports from Foti et al. [3], Kamrava et al [15]. and Sepahdari et al. [23]. The study from Erb-Eigner et al. showed a lower mean ADC of $0.89 \times 10^{-3} \text{ mm}^2/\text{s}$ [24], due to the larger size of the UM (mean diameter of 14 mm), or due to the potential overall lower ADC value of their protocol (mean ADC of the vitreous of $2.76 \times 10^{-3} \text{ mm}^2/\text{s}$) [24].

Dynamic contrast-enhanced MR imaging confirms that the tumor is enhancing. That is important in some T1-hyperintense UM where one might doubt whether there is enhancement from the evaluation of the pre- and post-contrast series [8]. The time-intensity curve can be qualitatively analyzed in 3D or 2D. In homogeneous tumors, the 3D evaluation performs better as it provides information on the entire UM. However, in heterogeneous tumors, especially in bipartite tumors, different tumor components may have different TIC's and therefore a separate evaluation of both tumor components is advised. Overall, two-thirds of the UM had a wash-out curve, with a plateau curve in the other one-third, consistent with the reports from Yuan et al [14]. and Li et al. [25]. We noticed that both an increase of the tumor prominence and a decrease of the ADC favour a wash-out TIC. We found a mean Peak intensity of UM was 1.62, consistent with Buerk et al. [26].

MRI potentially plays a pivotal role at the differential diagnosis [27]. Benign ocular lesions are expected to have higher ADCs[16] and mostly a progressive or plateau TIC at DCE, although functional evaluation of choroidal nevi can still be hampered by their very small size. In other intraocular malignant lesions, such as metastases and lymphomas, the main clues for the differential diagnosis are the lesion number, configuration and signal intensity. For example, in the study from Lemke et al. with 200 UM, no tumor had a flat-placoid shape [27], which is the predominant shape of ocular metastases.

Assessment of tumor size is essential for the choice of treatment modality and planning of radiotherapy. The most accurate way to measure TP and LBD is the use of multiplanar reconstructions of isotropic 3D MR sequences [8]. Measuring the tumor's LBD with MRI is only limited in case of flat tumors, with a tendency to underestimate the size due to unclear tumor margins. In comparison to MR, US tends to overestimate tumor size, likely due to oblique measurements whenever the transducer cannot be positioned perpendicular to the tumor [2, 11, 28].

Extraocular growth is associated with an increased rate of orbital recurrence and worse survival [29, 30]. It should be diagnosed in order to be taken into account in the treatment plan. We found extrascleral extension in 7% of the UM, consistent with current literature [27, 29–31]. Interestingly, in the present study, all observed extrascleral extensions occurred in small tumors with a maximum prominence of 4.8 mm, although in general, it occurs more commonly in medium or large tumors [29, 32]. Extrascleral extension often develops along scleral canals, via perivascular or perineural invasion. Therefore the scleral underlying the tumor does not need to be invaded and the extrascleral tumor can even be located further away from the intraocular tumor [29, 30]. We had no false-positive cases with MRI, and

one false-negative case where the extrascleral extension was 1.1 mm and anteriorly located. Diagnosing extrascleral extension with MRI is more challenging at the bulbar insertion of the extraocular muscles and anteriorly adjacent to the enhancing eyelid structures, although the latter extensions are usually readily visible clinically. Venous ectasia is another pitfall but it is more serpiginous in configuration [32]. MRI has been reported to be more accurate and judged with more confidence than US in the diagnosis of extrascleral extension [32]. In our study, from the three extrascleral extensions seen with MRI, US missed one case, which corresponded to the case of optic nerve invasion.

In one series with 1527 enucleated eyes due to UM, scleral invasion was histologically present in 56% of the cases [31]. An irregular inner contour and slight enhancement of the sclera adjacent to a UM on MRI should prompt the suspicion of scleral invasion. However, contrarily to what has been previously reported [33], scleral invasion is difficult to diagnose with MRI. All cases of histopathologic proven scleral invasion were missed on MRI and only in 20% it was possible to see it retrospectively.

Optic nerve invasion is graded as prelaminar, laminar or postlaminar, if tumor cells are present in the optic nerve head, in or beyond the lamina cribrosa, respectively [34]. In the present study, MRI demonstrated or ruled out postlaminar optic nerve invasion reliably in all cases. Optic nerve invasion needs to be assessed because its presence is a contraindication for ruthenium brachytherapy and especially when it occurs postlaminar, it is associated with a propensity to orbital recurrence and poor prognosis [34].

We observed retinal detachment on MRI in 62% of the cases, more prevalent in tumors with a larger prominence and larger diameter, which is consistent with the literature [19, 27, 32]. It is important to differentiate tumor tissue from retinal detachment, especially in order to not overestimate the LBD. On MRI, retinal detachment does not enhance, there is no diffusion restriction (except when hemorrhagic), it has a lentiform shape and a typical V shape with the vertex at the optic nerve [8, 19, 24]. In our study, MRI performed better than US in depicting RD.

It would be desirable to have noninvasive markers that may predict a tumor's response to therapy and provide prognostic information. A biopsy is an invasive procedure and may not always be representative because chromosomal aberrations can be heterogeneous across the tumor [35, 36] and they seem to change with time. DWI and PWI are potentially useful but have hardly been evaluated. It is the current belief that the genetic profile governs prognosis and not the treatment modality.

Both the presence of monosomy 3 [22, 37, 38] and of extracellular matrix patterns "loops" [39–44] are important determinants of poor prognosis and they frequently coexist. All our tumors with loops had monosomy 3 and *vice versa*, consistent with the literature where monosomy 3 is detected in 67% of tumors with loops [40]. The study from Kamrava et al. found a significant correlation between monosomy 3 and perfusion values such as higher k^{trans} and v_e [15]. Interestingly, in our study, it seems that UM with loops also tend to have

different perfusion values than UM without loops, such as a shorter Time to peak and a bigger Peak intensity, consistent with the fact that extracellular matrix patterns are pseudovascular channels, seeming to conduct plasma and sometimes blood. Because Peak intensity and k^{trans} are related, our results add an extra meaning to the association described by Kamrava et al [15], corroborating the promising value of PWI in recognizing UM with a poor prognosis.

CONCLUSION

In this study, we comprehensively assessed the anatomical and functional MRI characteristics of UM. Knowing the MRI characteristics of UM is important in order to confirm the diagnosis of UM, to differentiate UM from other intra-ocular lesions and because it has implications for treatment planning. MRI is a good imaging technique for the assessment of size, shape and local extent of UM, seeming more accurate than US, and only being limited in case of flat tumors and for the diagnosis of scleral invasion. The promising value of PWI on the identification of UM at higher risk of metastasis needs further investigation, as it could serve as a substitute for histopathology in patients that undergo an eye-sparing treatment.

REFERENCES

1. Weis E, Salopek TG, McKinnon JG, Larocque MP, Temple-Oberle C, Cheng T, McWhae J, Sloboda R, Shea-Budgell M. Management of uveal melanoma: a consensus based provincial clinical practice guideline. *Curr Oncol*. 2016 Feb;23(1):e57-64.
2. Beenakker J-WM, Ferreira TA, Soemarwoto KP, Genders SW, Teeuwisse WM, Webb AG, Luyten GPM. Clinical evaluation of ultra-high-field MRI for three-dimensional visualisation of tumour size in uveal melanoma patients, with direct relevance to treatment planning. *MAGMA*. 2016 Jun;29(3):571-577.
3. Foti PV, Longo A, Reibaldi M, Russo A, Privitera G, Spatola C, Raffaele L, Salamone V, Farina R, Palmucci S, Musumeci A, Caltabiano R, Ragusa M, Mariotti C, Avitabile T, Milone P, Ettorre GC. Uveal melanoma: quantitative evaluation of diffusion-weighted MR imaging in the response assessment after proton-beam therapy, long-term follow-up. *Radiol Med*. 2017 Feb;122(2):131-139.
4. Singh M, Durairaj P, Yeung J. Uveal Melanoma: A Review of the Literature. *Oncol Ther*. 2018 Jun;6(1):87-104.
5. Carvajal RD, Piperno-Neumann S, Kapiteijn E, Chapman PB, Frank S, Joshua AM, Piulats JM, Wolter P, Cocquyt V, Chmielowski B, Evans TRJ, Gastaud L, Linette G, Berking C, Schachter J, Rodrigues MJ, Shoushtari AN, Clemett D, Ghiorghiu D, Mariani G, Spratt S, Lovick S, Barker P, Kilgour E, Lai Z, Schwartz GK, Nathan P. Selumetinib in Combination With Dacarbazine in Patients With Metastatic Uveal Melanoma: A Phase III, Multicenter, Randomized Trial (SUMIT). *J Clin Oncol*. 2018 Apr 20;36(12):1232-1239.
6. Rodrigues M, de Koning L, Coupland SE, Jochemsen AG, Marais R, Stern MH, Valente A, Barnhill R, Cassoux N, Evans A, Galloway I, Jager MJ, Kapiteijn E, Romanowska-Dixon B, Ryll B, Roman-Roman S, Piperno-Neumann S. So Close, yet so Far: Discrepancies between Uveal and Other Melanomas. A Position Paper from UM Cure 2020. *Cancers (Basel)*. 2019 Jul 22;11(7):1032.
7. Hayward NK, Wilmott JS, Waddell N, Johansson PA, Field MA, Nones K, Patch AM, Kakavand H, Alexandrov LB, Burke H, Jakrot V, Kazakoff S, Holmes O, Leonard C, Sabarinathan R, Mularoni L, Wood S, Xu Q, Wadell N, Tembe V, Pupo GM, De Paoli-Iseppi, Vilain RE, Shang P, Lau LMS, Dagg RA, Schramm SJ, Pritchard A, Dutton-Regester K, Newell F, Fitzgerald A, Shang CA, Grimmond SM, Pickett HA, Yang JY, Stretch JR, Behren A, Kefford RF, Hersey P, Long GV, Cebon J, Shackleton M, Spillane AJ, Saw RPM, Lopez-Bigas N, Pearson JV, Thompson JF, Scolyer RA, Mann GJ. Whole-genome landscapes of major melanoma subtypes. *Nature*. 2017 May 11;545(7653):175-180.
8. Ferreira TA, Fonk LG, Jaarsma-Coes MG, van Haren GGR, Marinkovic M, Beenakker J-WM. MRI of uveal melanoma. *Cancers (Basel)*. 2019 Mar 17;11(3):377.
9. Lemke, A.-J.; Alai-Omid, M.; Hengst, S. A.; Kazi, I.; Felix, R. Eye imaging with a 3.0-T MRI using a surface coil – a study on volunteers and initial patients with uveal melanoma. *Eur Radiol*. 2006 May; 16(5):1084-1089.
10. Herrick RC, Hayman LA, Taber KH, Diaz-Marchan PJ, Kuo MD. Artifacts and pitfalls in MR imaging of the orbit: a clinical review. *Radiographics*. 1997 May-Jun;17(3):707-724.
11. Foti PV, Travalì M, Farina R, Palmucci S, Spatola C, Raffaele L, Salamone V, Caltabiano R, Broggi G, Puzzo L, Russo A, Reibaldi M, Longo A, Vigneri P, Avitabile T, Ettorre GC, Basile A. Diagnostic methods and therapeutic options of uveal melanoma with emphasis on MR imaging—Part I: MR imaging with pathologic correlation and technical considerations. *Insights Imaging*. 2021 Jun 3;12(1):66.

12. Jaarsma-Coes MG, Ferreira TAG, van Haren GR, Marinkovic M, Beenakker J-WM. MRI enables accurate diagnosis and follow-up in uveal melanoma patients after vitrectomy. *Melanoma Res.* 2019 Dec;29(6):655-659.
13. Niendorf T, Beenakker J-W, Langner S, Erb-Eigner K, Cuadra MB, Beller E, Millward JM, Niendorf TM, Stachs O. Ophthalmic Magnetic Resonance Imaging: Where Are We (Heading To)? *Curr Eye Res.* 2021 Sep;46(9):1251-1270.
14. Yuan Y, Kuai XP, Chen XS, Tao XF. Assessment of dynamic contrast-enhanced magnetic resonance imaging in the differentiation of malignant from benign orbital masses. *Eur J Radiol.* 2013 Sep;82(9):1506-1511.
15. Kamrava M, Sepahdari AR, Leu K, Wang P-C, Roberts K, Demanes DJ, McCannel T, Elligson BM. Quantitative multiparametric MRI in uveal melanoma: increased tumor permeability may predict monosomy 3. *Neuroradiology.* 2015 Aug;57(8):833-840.
16. Sepahdari AR, Politi LS, Aakalu VK, Kim HJ, Razek AAKA. Diffusion-weighted imaging of orbital masses: multi-institutional data support a 2-ADC threshold model to categorize lesions as benign, malignant, or indeterminate. *Am J Neuroradiol.* 2014 Jan;35(1):170-175.
17. Foti PV, Farina R, Coronella M, Palmucci S, Montana A, Sigona A, Reibaldi M, Longo A, Russo A, Avitabile T, Caltabiano R, Puzzo L, Ragusa M, Mariotti C, Milone P, Etorre GC. Diffusion-weighted magnetic resonance imaging for predicting and detecting the response of ocular melanoma to proton beam therapy: initial results. *Radiol Med* 2015 Jun;120(6):526-535.
18. Foti PV, Travali M, Farina R, Palmucci S, Spatola C, Liardo RLE, Milazzotto R, Raffaele L, Salamone V, Caltabiano R, Broggi G, Puzzo L, Russo A, Reibaldi M, Longo A, Vigneri P, Avitabile T, Ettorre GC, Basile A. Diagnostic methods and therapeutic options of uveal melanoma with emphasis on MR imaging-Part II: treatment indications and complications. *Insights Imaging.* 2021 Jun 4;12(1):67.
19. Lemke AJ, Hosten N, Bornfeld N, Bechrakis NE, Schuler A, Richter M, Stroszczyński C, Felix R. Uveal melanoma: Correlation of histopathologic and radiologic findings by using thin-section MR imaging with a surface coil. *Radiology.* 1999 Mar;210(3):775-783.
20. Fleury E, Trnkova P, Erdal E, Hassan M, Stoel B, Jaarsma-Coes M, Luyten G, Herault J, Webb A, Beenakker J-W, Pignol JP, Hoogeman M. Three-dimensional MRI-based treatment planning approach for non-invasive ocular proton therapy. *Med Phys.* 2021 Mar;48(3):1315-1326.
21. Hainsworth P, Sommerville DN, Ranson NT, Todd KC, Gigantelli JW. Bruch's membrane abnormalities in dome-shaped and mushroom-shaped choroidal melanomas. *Ann Acad Med Singap.* 2006 Feb;35(2):87-88.
22. Berus T, Halon A, Markiewicz A, Orłowska-Heitzman J, Romanowska-Dixon B, Donizy P. Clinical, Histopathological and Cytogenetic Prognosticators in Uveal Melanoma – A Comprehensive Review. *Anticancer Res.* 2017 Dec;37(12):6541-6549.
23. Sepahdari AR, Kapur R, Aakalu VK, Villablanca JP, Mafee MF. Diffusion-Weighted Imaging of Malignant Ocular Masses: Initial Results and Directions for Further Study. *Am J Neuroradiol.* 2012 Feb;33(2):314-319.
24. Erb-Eigner K, Willerding G, Taupitz M, Hamm B, Asbasch P. Diffusion-Weighted Imaging of Ocular Melanoma. *Invest Radiol.* 2013 Oct;48(10):702-707.
25. Li DJ, Yang WL, Wang ZY, Chen W, Zhao Q, Li YF, Shen L, Wei WB. Comparative analysis on the significances of contrast-enhanced ultrasound and dynamic contrast-enhanced magnetic resonance imaging in uveal melanoma diagnosis. *Chinese J Ophthalmol.* 2018 Mar 11;54(3):194-198.

26. Buerk BM, Pulido JS, Chiong I, Folberg R, Edward DP, Duffy MT, Thulborn KR. Vascular perfusion of choroidal melanoma by 3.0 tesla magnetic resonance imaging. *Trans Am Ophthalmol Soc.* 2004;102:209–217.
27. Lemke AJ, Hosten N, Wiegel T, Prinz RD, Richter M, Bechrakis NE, Foerster PI, Felix R. Intraocular metastases: differential diagnosis from uveal melanomas with high-resolution MRI using a surface coil. *Eur Radiol.* 2001;11(12):2593–2601.
28. Schueller P, Dogan A, Panke JE, Micke O, Willich N. Does the imaging method have an influence on the measured tumor height in ruthenium plaque therapy of uveal melanoma? *Strahlenther Onkol.* 2005 May;181(5):320–325.
29. Lemaitre S, Zmuda M, Jacomet P, Lévy-Gabriel C, Dendale R, Berges O, Fréneaux P, Mariani P, Desjardins L, Galatoire O, Cassoux N. Small Choroidal Melanoma Revealed by a Large Extrascleral Extension. *Ocul Oncol Pathol.* 2017 Sep;3(3):240–246.
30. Burris CKH, Papastefanou VP, Thaug C, Restori M, Arora AK, Sagoo MS, Cohen VML. Detection of extrascleral extension in uveal melanoma with histopathological correlation. *Orbit.* 2018 Aug;37(4):287–292.
31. Histopathologic characteristics of uveal melanomas in eyes enucleated from the collaborative ocular melanoma study COMS report no. 6. *Am J Ophthalmol.* 1998 Jun;125(6):745–766.
32. Tartaglione T, Pagliara MM, Sciandra M, Caputo CG, Calandrelli R, Fabrizi G, Gaudino S, Blasi MA, Colosimo C. Uveal melanoma: evaluation of extrascleral extension using thin-section MR of the eye with surface coils. *Radiol Med.* 2014 Oct;119(10):775–783.
33. Récsán Z, Karlinger K, Fodor M, Zalatnai A, Papp M, Salacz G. MRI for the Evaluation of Scleral Invasion and Extrascleral Extension of Uveal Melanomas. *Clin Radiol.* 2002 May;57(5):371–376.
34. Lindegaard J, Isager P, Prause JU, Heegaard S. Optic Nerve Invasion of Uveal Melanoma: Clinical Characteristics and Metastatic Pattern. *Invest Ophthalmol Vis Sci.* 2006 Aug;47(8):3268–3275.
35. Dopierala J, Damato BE, Lake SL, Taktak AFG, Coupland SE. Genetic Heterogeneity in Uveal Melanoma Assessed by Multiplex Ligation-Dependent Probe Amplification. *Invest Ophthalmol Vis Sci.* 2010 Oct;51(10):4898–4905.
36. Schoenfeld L, Pettay J, Tubbs RR, Singh AD. Variation of Monosomy 3 Status Within Uveal Melanoma. *Arch Pathol Lab Med.* 2009 Aug;133(8):1219–1222.
37. Bornfeld N, Prescher G, Hirche H, Horsthemke B, Jockel KH, Becher R. Prognostic implications of monosomy 3 in uveal melanoma. *Lancet.* 1996 May 4;347(9010):1222–1225.
38. Damato B, Eleuteri A, Fisher AC, Coupland SE, Taktak AF. Artificial Neural Networks Estimating Survival Probability after Treatment of Choroidal Melanoma. *Ophthalmology.* 2008 Sep;115(9):1598–1607.
39. Broggi G, Russo A, Reibaldi M, Russo D, Varricchio S, Bonfiglio V, Spatola C, Barbagallo C, Foti PV, Avitabile T, Longo A, Caltabiano R. Histopathology and Genetic Biomarkers of Choroidal Melanoma. *Appl Sci.* 2020 10(22):8081.
40. Kivelä T, Mäkitie T, Rana'a T, Toivonen P. Microvascular loops and networks in uveal melanoma. *Can J Ophthalmol.* 2004 Jun;39(4):409–421.
41. Folberg R, Rummelt V, Parys-Van Ginderdeuren R, Hwang T, Woolson RF, Pe'er J, Gruman LM. The Prognostic Value of Tumor Blood Vessel Morphology in Primary Uveal Melanoma. *Ophthalmology.* 1993 Sep;100(9):1389–1398.
42. Mäkitie T, Summanen P, Tarkkanen A, Kivelä T. Microvascular Loops and Networks as Prognostic Indicators in Choroidal and Ciliary Body Melanomas. *J Natl Cancer Inst.* 1999 Feb 17;91(4):359–367.

Chapter 2.2

43. Folberg R, Pe'er J, Gruman LM, Woolson R.F, Jeng G, Montague PR, Moninger TO, Yi H, Moore KC. The morphologic characteristics of tumor blood vessels as a marker of tumor progression in primary human uveal melanoma: A matched case-control study. *Hum Pathol.* 1992 Nov;23(11):1298–1305.
44. Folberg R, Mehaffey M, Gardner LM, Meyer M, Rummelt V, Pe'er J. The microcirculation of choroidal and ciliary body melanomas. *Eye (Lond).* 1997;11(Pt 2):227–238.

3

Orbital inflammation



3.1

CT and MR imaging in the diagnosis of scleritis

Mariana C Diogo, Martine J Jager, Teresa A Ferreira

American Journal of Neuroradiology 2016; 37(12):2334-2339

ABSTRACT

Scleritis is a rare, underdiagnosed vision-threatening condition that can occur isolated or in association with other orbital abnormalities. The etiology of scleritis is mainly inflammatory noninfectious, either idiopathic or in the context of systemic disease. Ultrasonography remains the criterion standard in diagnostic imaging of this condition but might prove insufficient, and studies on the diagnostic value of CT and MRI are lacking. We retrospectively analyzed 11 cases of scleritis, in which CT and/or MRI were performed during the active phase of disease and assessed the diagnostic utility of these techniques. The most important imaging findings of scleritis were scleral enhancement, scleral thickening, and focal periscleral cellulitis. MR imaging is the recommended imaging technique, though posterior scleritis also can be accurately diagnosed on CT. It is important for the radiologist to be acquainted with these findings because being able to diagnose scleritis is of clinical significance and may be vision-saving.

INTRODUCTION

Scleritis is a rare but often treatable vision-threatening condition that can occur isolated or in association with other orbital abnormalities [1,2]. The most common etiology is inflammatory (noninfectious, 90% of patients), either idiopathic in the spectrum of idiopathic orbital inflammatory disease (IOID)/pseudotumor or in the context of a systemic disease [3]. Infectious scleritis is rare (7% of cases) and is associated with predisposing factors such as surgery or trauma [3,4].

Although diagnosis of scleritis is usually based on clinical assessment and ultrasonography [3,5], the variable clinical presentation, variable ultrasonography findings, and unfamiliarity with the diagnosis account for posterior scleritis being one of the most underdiagnosed conditions in ophthalmology [6].

Improvements in CT and MR techniques have led to important progress in ophthalmologic imaging [7]. However, detailed studies concerning imaging of scleritis, especially MR imaging, are few and contained only small number of patients [5,6,8-11].

This article considers the role of CT and MR imaging in the diagnosis of scleritis, emphasizing the array of imaging findings in 11 cases.

CASE SERIES

We describe a series of 11 cases of scleritis in 10 different patients. All cases had CT and/or MR imaging performed during the active phase of disease. Scleritis was confirmed by an experienced ophthalmologist by using clinical and imaging criteria and by the therapeutic response in doubtful cases.

CT was performed in 8 cases of unilateral scleritis and MR imaging in 6 unilateral and 1 bilateral case of scleritis.

Table 1 lists the clinical and diagnostic information for the 10 patients who form the basis of this report. All patients underwent laboratory testing to determine the presence of infectious and systemic inflammatory diseases.

Patient 1

A 50-year-old woman with Down syndrome presented with a 5-month history of ocular pain, proptosis, and periorbital swelling on the right orbit and low-grade fever. Contrast-enhanced CT (CECT) showed signs of pre- and postseptal cellulitis and scleritis of the right eye (Figure 1A). Infectious cellulitis was diagnosed and antibiotic therapy started. After a lack of improvement, an inflammatory etiology (IOID) was suspected and non-steroidal anti-inflammatory drugs were initiated. Complete resolution of symptoms was subsequently achieved with systemic corticosteroids.

Table 1. Clinical data of patients with scleritis analysed by CT and/or MR imaging.

Pt	Duration of Symptoms ^a	US Performed, Diagnosis	Clinical Diagnosis ^b	Imaging Modality	Systemic Disease	Final Diagnosis
1	5 mo	No	Infectious cellulitis	CT	Down Syndrome	IOID with scleritis
1	2 mo	No	Infectious cellulitis	CT	Down Syndrome	IOID with scleritis
2	3 mo	Yes, disc edema	Optic neuritis	MRI	Not found	Bilateral idiopathic scleritis
3	2 mo	No	Intraorbital mass	CT	Not found	Idiopathic scleritis
4	2 mo	Yes, uveal mass	Choroidal melanoma	CT	Not found	Nodular idiopathic scleritis
5	Acute	No	Infectious cellulitis	CT, MRI	DRM; Colon carcinoma	Infectious orbital disease with panophthalmitis
6	6 mo	No	Infectious cellulitis	CT, MRI	Down Syndrome	IOID with sclerouveitis
7	1 mo	Yes, scleritis	Scleritis or tumor	MRI	Granulomatosis with polyangiitis	Autoimmune orbital inflammation with scleritis
8	2 mo	No	Uveitis	CT, MRI	JIA	Autoimmune sclerouveitis
9	3 wk	Yes, inconclusive	Optic pathway condition	CT, MRI	None	Idiopathic scleritis
10	4 wk	No	Optic pathway condition	MRI	None	Idiopathic scleritis

Note:- DRM indicates dermatomyositis; JIA, Juvenile idiopathic arthritis; Pt, patient; US, ultrasonography

^a Duration of symptoms refers to the time elapsed between onset of symptoms of scleritis (pain, vision disturbances) and the time of imaging.

^b Diagnosis after ophthalmologic evaluation and ultrasound and before CT and/ or MRI.

Eighteen months later, the same patient re-presented with similar complaints related to the left eye. Clinically, it was again thought to be infectious orbital cellulitis. On CECT, imaging findings on the left orbit were identical to the previous findings on the right side (Figure 1B). Because of the presence of scleritis and a history of pseudotumor, recurrent IOID (with scleritis) was diagnosed and corticosteroids started, with total recovery.

Patient 2

An 11-year-old girl presented with 3 months of severe headaches that progressed to bilateral orbital pain and blurry vision. She had a history of recurrent peripheral articular pain. Ultrasonography revealed bilateral disc edema, and optic neuropathy was suspected. Gadolinium-enhanced MR imaging showed bilateral posterior scleritis (Figure 2). In the absence of infectious parameters, an inflammatory idiopathic etiology was assumed and systemic corticosteroids started, with improvement. Follow up MR imaging showed no anomalies.

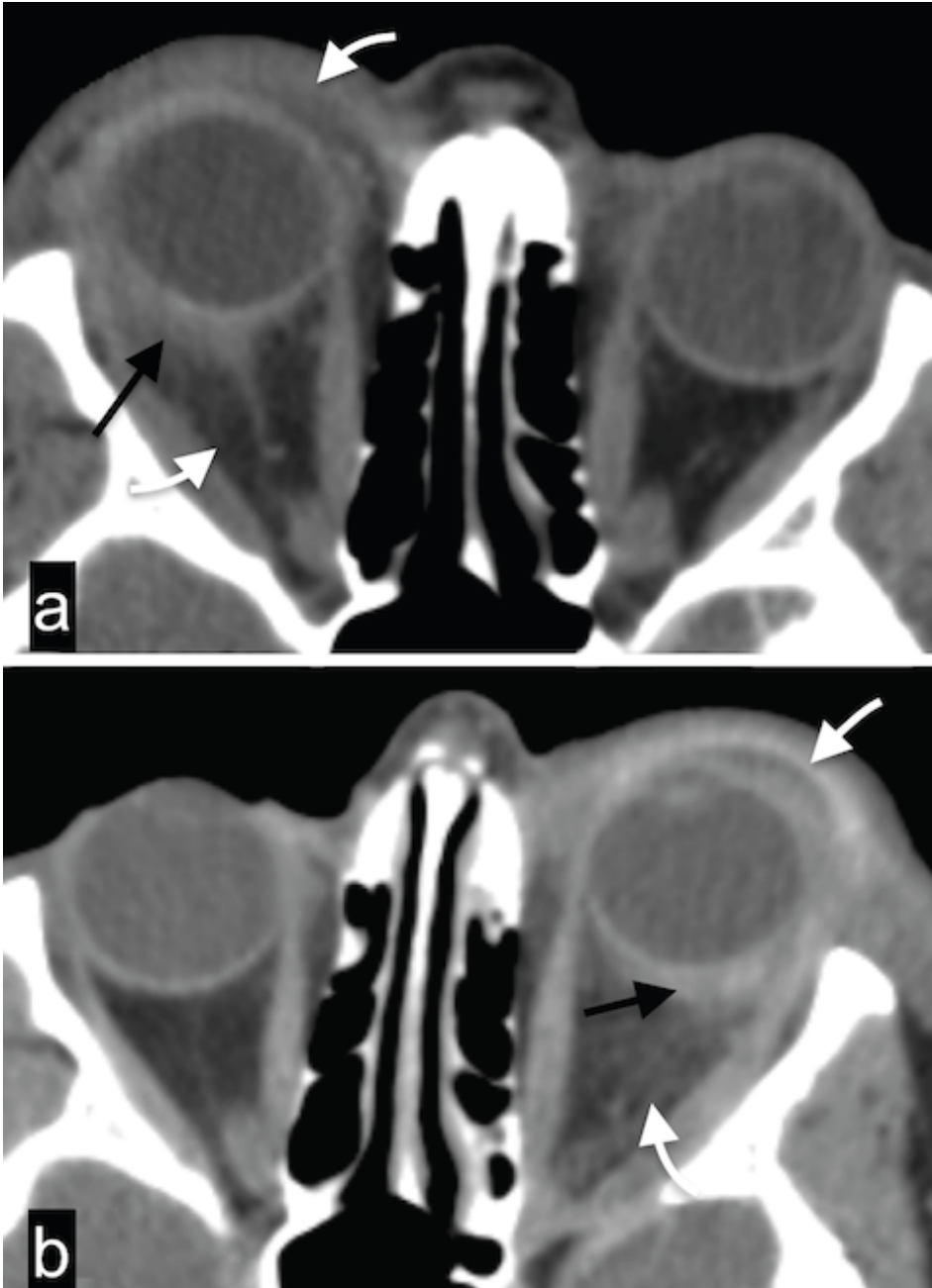


Figure 1. Asynchronous IOID with scleritis.

a, CECT depicts outward, eccentric thickening and enhancement of the right globe wall with focal periscleral cellulitis (*black arrow*), compatible with posterior scleritis. There is associated pre- and postseptal cellulitis (*white arrow*) and proptosis.

b, CECT 18 months after examination (a) shows almost identical findings in the left orbit. *Black* and *white* arrows point to the scleritis and cellulitis, respectively. Notice the complete resolution of the alterations of the right orbit.

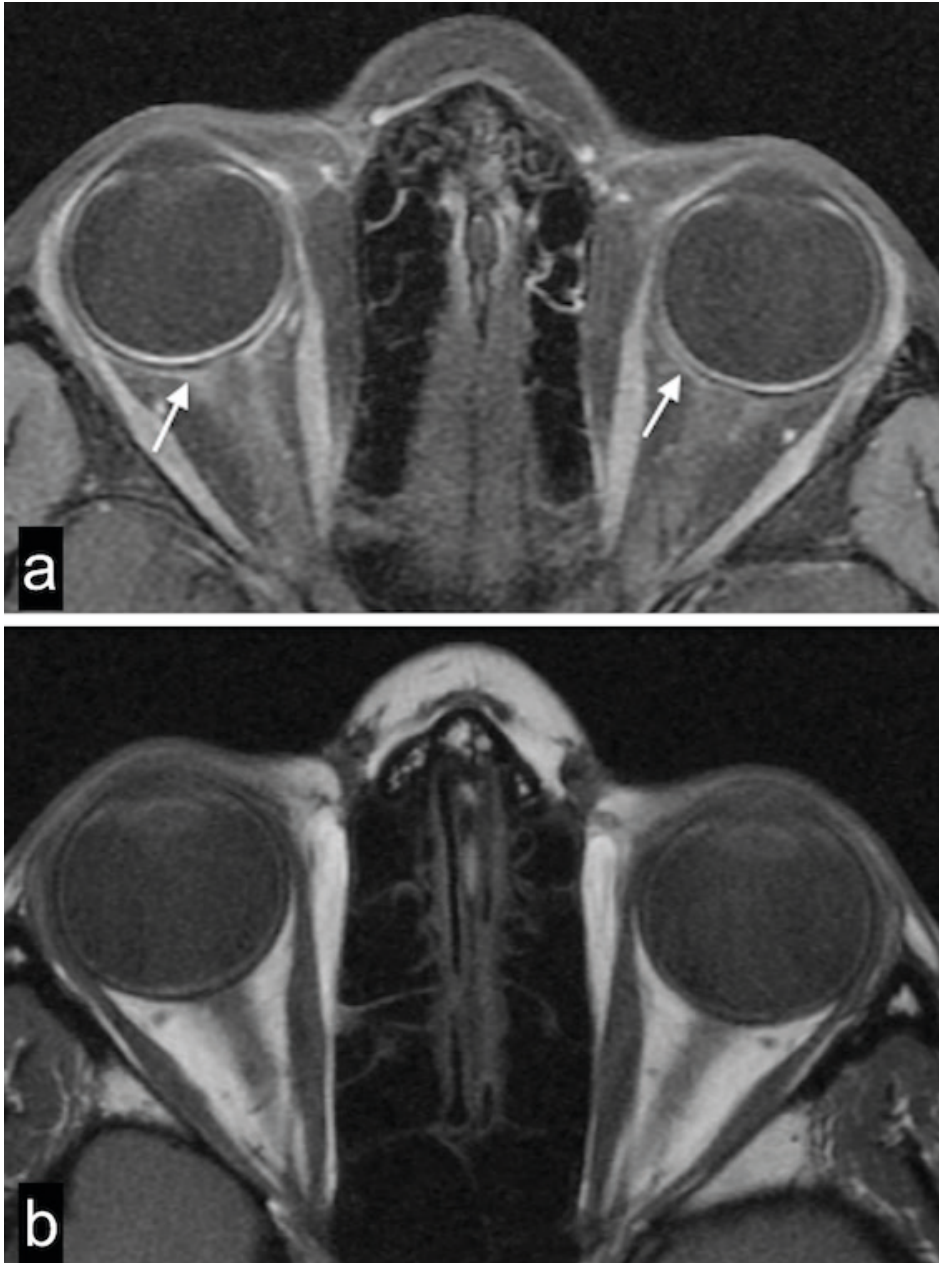


Figure 2. Bilateral inflammatory isolated scleritis. axial MRI images.
a, Post-Gd-DTPA T1-weighted image with fat saturation shows bilateral enhancement of the outer aspect of the sclera (*white arrows*), extending to the optic nerve sheath, depicting scleritis. There is also focal periscleral cellulitis. Notice the absence of ocular anomalies on the precontrast TIWI (b).

Patient 3

A 68-year-old woman presented with a 2-month history of proptosis and ocular pain on the left eye. Suspecting a retrobulbar mass, CECT was performed, depicting scleritis with periscleral cellulitis. Diagnosis of inflammatory idiopathic scleritis was made, and the patient was started on non-steroidal anti-inflammatory drugs, with clinical improvement.

Patient 4

A 41-year-old woman was referred for enucleation by an ophthalmologist with the diagnosis of uveal melanoma. She had a 2-month history of visual loss and pain in the left eye. Fundoscopy and ultrasonography findings were compatible with a mass, but because of clinical uncertainty, including the presence of pain, a CECT was performed. It showed a scleral mass displacing the choroid anteriorly, with periscleral cellulitis (Figure 3). Given the cellulitis, sparing of the choroid, and the presence of pain, a diagnosis of inflammatory idiopathic nodular scleritis was suggested. Systemic corticosteroids were started, with complete resolution of symptoms, confirming the diagnosis.

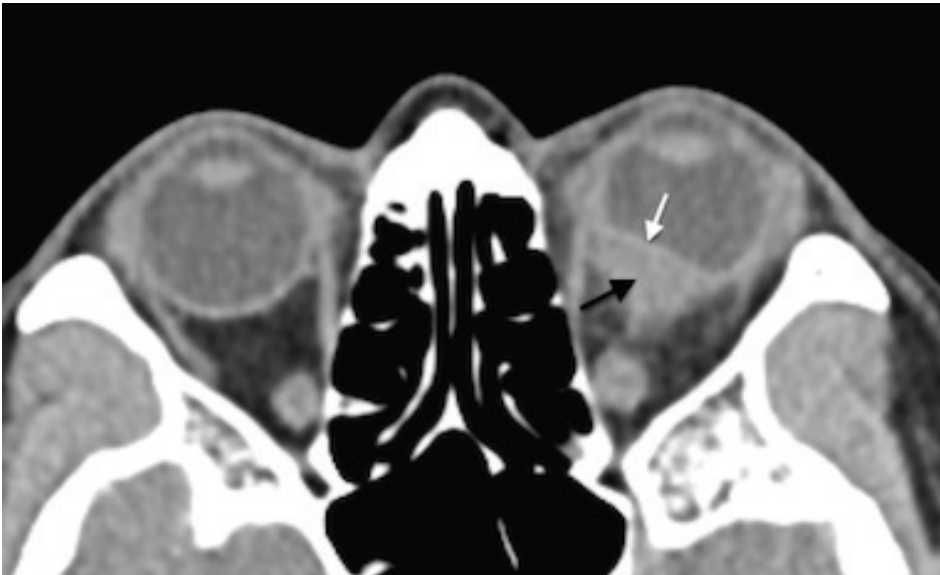


Figure 3. Nodular inflammatory scleritis mimicking uveal melanoma. CECT depicts a posterior globe wall mass (*black arrow*) deviating the choroid-retinal layer internally (*white arrow*), and hence, most probably arising from the sclera. Also notice the presence of slight periscleral cellulitis.

Patient 5

A 66-year-old woman under immunosuppression for dermatomyositis presented with sudden onset of vision loss on the left, headache, proptosis, fever, and elevated infectious parameters. MR imaging depicted pre- and postseptal cellulitis, scleritis and dacryoadenitis (Figure 4A). An orbital infection was suspected, and the patient was started on antibiotics. Despite treatment, infection progressed to panophthalmitis, and a subsequent CT showed globe rupture (Figure 4B). Cultures isolated *Clostridium septicum*.

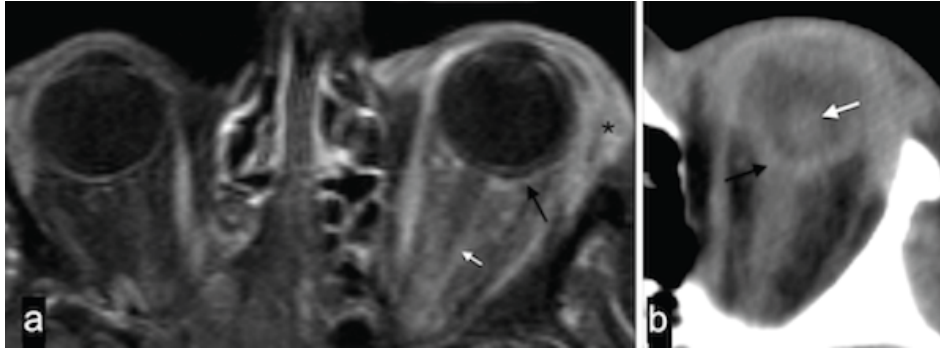


Figure 4. Infectious orbital process with scleritis followed by panophthalmitis. Post-Gd-DTPA axial T1-weighted spectral presaturation with inversion recovery image of the orbit (a) depicts scleral enhancement (black arrow) and extensive pre- and postseptal cellulitis, with involvement of the optic nerve sheath (white arrow) and dacryoadenitis (asterisk). CECT performed 48h later (b) shows lens luxation (white arrow) and inward folding of the globe wall with volume loss (black arrow), depicting globe rupture.

Patient 6

A 56-year-old woman with Down syndrome complained of progressive right eyelid swelling and proptosis. Infectious cellulitis was suspected and the patient started on antibiotics, without improvement. An inflammatory idiopathic etiology was suspected and MR imaging performed, demonstrating pre- and postseptal cellulitis, scleritis, and uveitis, with choroidal and retinal detachments. Therapy with corticosteroids was initiated, with resolution of all ocular complaints.

Patient 7

An 80-year-old woman with granulomatosis with polyangiitis (Wegener) presented with a history of left ocular pain and 1 month of left eyelid swelling. Ultrasonography identified left posterior scleritis, but because of lack of improvement on non-steroidal anti-inflammatory drugs, MR imaging was performed to exclude malignancy. It showed left scleritis (Figure 5), dacryoadenitis, and cellulitis. The findings were consistent with inflammatory autoimmune orbital disease, and corticosteroids were started. Resolution of symptoms was achieved after adding cyclophosphamide.

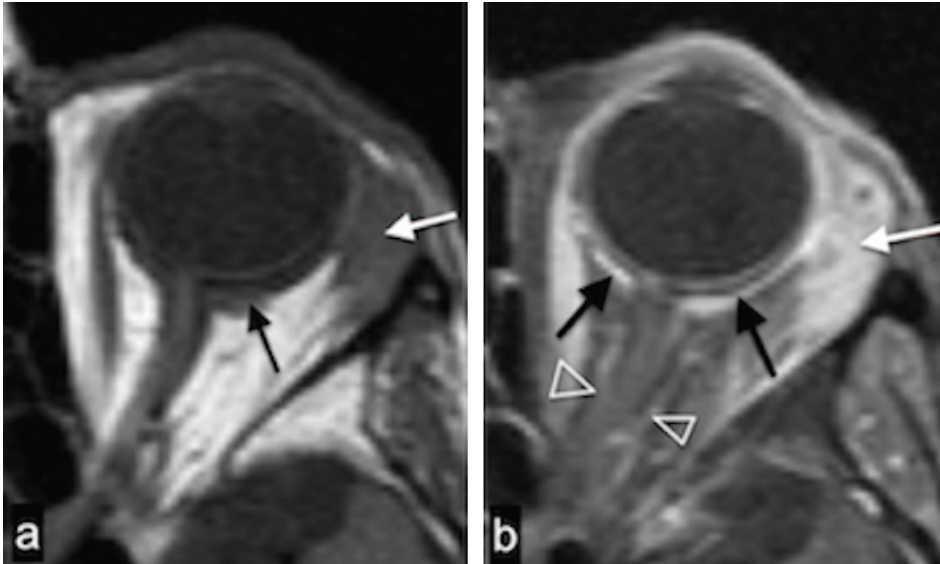


Figure 5. Orbital inflammation with scleritis in patient with granulomatosis with polyangiitis (Wegener). TIWI (a) shows eccentric focal thickening of the sclera (*black arrow*), with coexisting enlargement of the lacrimal gland (*white arrow*), both enhancing on the post-Gd-DTPA T1-weighted spectral presaturation with inversion recovery image (b). Enhancement extends to the optic nerve sheath (*open arrow heads*). This illustrates posterior scleritis with optic perineuritis, cellulitis and dacryoadenitis.

Patient 8

A 10-year-old boy with a history of idiopathic juvenile arthritis presented with ocular pain and diminished visual acuity of the left eye. Fundoscopy showed optic disc edema and signs of posterior uveitis, and orbital MR imaging depicted scleritis (Figure 6). Inflammatory autoimmune sclerouveitis was diagnosed, and corticosteroids and immunosuppressive medication were started, with clinical improvement.

Patient 9

A 47-year-old man presented with a 3-week history of headaches and blurry vision. Ultrasonography was inconclusive. CECT depicted posterior scleritis, confirmed by MR imaging (Figure 7). Assuming an inflammatory idiopathic etiology, non-steroidal anti-inflammatory drugs were started, with complete resolution of symptoms.

Patient 10

An 8-year-old boy, with headaches for 4 weeks, presented with diminished visual acuity on the right eye. An optic neuropathy was suspected, and MR imaging was performed, showing scleritis and focal periscleral cellulitis. An inflammatory idiopathic etiology was suspected and the patient started on corticosteroids and methotrexate, with visual recovery.

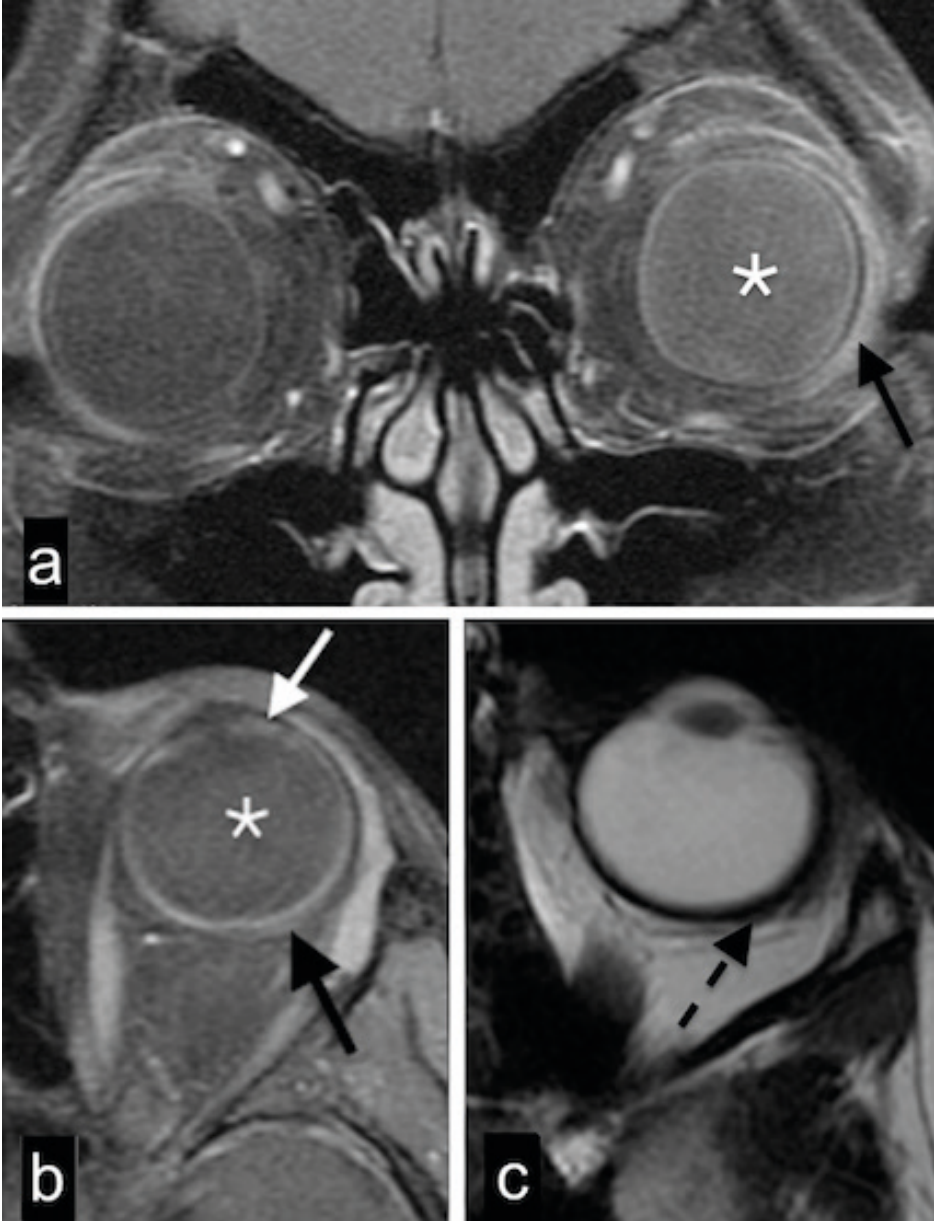


Figure 6. Scleritis with vitritis and uveitis. Enhanced coronal (a) and axial (b) T1-weighted spectral presaturation with inversion recovery images and axial T2WI (c) with a sclerouveitis. There is increased signal intensity of the vitreous on the left (vitritis; a, b, asterisk), with slight focal enhancement of the iris/ciliary body (uveitis; white arrow) and concurrent slight focal scleral outward thickening (c; black dashed arrow) and enhancement (b; black solid arrow).

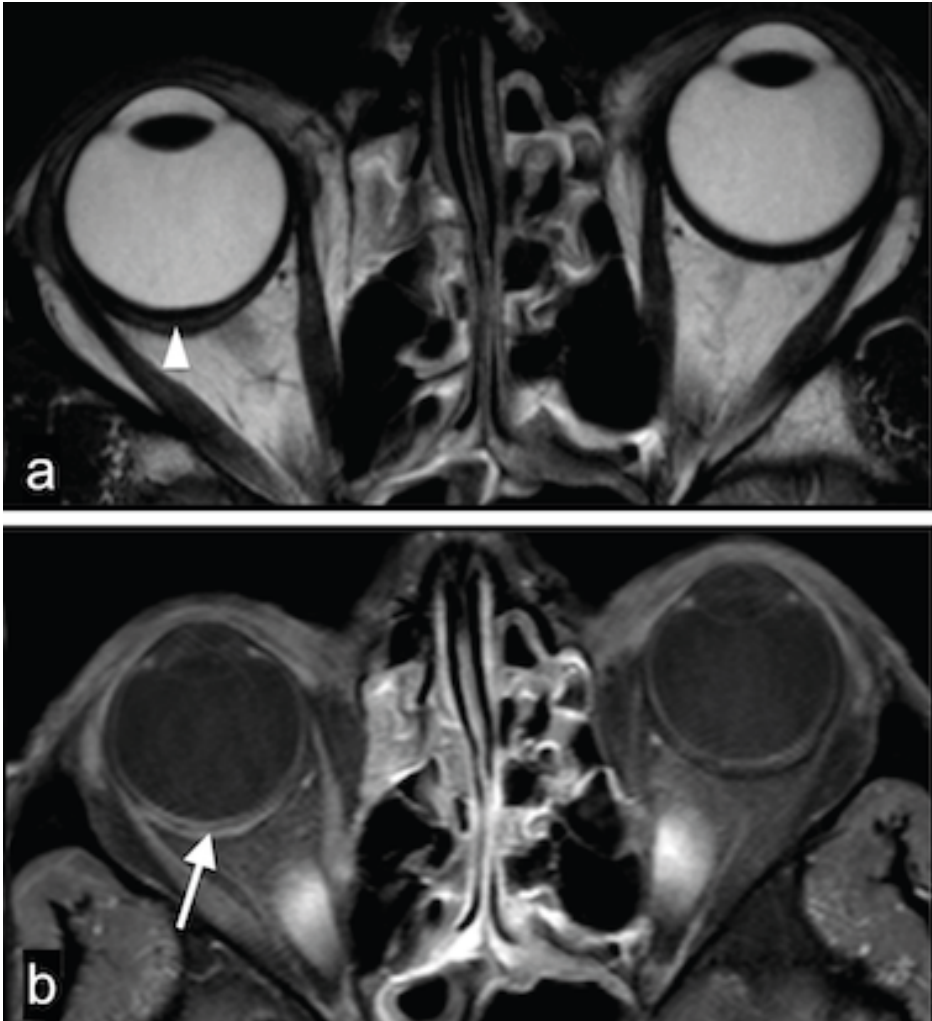


Figure 7. Isolated inflammatory scleritis: orbital MR imaging. T2-weighted (a) and Gd-DTPA enhanced T1-weighted spectral presaturation with inversion recovery (b) images depict scleral thickening and enhancement (b, *white arrow*). There is a linear hyperintense (fluid) collection between the sclera and the choroid/retina, representing a suprachoroidal effusion (a, *white arrowhead*).

DISCUSSION

Although clinically scleritis is classified according to an anterior or posterior location and subdivided into diffuse or nodular (focal) forms [12,13], there has been no defined classification applied to imaging studies. Inflammation or infection of the sclera as observed on CT or MR imaging is generally referred to as “scleritis” independent of location or etiology. Anterior scleritis is the most common form, readily diagnosed on direct observation without the need for imaging [2,12]. Posterior scleritis accounts for 2%-12% of cases and is widely

underdiagnosed because of its rarity, variable clinical findings, and unfamiliarity with this condition of the general ophthalmologist and radiologist [2,6]. The etiology of scleritis is most often inflammatory noninfectious, occurring either as an idiopathic condition (43%) or as a manifestation of a systemic disease (48%) [7,12,14], most often autoimmune. Rheumatoid arthritis and granulomatosis with polyangiitis are the most common underlying conditions. Idiopathic inflammatory scleritis might occur isolated or associated with extraocular anomalies and, we believe, as suggested by other authors [10,11,15-17], is part of the IOID/pseudotumor spectrum. We identified a systemic disease in 2 patients (granulomatosis with polyangiitis, juvenile idiopathic arthritis). In addition, 2 patients had Down syndrome, which to our best knowledge has not been specifically associated with scleritis; both patients presented with extensive IOID. Infectious scleritis is rare, particularly in the absence of predisposing factors [3,4]. In our series, 1 case was identified in an immunosuppressed patient. The most distinctive clinical feature of scleritis is orbital pain, present in around 60% of patients [3]. Orbital pain occurred in 7 of our 11 cases. From the remaining 4 cases, 3 presented with headaches. Decreased vision has been described to occur in up to 31% of patients, 3% developing permanent visual loss [1]. We found visual symptoms in 6 cases, 5 of which resolved completely with treatment. Fever is a feature in infectious scleritis. Treatment depends on etiology and, excluding infectious causes, involves nonsteroidal anti-inflammatory drugs, corticosteroids, and immunosuppressive drugs [3,18].

Correctly diagnosing scleritis is important given the potential for complications and the frequent association with systemic disease, of which scleritis might be the presenting manifestation [2,3,14]. Because the posterior sclera cannot be directly visualized, imaging methods are needed to make or confirm the diagnosis in clinically challenging cases. Sonography is the most widely used imaging technique, but often fails to show pathognomonic findings and is of limited value in evaluating other intraorbital structures [2,19]. Scleritis is frequently part of a more extensive inflammatory process, which might involve other orbital structures. In our series, sonography was performed by a specialized ophthalmologist in 4 patients and was diagnostic in 1 patient. Sonography was not performed in the remaining patients because scleritis was not clinically suspected.

MR imaging has excellent soft tissue contrast and the ability to image the entire orbit. On T2-weighted sequences, the posterior globe wall appears as a single hypointense ring, whereas on T1-weighted sequences, the sclera can be individualized as the outer hypointense rim of the globe. A distinct hyperintense and enhancing rim can be seen internal to the sclera, corresponding to the choroid, and, at least partially, to the retina (Figure 2B).

Direct signs of scleritis on imaging are scleral enhancement, scleral thickening, and focal periscleral cellulitis. Our most consistent finding was scleral enhancement, present in 100% of contrast-enhanced examinations. Enhancement might involve the whole sclera (Figure 1B) or be preferentially peripheral (Figure 2), perhaps illustrating different degrees of inflammation, starting from the vascularized outer aspect of the sclera. It also might extend along the optic

nerve sheath (Figure 5), representing optic perineuritis. Scleral enhancement is always abnormal and should not be confused with choroidal enhancement, a physiological finding. Use of contrast is critical because scleral enhancement might be the only positive finding (Figure 2) [5]. On MR imaging, postcontrast T1WI should be acquired with fat saturation because the fat signal might mask scleral enhancement. Another sign of scleritis is scleral thickening, present in 83% of our patients and easily identified on MR imaging. On CT, though the globe layers cannot be separated, we found eccentric globe wall thickening and peripheral enhancement in all patients, making CT a useful tool in the diagnosis scleritis [6,11,20]. Periscleral cellulitis, described as the “ring sign” by Chaques et al [11], is also an important sign of scleritis, found in 42% of our patients. Imaging findings are summarized in Table 2.

Table 2: Imaging findings in 11 cases with scleritis on CT (n = 8) and MRI (n = 8).

Imaging Modality	Imaging Finding	No (%)
CT	Eccentric enhancement of the globe wall	8 (100)
	Eccentric thickening of the sclerouveal rim	8 (100)
	Periscleral cellulitis	6 (75)
	Pre/postseptal cellulitis	4 (50)
	Nodular scleral tickening	1 (13)
MR	Scleral enhancement	8 (100)
	Scleral thickening	6 (75)
	Focal periscleral cellulitis	4 (50)
	Pre/postseptal cellulitis	2 (25)
	Scleral thinning	1 (13)
	Dacryoadenitis	1 (13)
	Uveitis	2 (25)
	Suprachoroidal effusion	1 (13)
Retinal detachment	1 (13)	
Choroidal detachment	1 (13)	

Indirect signs of scleritis include retinal and choroidal detachment and effusion in the suprachoroidal or Tenon spaces [6]. There might be associated uveitis [18,21], which can be differentiated from scleritis, particularly on MR imaging.

Scleritis also might be associated with extraocular orbital abnormalities, as seen in 5 of our cases, such as pre- and postseptal cellulitis, myositis, or dacryoadenitis. When scleritis occurs with anterior cellulitis, the clinical picture is often mistaken for infectious orbital cellulitis. Because extension of an orbital infection to the sclera is extremely rare in immunocompetent patients, coexistence of cellulitis and scleritis on imaging should raise suspicion of an inflammatory noninfectious etiology [3]. Other clues pointing to an inflammatory etiology include subacute/chronic complaints and absence of fever, infectious parameters, or sinusitis.

The differential diagnosis of scleritis on imaging mainly is tumor, particularly with nodular scleritis, with published cases of globe tumors misdiagnosed as scleritis [14] and scleritis mimicking a choroidal mass [8,9]. In the diffuse form of scleritis, posterior uveitis, diffuse melanoma, and lymphoma are the most relevant differential diagnoses. CT and MR imaging have proved useful in distinguishing these entities [20]. In challenging cases, a therapeutical trial (with non-steroidal anti-inflammatory drugs or steroids)[15] and/or histopathological confirmation might be warranted because misdiagnosis of scleritis have been described to lead to inadvertent enucleations [9]. In the presented case with melanoma as the presumptive diagnosis (patient 4), imaging and treatment with corticosteroids led to resolution of the mass, making a biopsy unnecessary. Clues to the inflammatory (versus neoplastic) nature of the process include the presence of pain, cellulitis as seen on imaging, and the specific scleral location, though some intraocular tumors might also involve the sclera. Additional MR sequences, such as DWI, might be of benefit [22], particularly in lymphoma, which often demonstrates restricted diffusion [23]. Neither DWI nor other advanced imaging sequences were routinely performed in our patients.

Although we present a small group of patients, they illustrate a wide range of direct and indirect imaging findings in scleritis. CT and MR imaging provided useful information and influenced clinical decision-making. MR imaging is the most useful examination in the diagnosis of scleritis [5,9], differentiating the sclera from the other ocular layers. In our experience and as ascertained by previous studies [6,11,20], CT is also able to diagnose scleritis, showing eccentric outward globe wall thickening and enhancement, frequently associated with periscleral cellulitis. Both techniques are more informative than ultrasonography for assessment of extraocular extension of disease.

We suggest that in cases when clinical evaluation and ultrasonography do not suffice in the diagnosis of scleritis, or when associated ailments are suspected, MR imaging be performed. When MR imaging is not available, or when there are contraindications, CT can be of diagnostic value.

The results of our study are limited by its retrospective nature, the small number of patients, and the lack of standardized protocol. Despite this, we believe that this article contributes to the current knowledge on imaging signs of scleritis on CT and MR imaging. To the best of our knowledge, this is the largest series of MR imaging in scleritis analyzed to date.

CONCLUSIONS

Scleritis is an underdiagnosed, treatable condition, almost invariably of inflammatory noninfectious etiology - idiopathic, in the spectrum of IOID, or in the context of a systemic disease. Imaging findings on CT and particularly on MR imaging are quite distinct and

include scleral enhancement, scleral thickening, and focal periscleral cellulitis. To the radiologist, familiarization with these findings is important to recognize this diagnosis.

REFERENCES

1. McCluskey PJ, Watson PG, Lightman S, Haybittle J, Restori M, Branley M. Posterior scleritis: clinical features, systemic associations, and outcome in a large series of patients. *Ophthalmology*. 1999 Dec;106(12):2380-2386.
2. Benson WE. Posterior scleritis. *Surv Ophthalmol*. 1988 Mar-Apr;32(5):297-316.
3. Biber J, Schwam B, Raizman M. Scleritis. In: Krachmer J, Mannis M, Holland E, editors. *Cornea* 3rd. 3rd ed. St Louis: Mosby; 2011. p. 1253-66.
4. Ho YF, Yeh LK, Tan HY, Chen HC, Chen YF, Lin HC, Chen SY, Hui-Kang D, Hsiao CH. Infectious scleritis in Taiwan—a 10-year review in a tertiary-care hospital. *Cornea*. 2014; Aug;33(8):838-843.
5. Cordero-Coma M, Garcia-Moran A, Yilmaz T, Sanchez-Campos S, Calleja-Antolin S, Martin-Escuer B, Martin S, de Morales JGR. Adjunctive globe magnetic resonance imaging in the diagnosis of posterior scleritis. *Can J Ophthalmol*. 2011 Aug;46(4):329-332.
6. Biswas J, Mittal S, Ganesh SK, Shetty NS, Gopal L. Posterior scleritis: clinical profile and imaging characteristics. *Indian J Ophthalmol*. 1998 Dec;46(4):195-202.
7. Mafee MF, Karimi A, Shah J, Rapoport M, Ansari SA. Anatomy and Pathology of the Eye: Role of MR Imaging and CT. *Radiologic Clinics of North America*. 2006;44(1):135-57.
8. Osman Saatci A, Saatci I, Kocak N, Durak I. Magnetic resonance imaging characteristics of posterior scleritis mimicking choroidal mass. *Eur J Radiol*. 2001 Aug;39(2):88-91.
9. Maggioni F, Ruffatti S, Viaro F, Mainardi F, Lisotto C, Zanchin G. A case of posterior scleritis: differential diagnosis of ocular pain. *J Headache Pain*. 2007 Apr;8(2):123-126.
10. Johnson MH, DeFilipp GJ, Zimmerman RA, Savino PJ. Scleral inflammatory disease. *AJNR Am J Neuroradiol*. 1987 Sep-Oct;8(5):861-865.
11. Chaques VJ, Lam S, Tessler HH, Mafee MF. Computed tomography and magnetic resonance imaging in the diagnosis of posterior scleritis. *Ann Ophthalmol*. 1993 Mar;25(3):89-94.
12. Okhravi N, Odufuwa B, McCluskey P, Lightman S. Scleritis. *Surv Ophthalmol*. 2005 Jul-Aug;50(4):351-363.
13. Watson PG, Hayreh SS. Scleritis and episcleritis. *Br J Ophthalmol*. 1976 Mar;60(3):163-191.
14. Kafkala C, Daoud YJ, Paredes I, Foster CS. Masquerade scleritis. *Ocul Immunol Inflamm*. 2005 Dec;13(6):479-482.
15. Gordon LK. Orbital inflammatory disease: a diagnostic and therapeutic challenge. *Eye (Lond)*. 2006 Oct;20(10):1196-1206.
16. Uehara F, Ohba N. Diagnostic imaging in patients with orbital cellulitis and inflammatory pseudotumor. *Int Ophthalmol Clin*. 2002 Winter;42(1):133-142.
17. Ding ZX, Lip G, Chong V. Idiopathic orbital pseudotumour. *Clin Radiol*. 2011 Sep;66(9):886-892.
18. Wieringa WG, Wieringa JE, ten Dam-van Loon NH, Los LI. Visual outcome, treatment results, and prognostic factors in patients with scleritis. *Ophthalmology*. 2013 Feb;120(2):379-386.
19. Benson WE, Shields JA, Tasman W, Crandall AS. Posterior scleritis. A cause of diagnostic confusion. *Arch Ophthalmol*. 1979 Aug;97(8):1482-1486.
20. Dorey SE, Clark BJ, Christopoulos VA, Lightman S. Orbital lymphoma misdiagnosed as scleritis. *Ophthalmology*. 2002 Dec;109(12):2347-2350.

21. Cheung CMG, Chee SP. Posterior scleritis in children: clinical features and treatment. *Ophthalmology*. 2012 Jan;119(1):59-65.
22. Kapur R, Sepahdari AR, Mafee MF, Putterman AM, Aakalu V, Wendel LJA, Setabutr P. MR Imaging of Orbital Inflammatory Syndrome, Orbital Cellulitis, and Orbital Lymphoid Lesions: The Role of Diffusion-Weighted Imaging. *AJNR Am J Neuroradiol*. 2009 Jan;30(1):64-70.
23. Razeq AAKA, Elkhamary S, Mousa A. Differentiation between benign and malignant orbital tumors at 3-T diffusion MR-imaging. *Neuroradiology*. 2011; Jul53(7):517-522.

3.2

CT and MR imaging of orbital inflammation

Teresa A Ferreira, Paulo Saraiva, Stijn W Genders, Mark van Buchem, Gregorius PM Luyten, Jan-Willem M Beenakker

Neuroradiology 2018; 60(12):1253-1266

ABSTRACT

Purpose: Orbital inflammation can be idiopathic or in the context of a specific disease and it can involve different anatomical orbital structures. On imaging inflammatory disease is frequently mistaken for infection and malignant tumors, and its underlying cause is often not determined. Through this article we aim to improve orbital inflammation diagnosis and underlying inflammatory diseases recognition.

Methods: The imaging protocols and characteristics of orbital inflammation were reviewed.

Results: A decision tree for the evaluation of these patients is provided. First a combination of clinical and radiological clues is used to recognize inflammation, in particular to differentiate it both from orbital infection and tumor. Subsequently different radiological patterns are recognized, often allowing the differentiation of the several orbital inflammatory diseases.

Conclusion: The use of adequate imaging protocols and subsequent evaluation allow to the recognition of an orbital lesion as inflammatory and to the diagnosis of the underlying inflammatory disease. All in all a proper treatment can be established and at times a biopsy can be avoided.

INTRODUCTION

Orbital inflammation may be either idiopathic or in the context of a specific inflammatory disease. It may involve different orbital structures, accounting for the different clinical presentations. Recognizing the inflammatory etiology of a lesion, identifying which structures are involved and determining the underlying disease is mandatory in order to establish an adequate treatment [1].

The diagnosis of orbital inflammation is made through combining the radiological findings, laboratory data and characteristics of other organ involvement. When the diagnosis still remains unclear tissue characterization and/or a therapeutical test is needed.

Despite its ability to identify orbital pathology as inflammatory and allowing for a specific diagnosis, imaging findings are often mistaken for infection and tumor [1-7].

This may be due to a number of reasons, the lack of detailed studies concerning the differential diagnosis on radiological imaging of orbital inflammatory diseases being one.

The purpose of this manuscript is to provide a comprehensive review of orbital inflammation, together with a systematic approach for the radiological evaluation of these patients, in order to improve the diagnostic accuracy of orbital inflammation.

CT and MRI protocols will be addressed first. Secondly the specific radiological characteristics of inflammation affecting the various orbital structures will be illustrated, providing the necessary clues to differentiate orbital inflammation both from orbital infection and tumor. Thirdly the imaging characteristics of specific inflammatory diseases will be presented, emphasizing the main features that will allow differentiation between distinct etiologies. Finally, a decision tree, combining mainly imaging features but also clinical findings, will be provided, which will help in the differential diagnosis of orbital inflammatory diseases.

Imaging Protocols

MRI is the modality of choice for the evaluation of orbital inflammation because of its superior soft tissue contrast and spatial resolution, as well as its possibility to generate functional images such as diffusion weighted imaging (DWI) and perfusion weighted imaging (PWI). Orbital lesions should be evaluated in multiple planes, preferably at least in axial and coronal planes. However, when a lesion is located in the eyelid, in the region of the posterior wall of the globe or in close relationship with the optic nerve, additional sagittal oblique images should be obtained for an optimal evaluation.

In general, orbital evaluation with MRI is performed by using a head coil. The MRI protocol should include T1-weighted imaging (WI) sequences and T2-WI sequences with and without a fat suppression technique, T1-WI sequences with a fat suppression technique after contrast medium administration and DWI. T1-WI and T2-WI are the standard anatomical images to be obtained. They are important to determine which orbital structures are involved and to what extent. Inflammatory lesions are hypo to isointense on T1-WI. On T2-WI sequences

the signal intensity of inflammatory lesions depends on the balance between oedema and fibrosis, oedema being hyperintense and fibrosis hypointense. The use of T2-WI sequences with fat suppression will make edema more conspicuous. Fat suppression techniques after contrast sequences allow for the differentiation between an abnormal enhancing lesion and the normal bright signal of fat on T1-WI. Enhancement pattern can be important in differentiating inflammation from tumor and infection. Inflammatory lesions will tend to show a more homogeneous enhancement pattern while tumors and infections will be more heterogeneous due to the presence of non-enhancing components such as necrosis and pus. DWI can be performed using either Echo Planar Imaging (EPI) or non-EPI-based sequences. An EPI-based sequence is the traditional choice for DWI. It has high temporal resolution but is sensitive to susceptibility artifacts and image distortion, especially present at air-tissue and bone-tissue interfaces, making it a challenging technique in the orbit. A non-EPI technique takes longer but does not show image distortions and susceptibility artifacts. DWI helps distinguishing benign from malignant lesions. In the study from *Sepahdari et al.* with 189 cases, orbital masses were likely to be malignant (> 90% probability) when $ADC < 0.93 \times 10^{-3} \text{ mm}^2/\text{s}$ and likely to be benign (> 90% probability) when $ADC > 1.35 \times 10^{-3} \text{ mm}^2/\text{s}$. Inflammatory lesions due to its higher free water content will have less diffusion restriction and therefore will show high ADC values. In the meanwhile, malignant tumors having higher cellular content will restrict water diffusion and show low ADC values. In cases of bacterial infection, the presence of pus will be responsible for restricting diffusion and consequently high signal on DWI, matching the non-enhancing portion of the mass [8,9,10]. PWI can be performed in the orbit but few studies have been published. Most used a dynamic contrast enhanced technique (DCE) in which serial T1-weighted images are acquired before, during and after contrast administration. It provides data in the wash-in and wash-out contrast kinetics within a lesion. In DCE-MRI the qualitative evaluation of the time intensity curve (TIC) pattern seems to be a complementary investigation in distinguishing benign from malignant lesions. In the study from *Yuan et al.*, a persistent TIC pattern (type I curve) suggests a benign lesion, a wash-out TIC pattern (type III curve) mostly suggests malignancy, and a plateau TIC pattern (type II curve) occurs both in benign and malignant lesions [11]. In an emergency setting, computed tomography (CT) is often the first-line imaging modality because of its availability, high temporal resolution and allowing oftentimes the diagnosis of a mass lesion. It may also identify a metallic foreign body that could become harmful during MRI examination. However, CT diagnostic performance compares negatively with MRI, namely in the differentiation between inflammation and tumor, as it lacks the information obtained through DWI and due to its worse soft tissue contrast and spatial resolution. Ultrasonography is another alternative imaging method to diagnose inflammation or tumors of the globe in selected cases, but the technique is operator dependent and shows limited capacity in the evaluation of the retrobulbar structures [12,13].

Characteristics of Orbital Inflammation involving different Orbital Structures

Although infection may cause inflammation, in this paper when referring to inflammatory disease we are considering non-infectious inflammation.

Orbital inflammation may involve one or several orbital structures [1]. Table 1 summarizes the main imaging features in inflammation related to the different orbital structures.

Table 1. Imaging characteristics of inflammation involving different orbital structures.

Orbital Inflammation/Orbital Structure	Imaging Characteristics
Scleritis (Figure 1)	Scleral enhancement, scleral thickening, no DWI restriction, focal periscleral cellulitis
Uveitis (Figure 2)	Uveal tract increased enhancement, uveal tract thickening, no DWI restriction, subretinal effusions, vitreous humor signal abnormalities
Dacryoadenitis (Figure 3)	Lacrimal gland enlargement both involving the orbital and palpebral lobes, no DWI restriction, surrounding cellulitis
Optic perineuritis (Figure 4)	Optic nerve sheath enhancement, no DWI restriction, surrounding cellulitis
Optic neuritis	Optic nerve enhancement and hyperintensity on T2 and FLAIR, DWI restriction possible
Myositis (Figure 5)	Muscle enlargement, with increased enhancement, no DWI restriction, tubular/fusiform configuration, surrounding cellulitis
Cellulitis (Figure 6)	Preseptal fat thickening, pre and postseptal fat infiltration and enhancement, no DWI restriction

Scleritis is an inflammation or infection of the sclera. The most common etiology is inflammatory, either idiopathic (43%) or in the context of a systemic disease (48%), most usually rheumatoid arthritis or granulomatosis with polyangiitis [12,14]. Infectious scleritis is rare (7%) and is associated with predisposing factors such as surgery or trauma [11]. The diagnosis of scleritis is usually based on clinical assessment with intense and localized pain, with or without choroidal folds on fundoscopy and scleral thickening on ultrasonography. Image evaluation should be performed with MRI. MRI findings are quite distinct and include scleral enhancement, scleral thickening and focal periscleral cellulitis, with no DWI restriction. Scleritis can be diffuse or less common nodular, the latter with a mass-like lesion in the wall of the globe (Figure 1) [12]. Uveitis is an inflammation or infection of any part of the uveal tract, comprising the iris anteriorly, the ring-shaped ciliary body and the choroid posteriorly. When inflammatory, uveitis is either idiopathic or in the context of a systemic disease, such as HLA-B27 associated seronegative spondylarthropathies, rheumatoid arthritis and sarcoidosis [15]. The diagnosis of uveitis is predominantly based on clinical symptoms, such as pain, photophobia, decreased vision and on slit lamp biomicroscopy and fundoscopy the presence of cells and flare in the vitreous and anterior chamber respectively. If image evaluation is considered it should be through MRI. MRI signs of uveitis include increased enhancement and/or thickening of the uveal tract, subretinal effusions and vitreous humor

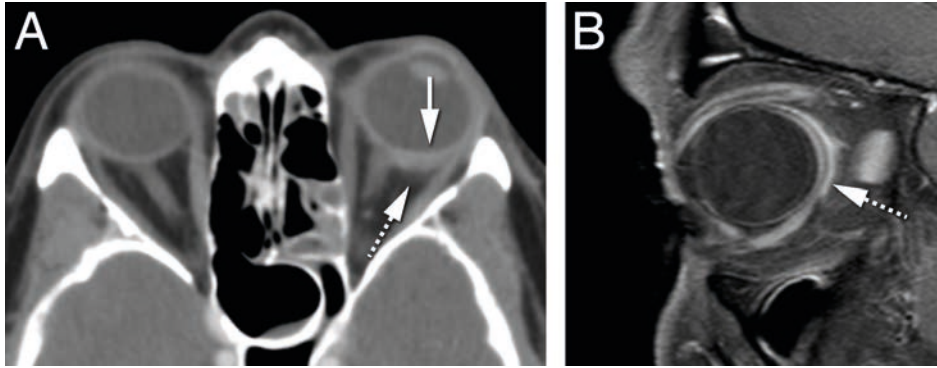


Figure 1.

A. 69 y/o female. Inflammatory scleritis on the left. Axial contrast enhanced CT (CECT): focal eccentric thickening and enhancement of the globe wall (arrow) and slight periscleral cellulitis (dashed arrow). The outward eccentric thickening of the globe wall points to involvement of the sclera.

B. 38 y/o male. Idiopathic inflammatory scleritis on the right. Enhanced sagittal T1 WI with fat signal suppression: scleral thickening and enhancement (dashed arrow) consistent with scleritis. Contrary to CT, MRI clearly depicts which ocular layer is enhancing.

signal abnormalities, with no DWI restriction (Figure 2) [15]. On imaging inflammatory scleritis and infectious scleritis are alike, as are inflammatory and infectious uveitis. Inflammatory scleritis looks similar whatever the underlying inflammatory disease is, the same holding true when inflammatory uveitis is considered. Nodular scleritis and nodular uveitis need to be differentiated from a tumor [16,17]. On both cases the presence of pain and lack of diffusion restriction on MRI should raise the suspicion of an inflammatory or infectious condition. Moreover, the presence of periscleral cellulitis and a located scleral mass both favor the diagnosis of nodular scleritis over tumor [12].

Dacryoadenitis is an inflammation or infection of the lacrimal gland. It can be acute such as due to infection or idiopathic orbital inflammation or chronic related to sarcoidosis, Sjogren syndrome, granulomatosis with polyangiitis, Graves' disease and IgG4 related disease. Clinically, it is characterized by swelling of the lateral third of the upper eyelid, as well as redness and, especially in case of acute presentation, pain. On CT and MRI, a diffuse enlargement of the gland is observed, maintaining its normal almond shape and involving both the orbital and palpebral gland lobes [2]. Surrounding cellulitis is possible, with blurring of the glandular margin and possibly involving the adjacent muscles [1,2,18]. There can be a tapered posterior margin of the gland until the apex (Figure 3A) [2]. On imaging inflammatory and infectious dacryoadenitis look similar. Furthermore, inflammatory dacryoadenitis looks similar whatever the underlying cause is. Dacryoadenitis must be differentiated from a tumor. A benign tumor will be confined to the orbital lobe, with no surrounding cellulitis and no invasion of adjacent structures [2]. A malignant tumor has no surrounding cellulitis and has diffusion restriction. In cases of infectious dacryoadenitis with abscess formation restricted diffusion is also expected. Lymphomas can, just as dacryoadenitis, involve both the orbital and palpebral lobes and have a tapered posterior margin until the apex, but unlike

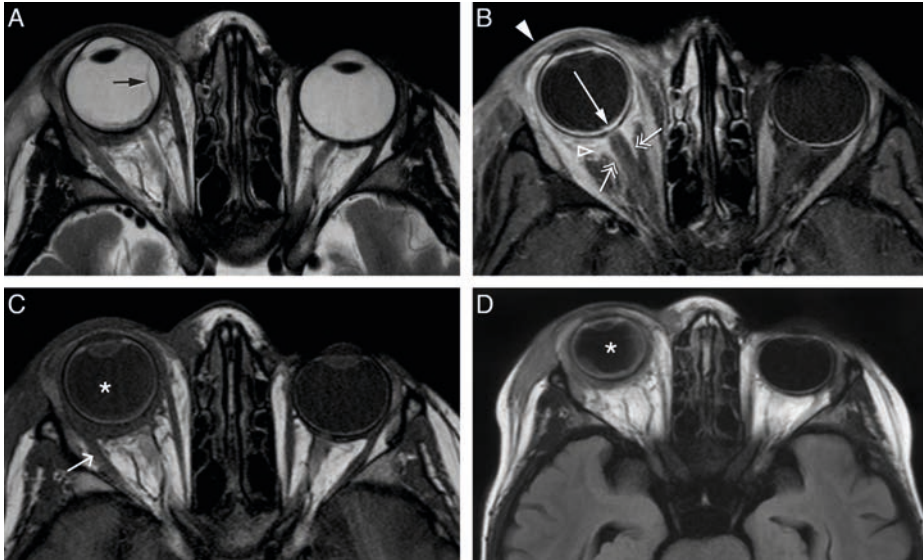


Figure 2.

8 y/o male with graft versus host disease after stem cell transplant. Extensive orbital cellulitis, myositis involving the lateral rectus and sclerouveitis on the right. Axial T2 WI (A), axial T1 WI (C), enhanced axial T1 WI with fat signal suppression (B), and axial FLAIR (D): increased thickness and enhancement of the whole uvea consistent with uveitis (long arrow), subretinal effusions (black arrow) and slight increased signal intensity of the vitreous humor signal on T1 and FLAIR consistent with vitritis (asterisk). Extensive periscleral cellulitis due to scleritis (empty arrowhead), preseptal cellulitis (arrowhead), myositis of the lateral rectus (short arrow) and perioptic neuritis (double headed arrows).

dacryoadenitis lymphomas have diffusion restriction. When dacryoadenitis is bilateral the differential diagnosis includes idiopathic orbital inflammation, *Graves'* disease, sarcoidosis, *Sjogren* syndrome, IgG4 related disease or granulomatosis with polyangiitis (Figure 3B) [19]. Optic perineuritis (OPN) and optic neuritis (ON) have been considered different entities, the first affecting the optic nerve sheath and the second the optic nerve itself [2,20]. It is important to distinguish them because they tend to have different etiologies. OPN is either inflammatory, infectious or idiopathic, while ON is demyelinating, idiopathic or in the context of the neuromyelitis optica spectrum disorder [20,21]. Clinically OPN is difficult to differentiate from ON, both presenting with vision loss, pain with eye movement and either a normal or swollen optic disk. OPN has a broad age distribution with most patients being above 50-years-old. ON tend to affect younger adults, especially females [20]. Image evaluation should be performed with MRI. In OPN there is enhancement of the optic nerve sheath, with the characteristic tram-track sign on axial and sagittal images and the donut sign on coronal sequences. Surrounding cellulitis is a possible other feature in OPN (Figure 4) [2,20]. In ON the enhancement and hyperintensity on T2 and FLAIR sequences are located in the nerve itself [20]. This differentiation may also have important therapeutic and prognostic implications [21]. With the potential serious side-effects associated with high-dose systemic steroid therapy, some clinicians may choose not to prescribe steroids for typical multiple

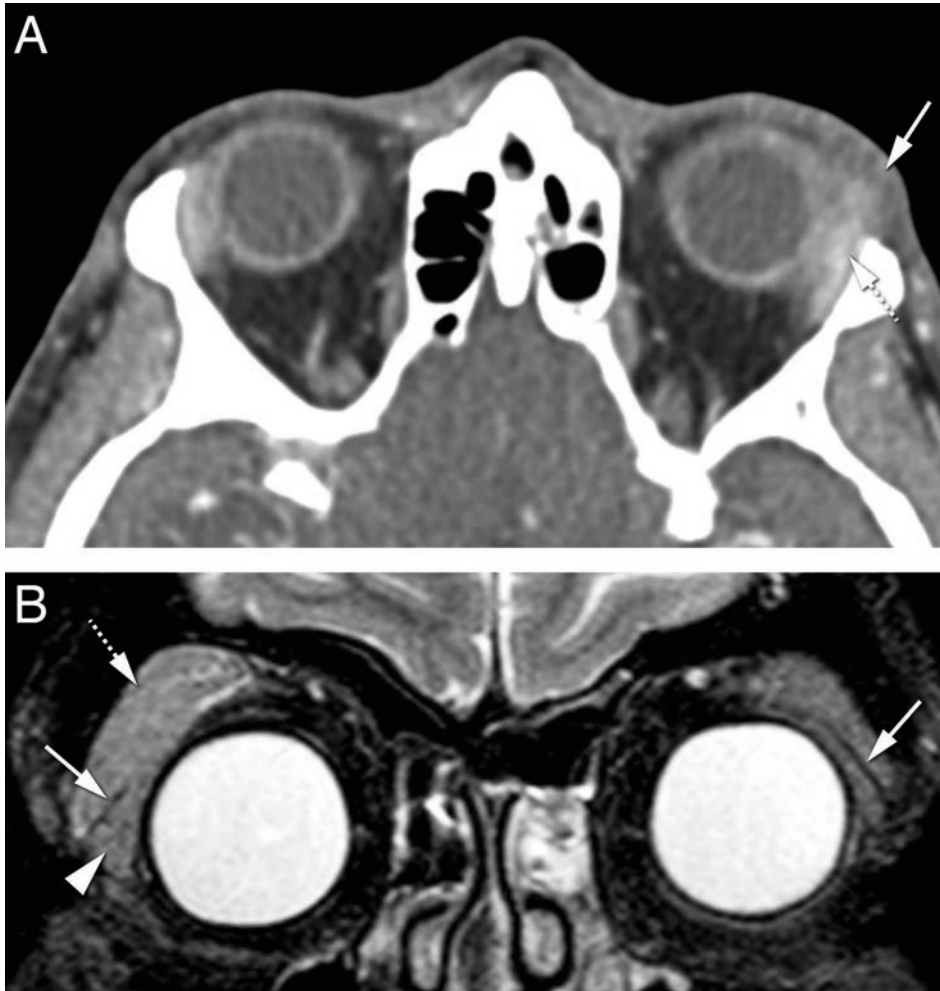


Figure 3.

A. 68 y/o male with *Stills' disease*. Inflammatory dacryoadenitis on the left. Axial CECT: enlarged lacrimal gland (dashed arrow) with slight blurred margin and preseptal cellulitis (arrow) consistent with dacryoadenitis. The coexistence of preseptal cellulitis makes the diagnosis of tumor not probable.

B. 54 y/o female with *Sjogren's disease*. Bilateral inflammatory dacryoadenitis. Coronal T2 WI with fat signal suppression: bilateral enlargement of the lacrimal gland, involving both the orbital (dashed arrow) and palpebral (arrowhead) lobes, a feature typical of dacryoadenitis but that can also occur in lymphomas. The levator palpebrae tendon separating the orbital and palpebral lobes (arrows).

sclerosis related ON, particularly as steroid therapy has been shown not to positively affect long term visual acuity [21]. On the other hand, early initiation of steroid treatment for OPN is essential to prevent irreversible visual loss and recurrence. OPN typically does not naturally resolve [21]. ON must be distinguished from optic ischemic neuropathy as well. Differentiation is not straightforward. Enhancement is more commonly seen with ON while lower ADC is more typical of ischemic neuropathy [22,23]. OPN must be distinguished from meningioma,

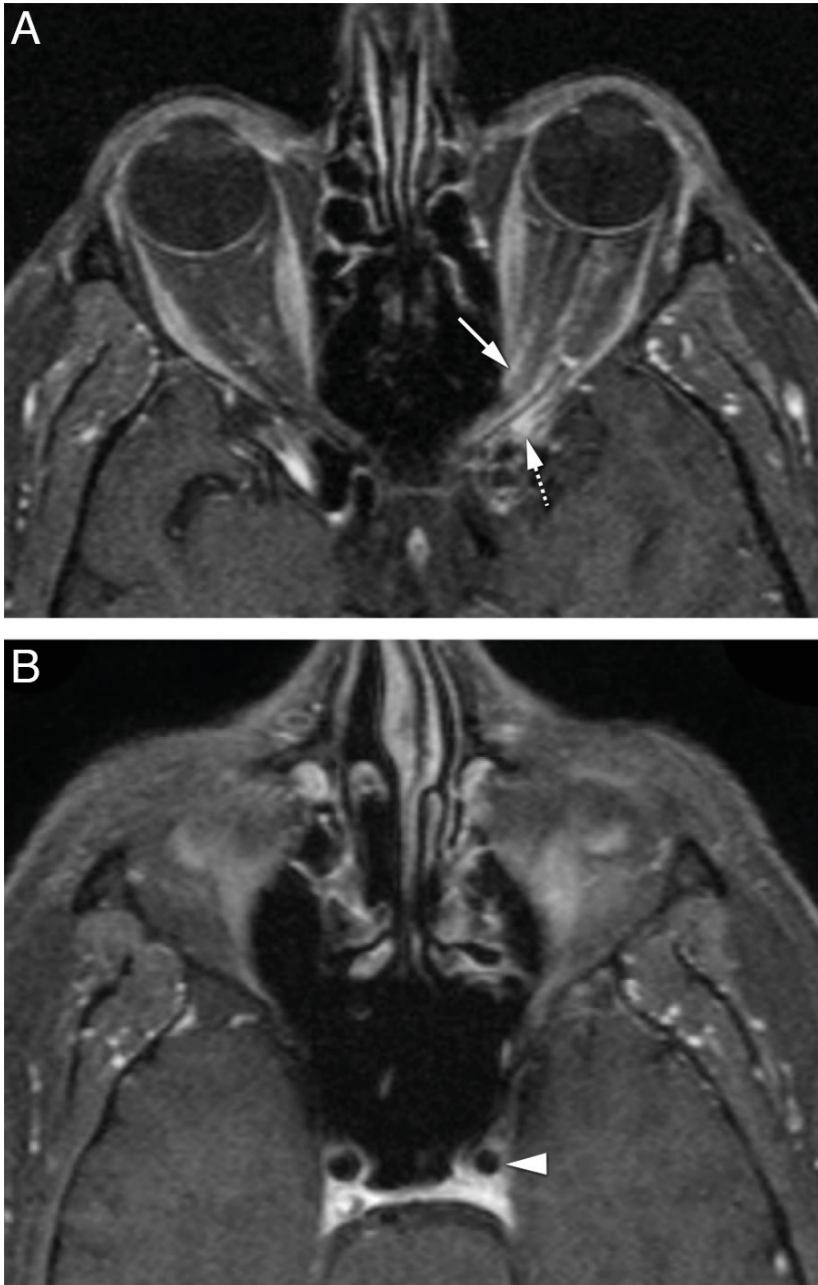


Figure 4.

40 y/o male with *Tolosa-Hunt* disease.

A. Optic perineuritis on the left at the orbital apex. Enhanced axial T1 WI with fat signal suppression: tram-track sign (arrow) and slight streaky enhancement of the surrounding fat consistent with peri optic neuritis. Slight orbital apical enhancement (dashed arrow) keeping with *Tolosa Hunt* disease.

B. Enhanced axial T1 WI with fat signal suppression at the level of the carotid siphons: smaller internal carotid artery on the left (arrowhead), due to pericarotid inflammatory tissue, a known finding in *Tolosa-Hunt* disease.

the latter being usually thicker, may show calcifications and there may be hyperostosis of the optic canal. Meningiomas will not typically respond to steroids [2].

Myositis is an inflammation or infection of the muscle. One or more muscles can be simultaneously involved. Clinically it is characterized by prominent pain especially with eye movement. On CT and MRI, the involved muscle/s is enlarged, there is too much enhancement and in case MRI is performed no diffusion restriction is expected. Surrounding cellulitis is possible and the signal on T2-WI is variable depending on etiology (Figure 5). On imaging an inflammatory myositis looks similar to an infectious myositis. In case of an inflammatory myositis some clues will point the underlying inflammatory etiology. Idiopathic orbital inflammation involves especially the medial, followed by the superior and lateral recti, the muscle has a tubular configuration and there is frequently surrounding cellulitis [2,18]. *Graves'* disease is typical bilateral, the superior oblique and lateral recti are relatively spared and the muscles have a fusiform configuration [2]. On IgG4 related disease muscle involvement is typically bilateral, the lateral rectus is the most commonly affected, muscles have a fusiform aspect and there can be surrounding cellulitis [24]. A myositis also needs to be differentiated from a tumor such as lymphoma or metastasis. The presence of pain, surrounding cellulitis and the absence of diffusion restriction are suggestive of inflammation or infection [2].

Orbital cellulitis refers to orbital fat inflammation or infection. It can be pre or postseptal [2]. Clinically, preseptal cellulitis presents with swollen, reddish and painful eyelids, while in postseptal cellulitis proptosis, restriction of eye movements and disturbed pupillary reflexes may exist. Signs of cellulitis are easy to appreciate on CT and MRI and include thickening of the fat, best appreciated on the preseptal space, fat infiltration and contrast enhancement. On MRI the signal on T2-WI is variable depending on the etiology. Inflammatory cellulitis is frequently confused with infectious cellulitis. On imaging the presence of sinusitis or abscess suggests infection, while the presence of scleritis points to inflammation (Figure 6) [2,12].

Inflammation will sometimes present as a focal solid enhancing mass, which can be located anywhere in the orbit [2]. There is no diffusion restriction and surrounding cellulitis may exist. The clinical symptoms and signs are dependent of the anatomical location of the mass, but pain is frequently present. The main differential is tumor [2,12]. The presence of pain, surrounding cellulitis and absence of diffusion restriction will point to inflammation. As been said if the mass is in the globe wall originating from the sclera, the diagnosis of inflammation will be favoured (Figure 7) [12].

Characteristics of Orbital Inflammation due to Different Inflammatory Diseases

Orbital inflammation can have a wide range of underlying etiologies. It can be idiopathic, or in the context of *Graves'* disease, sarcoidosis, granulomatosis with polyangiitis, IgG4 related disease or sclerosing orbital inflammation [25]. More rarely it is associated with other systemic diseases such as *Erdheim-Chester* [1]. Over the past decade therapeutic options in orbital inflammatory disease have evolved markedly, from prednisone and cyclophosphamide, still

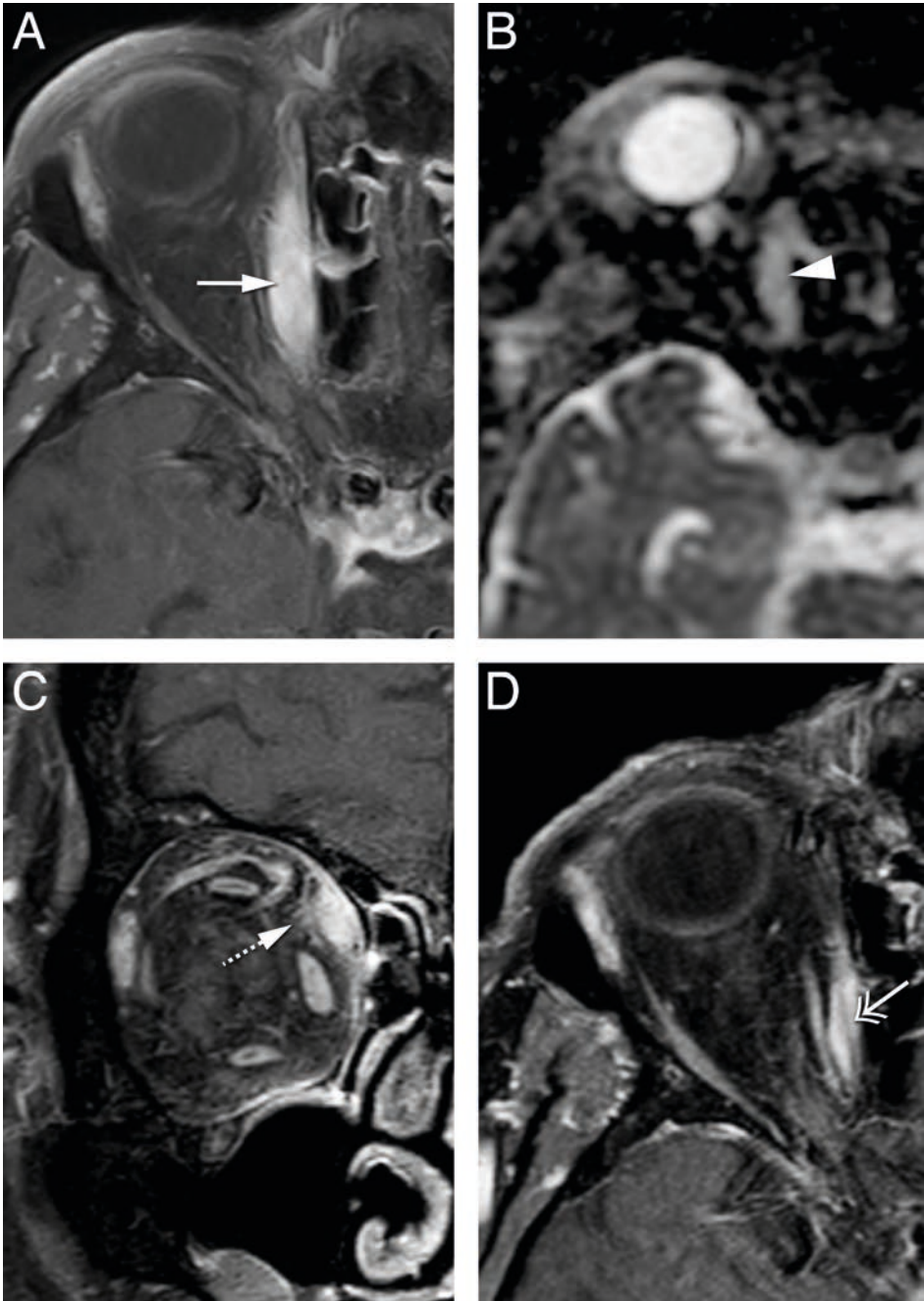


Figure 5.

68 y/o male. Inflammatory myositis of the right superior oblique muscle. Enhanced axial T1 WI with fat signal suppression (A and D), axial ADC (B) and enhanced coronal T1 WI with fat signal suppression (C): enlarged and with marked contrast enhancement right superior oblique muscle (arrow), with no DWI restriction (arrowhead) and slight surrounding cellulitis (dashed arrow), favoring inflammation. Clinically not suspicious for infection. Improvement after corticosteroids (D) avoiding biopsy (double headed arrow).

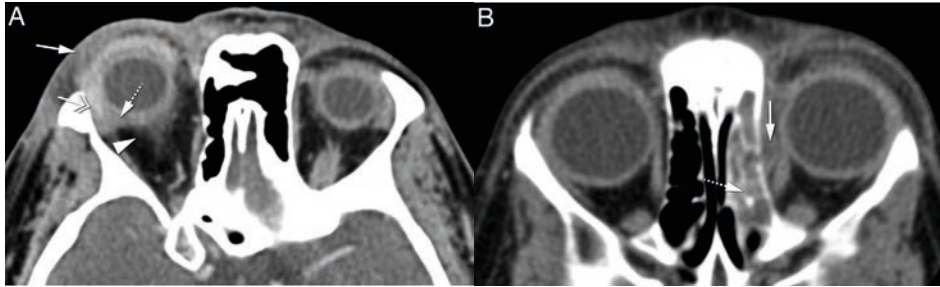


Figure 6.

A. 46 y/o female with idiopathic orbital inflammation on the right. Axial CECT: pre (arrow) and postseptal cellulitis (arrowhead), scleritis (dashed arrow) and dacryoadenitis (double headed arrow). Scleritis and no sinusitis favored inflammation over infection.

B. 5 y/o male. Axial CECT: pre and postseptal cellulitis on the left. Ethmoiditis (dashed arrow) and subperiosteal abscess (arrow), both favoring an infectious etiology.

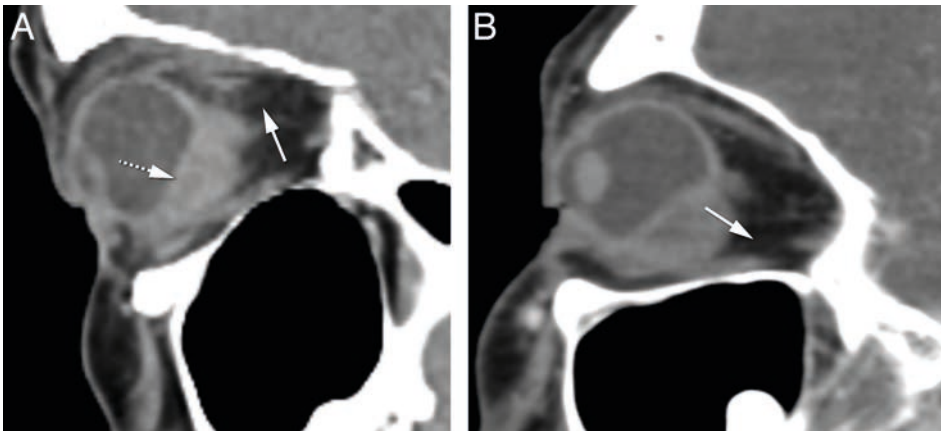


Figure 7.

A. 41 y/o female. Idiopathic inflammatory nodular scleritis on the left. Sagittal CECT: posterior wall globe focal mass. Deviation of the choroid-retinal layer internally (dashed arrow) suggesting a scleral origin. Painful periscleral cellulitis (arrow) favoring the diagnosis of scleritis.

B. 57 y/o female. Periocular breast cancer metastasis. Sagittal CECT: posterior wall globe focal mass, similar to (A), but note the normal aspect of the fat (arrow). Clinically there was no pain, both favoring the diagnosis of a tumor.

widely used, to targeted immunotherapy. Treatment is becoming more and more etiology specific and therefore recognizing the underlying disease in orbital inflammation has strong clinical implications. In Table 2 the main features of orbital inflammation due to different inflammatory diseases are summarized.

Idiopathic Orbital Inflammation (IOI), often called pseudotumor, is a diagnosis of exclusion and therefore infection, malignancy and a systemic inflammatory process must be ruled out [2]. Although the cause of IOI is unknown, an immune-mediated pathophysiological mechanism is likely [18]. It is the third most common orbital disease after *Graves'* orbitopathy and lymphoproliferative disorders [2,18]. Generally acute IOI presents with pain and is unilateral for the most of the times (75%) [2,18]. Imaging shows an infiltrative mass, less often

Table 2. Main imaging characteristics of the most common orbital inflammatory diseases.

Orbital Inflammatory Disease	Main Imaging Characteristics
IOI (Figure 8 A-D)	Pain, can involve all orbital structures, myositis with tubular configuration, cellulitis
Sarcoidosis (Figure 8 E)	Similar to IOI but: pain unusual, uveitis most common manifestation, predilection for antero-inferior quadrant
Graves' D (Figure 9 A-B)	Bilateral, myositis with predilection for inferior and medial quadrant and with fusiform configuration, increased orbital fat, no cellulitis
IgG4 RD (Figure 9 C-E)	Bilateral, chronic course, predilection for lateral and superior quadrant with myositis and dacryoadenitis, myositis with fusiform configuration, cellulitis, infraorbital nerve involvement
Granulomatosis w/poliansiitis (Figure 10)	Predilection for extraconal and conal compartments, chronic sinonasal involvement with bone destruction
ISOI (Figure 11)	Chronic course, predilection for lateral and superior quadrant with myositis and dacryoadenitis, enophthalmus possible

IOI – Idiopathic Orbital Inflammation. Graves' D – Graves' disease. IgG4 RD - Immunoglobulin G4-related disease. ISOI – Idiopathic Sclerosing Orbital Inflammation.

a focal mass, most of the time hypointense on T2-WI, with contrast enhancement [18] and lacks diffusion restriction [8]. IOI can involve any orbital compartment, commonly involving multiple sites at the same time [18]. The preseptal space is however less involved comparing to lymphoma [10]. In its muscular form IOI affects especially the medial followed by the superior and lateral recti [18,24], involving both the belly and the tendon, giving the muscle a tubular appearance. Most of the time the surrounding fat is involved (Figure 8 A-D) [2,18]. Fibrosis is frequently present at pathological examination [18]. Treatment for IOI consists of intravenous steroids [2]. Radiotherapy and chemotherapeutic agents such as methotrexate are alternative treatments [18]. *Tolosa-Hunt* syndrome is a rare subtype of pseudotumor with involvement confined to the orbital apex and/or cavernous sinus resulting in acute orbital pain and paralysis of cranial nerves III, IV, V (superior division) and VI [2]. The orbital pain should resolve within 72 hours when treated adequately with steroids, ophthalmoparesis usually requiring a little longer depending on inflammation degree and steroids regimen. Sarcoidosis is a systemic inflammatory disease of unknown etiology, characterized by the presence of granulomas in the affected organs [26]. Lungs and skin are most common affected. Sinonasal involvement is rare [27]. Orbital involvement is seen in 25-60% of patients with systemic sarcoidosis [28]. Sarcoidosis can involve any orbital compartment [28], similar to IOI. However, in sarcoidosis uveitis is the most common manifestation, the antero-inferior orbital quadrant is involved to a greater degree, the cavernous sinus can be affected as well and isolated myositis is rare (Figure 8 E) [26]. The involved orbital structures are hypointense on T2, enhance and no DWI restriction is expected. Clinical presentation is subacute evolving from months to years. Pain is not a typical feature. Orbital involvement is unilateral in 75% of

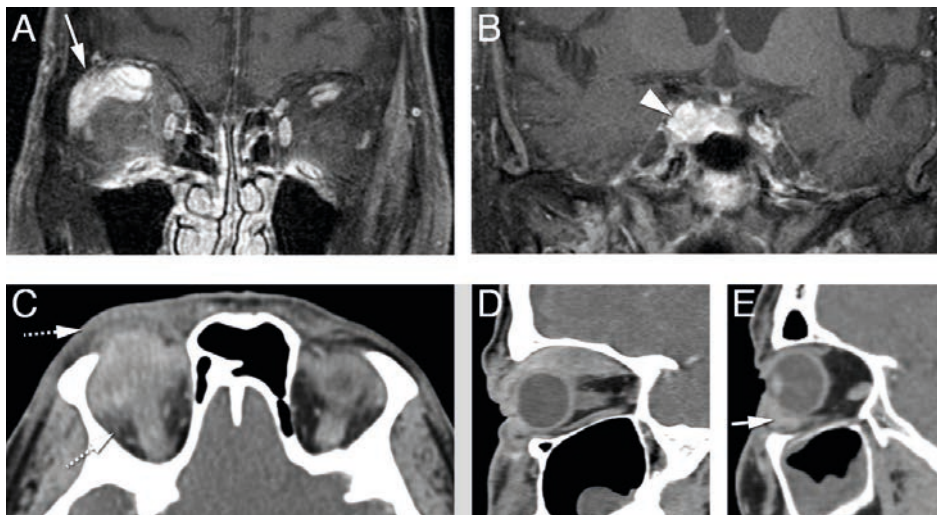


Figure 8.

A, B. 89 y/o male with idiopathic orbital inflammation. Enhanced coronals T1-WI with fat signal suppression (A, B): unilateral multifocal disease on the right involving the complex levator palpebrae-superior rectus and lacrimal gland (arrow) and the cavernous sinus (arrowhead). The bright signal around the inferior recti is due to inhomogeneous fat-saturation.

C, D. 46 y/o man with idiopathic orbital inflammation. Axial (C) and sagittal (D) CECT: myositis of the right superior muscle complex with surrounding cellulitis (dashed arrows). Muscle involvement encompasses tendon and muscle belly giving the muscle a tubular configuration (D).

E. 43 y/o male with sarcoidosis. Sagittal CECT: typical involvement of the antero-inferior quadrant of the left orbit with mass in the inferior eyelid (arrow).

cases. Isolated orbital granulomatous involvement, in the absence of systemic disease, should not be called orbital sarcoidosis, as it may represent an idiopathic granulomatous orbital inflammation, probably a different entity, affecting especially men in the fourth decade and in 50% of cases affecting the lacrimal gland [26,29]. Serum angiotensin-converting enzyme (ACE) is increased in 60 to 90% of patients with active disease and reflects its severity [1,30]. Oral steroids are the mainstay of treatment. Cytotoxic agents (v.g. methotrexate) are used as second line. Surgical excision may be considered for localized orbital disease, namely eyelid [26].

Thyroid-Associated Orbitopathy (TAO) is an autoimmune condition of the orbit, more often associated with *Graves'* hyperthyroidism, but it may exist in patients with euthyroid or hypothyroid chronic autoimmune thyroiditis [31]. The most important pathogenic factors are the Thyroid-Stimulating Hormone (TSH) receptor auto-antibodies, sharing as targets TSH receptors localized on orbital fibroblasts and adipocytes [31]. On TAO the extraocular muscles are the most common orbital structure involved [4]. Muscle involvement is bilateral on 90% and symmetrical on 70% of cases. The inferior rectus muscle is usually the first to be involved, followed by the medial, superior and the lateral recti and the oblique muscles. The tendon tends to be spared giving the muscle a fusiform configuration [4]. No surrounding cellulitis is seen. Increased orbital fat and dacryoadenitis may coexist. The enlarged muscles

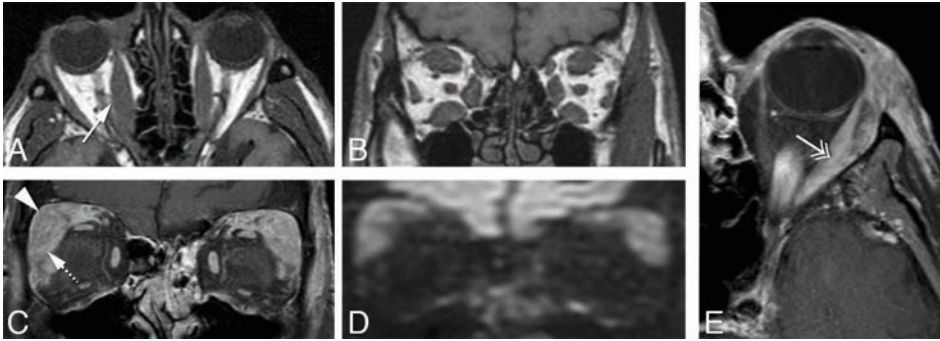


Figure 9.

A, B. 40 y/o female with thyroid-associated orbitopathy. Axial (A) and coronal T1-WI (B): bilateral and symmetric enlargement of the inferior, medial and complex levator palpebrae-superior rectus muscles. Notice fusiform configuration of the muscles because sparing of the tendon (arrow) and no surrounding infiltration of the fat. C-E. 35 y/old male with IgG4 related disease. Coronals enhanced T1-WI with fat signal suppression (C) and DWI (D) and axial enhanced T1-WI with fat signal suppression (E): bilateral involvement of the superolateral quadrants of the orbits, including bilateral enlargement of the lacrimal glands with involvement of some of the adjacent muscles. Involvement of both the orbital (arrowhead) and palpebral (dashed arrow) lobes of the lacrimal gland. Fusiform configuration (double headed arrow) of the muscle. No diffusion restriction favoring an inflammatory process.

and increased fat will induce proptosis. There can be crowding of the apex with compression of the optic nerve [4]. Indirect but objective signs of crowding of the apex and optic nerve compression are the presence of an enlarged superior ophthalmic vein and intracranial fat prolapse [4]. Proptosis may induce stretching of the optic nerve (Figure 9 A-B). Serologic testing includes measuring serum TSH, T3, T4, TSH-r antibody, thyrotropin-binding inhibitory immunoglobulin and thyroid stimulating immunoglobulin [32]. Natural history of the disease depicts an active phase followed by an inactive phase. MRI is a valuable tool to distinguish both stages, by demonstrating edema within the extraocular muscles in the active stage, translated as hypersignal on the STIR sequence [4,31,33]. Immunomodulatory therapies are the treatment of choice but are only effective in the active phase of the disease and therefore should not be considered in patients with inactive TAO [4].

Immunoglobulin G4-related Disease (IgG4 RD) is a recently described systemic inflammatory process of unknown etiology [24]. Any organ can be involved but there is a predilection for the orbits, salivary glands, lymph nodes, pancreas and hepatobiliary system. *Mickulicz* disease, previously thought to be a subtype of *Sjogren's* syndrome, is now considered part of the IgG4 RD [34,35]. IgG4 RD of the orbit has an indolent chronic course with symptoms evolving on average for 45 months at time of diagnosis [26]. Pain is not a characteristic finding [24,36]. On IgG4 RD of the orbit the extraocular muscles are the most common orbital structure involved (89%). Myositis is mostly bilateral (88%). The lateral rectus is the most affected muscle (76%) and typically enlarged to the greatest degree. The tendon is spared in 96% of cases, giving the muscle a fusiform configuration [24]. The lacrimal gland is the second most commonly orbital structure involved (70%) and its involvement is more common bilateral (58%) (Figure 9 C-E) [24,34]. Cellulitis is present in 44%, either pre or postseptal, uni or bilateral [24].

Perineural involvement has been reported, mostly affecting branches of the trigeminal nerve, the infraorbital nerve being involved in 30% and mostly unilateral [24,35,37,38,39]. There is expansion of the *foramina* [39]. In 89% of patients with IgG4 RD there is sinus disease as well [24]. At imaging orbital IgG4 RD lesions are diffuse or tumefactive, homogeneous, hypointense on T2-WI, enhancing, with no DWI restriction [37,40]. Bone remodeling is possible [37]. Increased IgG4 levels in serum will help in making the diagnosis [40], but serum IgG4 can be normal in up to 40% of patients with biopsy proven disease [32,38]. The definitive diagnosis is histopathologic typically with abundant IgG4-positive plasma cells and fibrosis [38,41]. Lymphoma can be a complication of IgG4 related disease [35,36,38]. Although the most effective therapy of IgG4-RD has yet to be defined, rituximab is a promising alternative to glucocorticoids [3,42,43].

Granulomatosis with polyangiitis, previously known as *Wegener* granulomatosis, is presumed to be an autoimmune disease but its exact nature remains unknown [44]. The organs most commonly involved are the lungs (95%), the paranasal sinuses (90%) and the kidneys (85%) [6]. Orbital involvement usually presents several years after the onset of the disease [45] and is mostly unilateral (86%) [6,45]. Pain is occasionally present [1,44]. There are two types of orbital involvement, granulomatous disease, causing an inflammatory mass, and small vessel vasculitis, causing among others scleritis, uveitis and optic neuritis [7]. In 70% of the cases the granulomatous orbital form represents an extension from sinus disease [7]. Extraconal involvement is present in 88% of the cases, frequently with conal extension [7]. Intraconal involvement without extraconal involvement is rare being present only in 6% of the cases [7]. Lesions enhance, are hypointense on T2-WI [7] and no DWI restriction is expected. Nasosinusal involvement is characterized by mucosal thickening, bone destruction and nasal septal perforation (Figure 10). The differential diagnosis based on image would include invasive fungal sinusitis, which has a different clinical context, the latter occurring in the setting of an immunosuppressed patient. The definitive diagnosis is based on tissue biopsy (granulomas, necrosis and vasculitis) [7,44]. A positive antineutrophil cytoplasmic antibodies (ANCA) is a marker of disease activity. It is present in more than 90% of patients with active systemic disease but only in 32% of patients with a limited form of the disease [1,7,30]. Therapy is based in immunosuppressive agents such as cyclophosphamide and corticosteroids [7]. Idiopathic sclerosing orbital inflammation (ISOI) is a rare disease [45,46]. Previously thought to be the endstage of IOI it is now considered a distinct pathologic entity with marked fibrosis present early in the disease [45-47]. ISOI is a chronic, indolent process with symptoms evolving on average for 18 to 24 months at time of diagnosis. Pain may be present. On imaging ISOI manifests as an ill defined mass, slightly enhancing, hypointense on T2-WI and with no DWI restriction. There is a predilection for the lateral and superior quadrants and therefore the lacrimal gland and the superior and lateral recti muscles are prone to be involved [45,47]. Enophthalmus can exist due to the fibrotic process (Figure 11) and extraorbital involvement is a possibility, with disease extending to the pterygopalatine fossa, to the masticator and buccal

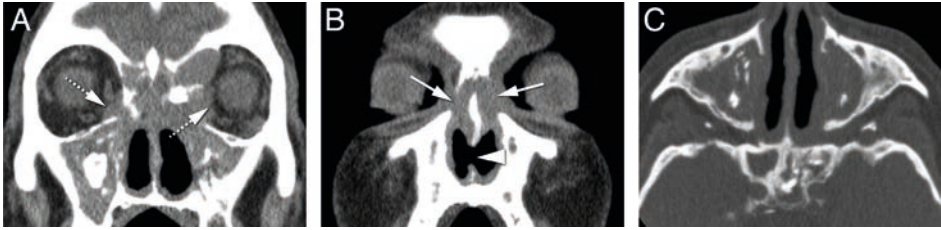


Figure 10.

67 y/o male with granulomatosis with polyangiitis involving the orbit, nose and sinuses. Coronals (A, B) and axial (C) CT: chronic pansinusitis with sclerosis of the bony walls and intrasinus calcifications coexisting with nasal septum (arrowhead) and lamina papiracea (arrows) erosions. Bilateral orbital involvement in the extraconal compartment (dashed arrows).

space and to the intracranial compartment [45]. The diagnosis of ISOI depends largely on biopsy, showing marked fibrosis together with a mixed chronic inflammatory cell infiltrate [45]. First-line treatment, although still controversial, encompasses corticosteroids and azathioprine, with poor results as fibrosis increases and inflammation subsides [45]. Some patients may show an elevated seric and tissue IgG4 [46]. It is difficult to know whether IgG4-related orbital disease is a distinct entity or an additional defining characteristic of idiopathic sclerosing orbital inflammation [46]. Testing IgG4 is important as rituximab seems effective in IgG4-related disease. Differential diagnosis includes sclerosing lymphoma and sclerosing breast carcinoma metastasis [48] but these entities, unlike ISOI, will show restricted diffusion on MRI.

Erdheim-Chester disease is a rare non-*Langerhans* cell histiocytosis of unknown origin, with multiorgan infiltration by lipid-laden histiocytes, belonging to the group of xantogranulomatous diseases [49,50]. The skeleton is the most commonly involved organ (96%), along with brain, heart, lung, liver, kidney, skin and retroperitoneal space [1]. Orbital involvement is also common. On imaging *Erdheim-Chester* disease presents with infiltrative intraconal masses, hypointense on T2-WI, enhancing after gadolinium and DWI restriction is not expected (Figure 12) [49]. Xanthomatous lesions of the eyelids are also present. Histologic evaluation reveals foamy cell infiltration, *Touton* giant cells and fibrosis. Immunologic staining confirms the diagnosis as these cells are positive for CD68, a histiocytic marker [1].

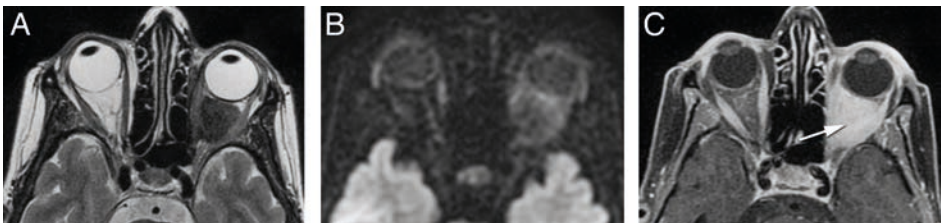


Figure 11.

48 y/o female with idiopathic sclerosing orbital inflammation. Axial T2 WI (A), axial DWI (B) and enhanced axial T1 WI with fat signal suppression (C): large intraconal mass on the left (arrow), with no restriction diffusion, hypointense on T2, with marked enhancement after contrast. Notice enophthalmus, very unusual for a retrobulbar mass, together with absence of restriction diffusion, making it suspicious for sclerosing orbital inflammation.

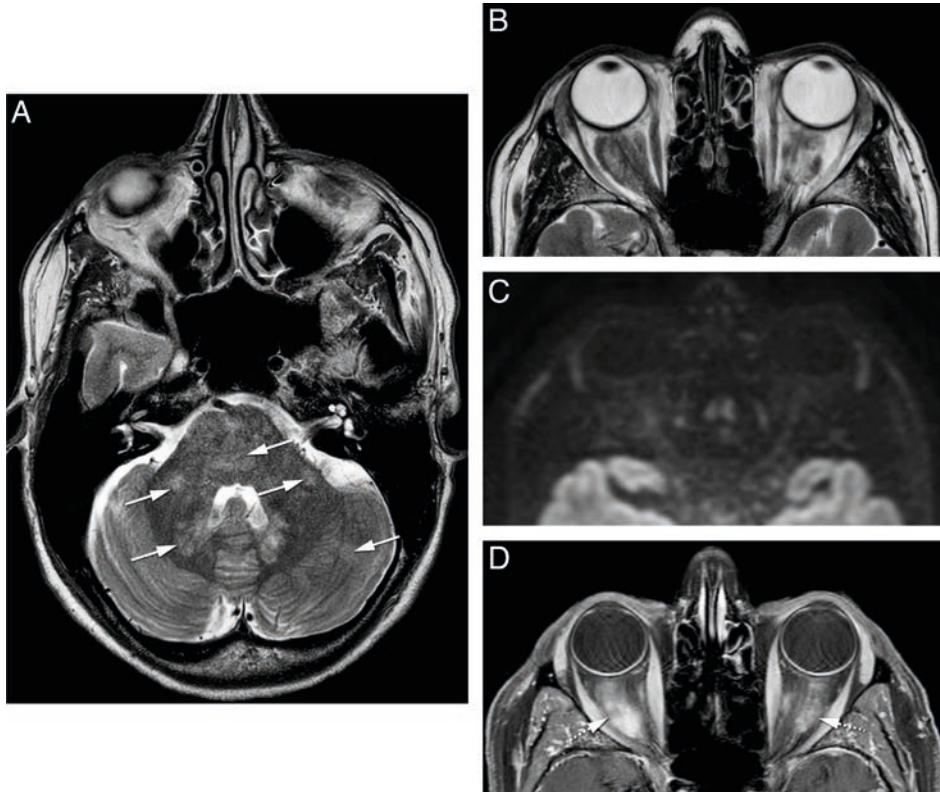


Figure 12.

47 y/o female with *Erdheim-Chester* disease. Axial T2 WI (A, B), axial DWI (C) and enhanced axial T1 WI with fat signal suppression (D): bilateral intraconal masses surrounding the optic nerves (dashed arrows), slightly heterogeneous on T2, no restriction diffusion, enhancing after contrast. Bilateral involvement of cerebellum, middle cerebellar peduncles and pons (arrows).

Decision Tree in Orbital Inflammation

Orbital inflammation presents on radiological imaging as a solid enhancing lesion, mostly as an ill-defined or infiltrative lesion. The differential diagnosis of an orbital solid enhancing lesion is however vast including not only inflammation but also infection, benign and malignant tumors and vascular malformations (*e.g.* cavernous hemangioma). In the presence of an orbital enhancing solid mass, one should first recognize its inflammatory nature and second try to determine the underlying inflammatory disease.

With those two purposes in mind and with background knowledge of the imaging characteristics of orbital inflammation we designed a decision tree for an orbital solid enhancing lesion (Figure 13).

Population is first dichotomized according to the DWI and subsequently whether pain and cellulitis are present. Diffusion restriction with no pain and no cellulitis point to malignant tumor, and biopsy should be envisaged. Facilitated diffusion together with no pain and no cellulitis can still correspond to inflammation, but other diagnosis such as a benign tumor

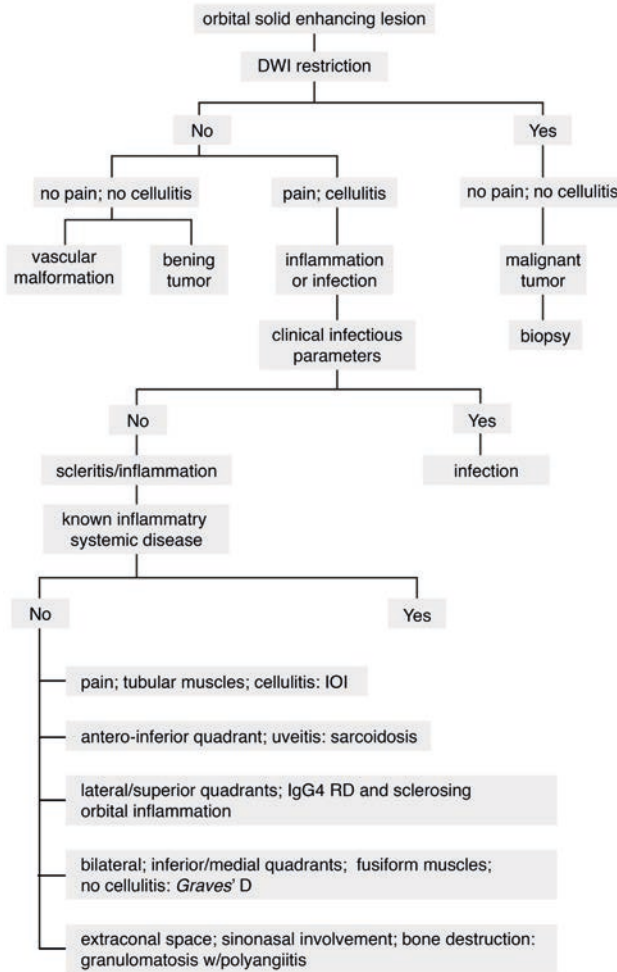


Figure 13. Decision Tree in an orbital solid enhancing lesion. IOI - Idiopathic Orbital Inflammation. IgG4 RD - Immunoglobulin G4-related disease.

or a vascular malformation should be kept in mind. The absence of diffusion restriction, in the presence of pain and/or cellulitis, favors an inflammatory or infectious process. The differentiation between inflammation and infection is mainly based on clinical features, with long standing symptoms pointing to inflammation, while the presence of fever, high infectious parameters (v.g. leukocytosis, elevated CRP) and pus, in which case DWI restriction should be expected, suggesting infection. On imaging the presence of sinusitis and/or an abscess points to infection, while scleritis suggests inflammation.

Imaging may also play an important role on establishing the diagnosis of the underlying inflammatory disease. This is especially important if the patient is not known to harbor any inflammatory systemic disease. In cases the inflammatory process shows predilection for the muscles at the inferior/medial quadrants of the orbits, the involved muscles have a fusiform

configuration and no cellulitis is present *Graves'* disease should be considered. *Graves'* disease is mostly bilateral and symmetric and there can be increased intraorbital fat. In cases of IgG4 related disease or sclerosing orbital inflammation the lateral/superior quadrants of the orbit are preferentially involved and both have an indolent course. IgG4 related disease is mostly bilateral, the involved muscles have a fusiform configuration and in 30% of the cases there is enlargement of the infraorbital nerve, which when present is very suggestive of the diagnosis. On sclerosing orbital inflammation enophthalmus can exist suggesting the fibrotic process. If there is a predilection for the extraconal space, with or without chronic sinonasal involvement, with bone destruction, consider granulomatosis with polyangiitis. History of uveitis and a predilection for the antero/inferior quadrant suggests sarcoidosis. Sarcoidosis is mostly unilateral and with a subacute presentation. When pain is a predominant feature, the involved muscles have a tubular configuration and cellulitis is present consider idiopathic orbital inflammation. Idiopathic orbital inflammation is mostly unilateral and when involving the muscles it affects especially the medial followed by the superior and lateral recti.

The definitive diagnosis of the orbital inflammatory disease is made by combining the radiological pattern with the laboratory findings and characteristics of other organ involvement. The radiological pattern can be specific for a certain type of orbital inflammation such as in *Graves'* disease or in granulomatosis with polyangiitis. However sometimes these patterns are shared between different etiologies making the imaging pattern not specific. Still the evaluation of the radiological pattern will shorten the differential diagnosis. That is helpful as it can guide the laboratory evaluation and eventual imaging of other organs. When the diagnosis is still unclear tissue characterization and/or a therapeutical test is needed. An orbital biopsy is easily considered for accessible orbital lesions such as dacryoadenitis. Locations where surgery is difficult or dangerous, such as the orbital apex or around the optic nerve, may confer a higher threshold for biopsy [51,52].

CONCLUSION

Orbital inflammation is frequently mistaken either for orbital infection or malignant tumors, and its underlying cause is often overlooked. Imaging findings obtained through appropriate protocols and knowledge of the most common orbital inflammatory diseases will help shorten the differential diagnosis, with important therapeutic and prognostic consequences. We have therefore combined different imaging and clinical clues that will allow one to recognize an orbital solid enhancing lesion as inflammatory. Subsequently we have shown how the different radiological patterns will help in differentiate the possible orbital inflammatory diseases. Overall these considerations enable the treating physician to establish an adequate treatment and at times a biopsy can be avoided.

REFERENCES

1. Gordon LK. Orbital Inflammatory Disease: a diagnostic and therapeutic challenge. *Eye (Lond)*. 2006 Oct;20(10):1196-1206.
2. Pakdaman MN, Sepahdari AR, Elkhamary SM. Orbital inflammatory disease: Pictorial review and differential diagnosis. *World J Radiol*. 2014 Apr 28;6(4):106-115.
3. Wallace ZS, Khosroshahi A, Jakobiec FA, Deshpande V, Hatton MP, Ritter J, Ferry JA, Stone JH. IgG4-related systemic disease as a cause of "idiopathic" orbital inflammation, including orbital myositis, and trigeminal nerve involvement. *Surv Ophthalmol*. 2012 Jan-Feb;57(1):26-33.
4. Kahaly GJ. Imaging in thyroid-associated orbitopathy. *Eur J Endocrinol*. 2001 Aug;145(2):107-118.
5. Edrich CL. Posterior scleritis mimicking orbital cellulitis. *Eye (Lond)*. 2005 Nov;19(11):1229-32.
6. Radhakrishnan R, Cornelius R, Cunnane MB, Golnik K, Morales H. MR imaging findings of endophthalmitis. *Neuroradiol J*. 2016 Apr;29(2):122-129.
7. Provenzale JM, Mukherji S, Allen NB, Castillo M, Weber AW. Orbital Involvement by Wegener's Granulomatosis: Imaging Findings. *Am J Roentgenol* 1996 Apr;166(4):929-934.
8. Sepahdari AR, Politi LS, Aakalu VK, Kim HJ, Razek AAKA. Diffusion-weighted imaging of orbital masses: multi-institutional data support a 2-ADC threshold model to categorize lesions as benign, malignant, or indeterminate. *Am J Neuroradiol*. 2014 Jan;35(1):170-175.
9. de Graaf P, Pouwels PJW, Rodjan F, Moll AC, Imhof SM, Knol DL, Sanchez E, van der Valk P, Castelijns JA. Single-shot turbo spin-echo diffusion-weighted imaging for retinoblastoma: initial experience. *Am J Neuroradiol*. 2012 Jan;33(1):110-118.
10. Ren J, Yuan Y, Wu Y, Tao X. Differentiation of orbital lymphoma and idiopathic orbital inflammatory pseudotumor: combined diagnostic value of conventional MRI and histogram analysis of ADC maps. *BMC Med Imaging*. 2018 May 2;18(1):6.
11. Yuan Y, Kuai X-P, Chen X-S, Tao X-F. Assessment of dynamic contrast-enhanced magnetic resonance imaging in differentiation of malignant from benign orbital masses. *Eur J Radiol*. 2013 Sep;82(9):1506-1511.
12. Diogo MC, Jager MJ, Ferreira TA. CT and MR imaging in the diagnosis of scleritis. *Am J Neuroradiol*. 2016 Dec;37(12):2334-2239.
13. Nguyen V, Singh A, Altmeyer W, Tantiwongkosi B. Demystifying Orbital Emergencies: A Pictorial Review. *Radiographics*. 2017 May-Jun;37(3):947-962.
14. McCluskey PJ, Watson PG, Lightman S, Haybittle J, Restori M, Branley M. Posterior scleritis: clinical features, systemic associations, and outcome in a large series of patients. *Ophthalmology*. 1999 Dec;106(12):2380-2386.
15. Li CQ, Cho AA, Edward NJ, Edward DP, Fajardo RG, Mafee MF. Magnetic resonance imaging of uveitis. *Neuroradiology*. 2015 Aug;57(8):825-832.
16. Benson WE. Posterior scleritis. *Surv Ophthalmol*. 1988 Mar-Apr;32(5):297-316.
17. Osman Saatci A, Saatci I, Kocak N, Durak I. Magnetic resonance imaging characteristics of posterior scleritis mimicking choroidal mass. *Eur J Radiol*. 2001 Aug;39(2):88-91.
18. Ding ZX, Lip G, Chong V. Idiopathic orbital pseudotumour. *Clin Radiol*. 2011 Sep;66(9):886-892.
19. Derr C, Shah A. Bilateral dacryoadenitis. *J Emerg Trauma Shock*. 2012 Jan;5(1):92-94.

20. Sadiq SB, Corbett JJ, Abubakr A. Idiopathic optic perineuritis: disguised as recurrent optic neuritis. *Clin Neurol Neurosurg.* 2015 May;132:12-15.
21. Cheng ACO, Chan NCY, Chan CKM. Acute and subacute inflammation of the optic nerve and its sheath: clinical features in Chinese patients. *Hong Kong Med J.* 2012 Apr;18:115-122.
22. He M, Cestari D, Cunnane MB, Rizzo JF. The use of diffusion MRI in ischemic optic neuropathy and optic neuritis. *Semin Ophthalmol.* 2010 Sep-Nov;25(5-6):225-232.
23. Rizzo JF, Andreoli CM, Rabinov JD. Use of Magnetic Resonance Imaging to Differentiate Optic Neuritis and Nonarteritic Anterior Ischemic Optic Neuropathy. *Ophthalmology.* 2002 Sep;109(9):1679-1684.
24. Tiegs-Heiden CA, Eckel LJ, Hunt CH, Diehn FE, Schwartz KM, Kallmes DF, Salomao DR, Witzig TE, Garrity JA. Immunoglobulin G4-Related Disease of the Orbit: Imaging Features in 27 Patients. *Am J Neuroradiol* 2014 Jul;35(7):1393-1397.
25. McNab AA. The 2017 Doyne Lecture: the orbit as a window to systemic disease. *Eye (Lond).* 2018 Feb;32(2):248-261.
26. Prabhakaran VC, Saeed P, Esmaeli B, Sullivan TJ, McNab A, Davis G, Valenzuela A, Leibovitch I, Kesler A, Sivak-Callcott J, Hoyama E, Selva D. Orbital and Adnexal Sarcoidosis. *Arch Ophthalmol.* 2007 Dec;125(12):1657-1662.
27. Kirsten AM, Watz H, Kirsten D. Sarcoidosis with involvement of the paranasal sinuses - a retrospective analysis of 12 biopsy-proven cases. *BMC Pulm Med.* 2013 Sep 26;13:59.
28. Carmody RF, Mafee MF, Goodwin JA, Small K, Haery C. Orbit and optic pathway sarcoidosis: MR findings. *Am J Neuroradiol.* 1994 Apr;15:775-783.
29. Mombaerts I, Schlingemann RO, Goldschmeding R, Koorneef L. Idiopathic granulomatous orbital inflammation. *Ophthalmol.* 1996 Dec;103(12):2135-2141.
30. Srinivasan A, Kleinberg T, Murchison A, Bilyk JR. Laboratory Investigations for diagnosis of Autoimmune and Inflammatory Periocular Disease: Part II. *Ophthal Plast Reconstr Surg.* 2017 Jan-Feb;33(1):1-8.
31. Tortora F, Cirillo M, Ferrara M, Belfiore MP, Carella C, Caranci F, Cirillo S. Disease activity in Graves' ophthalmopathy: diagnosis with orbital MR imaging and correlation with clinical score. *Neuroradiol J.* 2013 Oct;26(5):555-564.
32. Srinivasan A, Kleinberg T, Murchison, Bilyk JR. Laboratory Investigations for diagnosis of Autoimmune and Inflammatory Periocular Disease: Part I. *Ophthal Plast Reconstr Surg.* 2016 Sep-Oct;32(5):321-328.
33. Kirsch E, Hammer B, von Arx G. Graves'orbitopathy: current imaging procedures. *Swiss Med Wkly.* 2009 Oct 31;139(43-44):618-623.
34. Cheuk W, Yuen HK, Chan JK. Chronic sclerosing dacryoadenitis: part of the spectrum of IgG4-related sclerosing disease? *Am J Surg Pathol.* 2007 Apr;31(4):643-645.
35. Toyoda K, Oba H, Kutomi K, Furui S, Oohara A, Mori H, Sakurai K, Tsuchiya K, Kan S, Numaguchi Y. MR imaging of IgG4-related disease in the head and neck and brain. *Am J Neuroradiol.* 2012 Dec; 33(11):2136-2139.
36. Plaza JA, Garrity JA, Dogan A, Ananthamurthy A, Witzig TE, Salomao DR. Orbital inflammation with IgG4-positive plasma cells: manifestation of IgG4 systemic disease. *Arch Ophthalmol.* 2011 Apr;129(4):421-428.
37. Song YS, Choung H-K, Park S-W, Kim J-H, Khwarg SI, Jeon YK. Ocular adnexal IgG4-related disease: CT and MR findings. *Br J Ophthalmol.* 2013 Apr;97(4):412-418.

38. Ginat DT, Freitag SK, Kieff D, Grove A, Fay A, Cunnane M, Moonis G. Radiographic patterns of orbital involvement in IgG4-related disease. *Ophthal Plast Reconstr Surg*. 2013 Jul-Aug;29:261-266.
39. Katsura M, Morita A, Horiuchi H, Ohtomo K, Machida T. IgG4-related inflammatory pseudotumor of the trigeminal nerve: another component of IgG4-related sclerosing disease? *Am J Neuroradiol*. 2011 Sep;32(8): E150-152.
40. Fujita A, Sakai O, Chapman MN, Sugimoto H. IgG4-related disease of the head and neck: CT and MR imaging manifestations. *Radiographics*. 2012 Nov-Dec;32(7):1445-1458.
41. Deshpande V, Zen Y, Chan JK, Yi EE, Sato Y, Yoshino T, Kloppel G, Heathcote JG, Khosroshahi A, Ferry JA, Aalberse RC, Bloch DB, Brugge WR, Bateman AC, Carruthers MN, Chari ST, Cheuk W, Cornell LD, Fernandez-Del Castillo C, Forcione DG, Hamilos DL, Kamisawa T, Kasashima S, Kawas, Kawano M, Lauwers GY, Masaki Y, Nakanuma Y, Notohara K, Okazaki K, Ryu JK, Saeki T, Sahani DV, Smyrk TC, Stone JR, Takahira M, Webster GJ, Yamamoto M, Zamboni G, Umehara H, Stone JH. Consensus statement on the pathology of IgG4-related disease. *Mod Pathol*. 2012 Sep;25(9):1181-1192.
42. Khosroshahi A, Carruthers MN, Deshpande V, Unizony S, Bloch DB, Stone JH. Rituximab for the treatment of IgG4-related disease: lessons from 10 consecutive patients. *Medicine (Baltimore)*. 2012 Jan;91(1):57-66.
43. Wu A, Andrew NH, Tsirbas A, Tan P, Gajdatsy A, Selva D. Rituximab for the treatment of IgG4-related orbital disease: experience from five cases. *Eye (Lond)*. 2015 Jan;29(1):122-128.
44. Aletaha M, Tavakoli M, Kanavi MR, Hashemlou A, Roghaei S. Bilateral Orbital Mass Lesions: a Presentation of Wegener's Granulomatosis. *J Ophthalmic Vis Res*. 2011 Jul;6(3):215-218.
45. Hsuan JD, Selva D, McNab AA, Sullivan TJ, Saeed P, O'Donnell BA. Idiopathic Sclerosing Orbital Inflammation. *Arch Ophthalmol*. 2006 Sep;124(9):1244-1250.
46. Pemberton JD, Fay A. Idiopathic sclerosing orbital inflammation: a review of demographics, clinical presentation, imaging, pathology, treatment, and outcome. *Ophthal Plast Reconstr Surg*. 2012 Jan-Feb;28(1):79-83.
47. Rootman J, McCarthy M, White V. Idiopathic sclerosing inflammation of the orbit. A distinct clinicopathologic entity. *Ophthalmology*. 1994 Mar;101(3):570-584.
48. Lokdarshi G, Pushker N, Nagar A. Sclerosing lesions of the orbit: a review. *Middle East Afr J Ophthalmol*. 2015 Oct-Dec;22(4):447-451.
49. Mamlouk MD, Aboian MS, Glastonbory CM. Erdheim-Chester Disease. *Radiology*. 2017 Sep;284(3):910-917.
50. Abreu MR, Chung CB, Biswal S, Haghighi P, Hesselink J, Resnick D. Erdheim-Chester disease: MR imaging, anatomic and histopathologic correlation of orbital involvement. *Am J Neuroradiol*. 2004 Apr;25(4):627-630.
51. Yesiltas YS, Gündüz AK. Idiopathic Orbital Inflammation: Review of Literature and New Advances. *Middle East Afr J Ophthalmol*. 2018 Apr-Jun;25(2):71-80.
52. Mombaerts I, Bilyk JR, Rose GE, McNab AA, Fay A, Dolman PJ, Allen RC, Devoto MH, Harris GJ. Consensus on Diagnostic Criteria of Idiopathic Orbital Inflammation Using a Modified Delphi Approach. *JAMA Ophthalmol*. 2017 Jul 1;135(7):769-776.

4

Eyelid



4.1

MR and CT imaging of the normal eyelid and its application in eyelid tumors

Teresa A Ferreira, Carolina F Pinheiro, Paulo Saraiva, Myriam G Jaarsma-Coes, Sjoerd G van Duinen, Stijn W Genders, Marina Marinkovic, Jan-Willem M Beenakker

Cancers 2020; 12(3):658

ABSTRACT

T-staging of most eyelid malignancies includes the assessment of the integrity of the tarsal plate and orbital septum, which are not clinically accessible. Given the contribution of MRI in the characterization of orbital tumors and establishing their relations to nearby structures, we assessed its value in identifying different eyelid structures in 38 normal eyelids and evaluating tumor extension in three cases of eyelid tumors. As not all patients can receive an MRI, we evaluated those same structures on CT and compared both results. All eyelid structures were identified on MRI and CT, except for the conjunctiva on both techniques and for the tarsal muscles on CT. Histopathology confirmed the MRI findings of orbital septum invasion in one patient, and the MRI findings of intact tarsus and orbital septum in another patient. Histopathology could not confirm or exclude tarsal invasion seen on MRI on two patients. Although imaging the eyelid is challenging, the identification of most eyelid structures is possible with MRI and, to a lesser extent, with CT and can, therefore, have an important contribution to the T-staging of eyelid tumors, which may improve treatment planning and outcome.

INTRODUCTION

The eyelids correspond to the anterior limit of the orbits. They are muscular-membranous structures [1], forming part of the protective system of the eye. The eyelids have complex anatomy, with each eyelid being constituted of three externally visible regions, namely the external skin, the internal palpebral conjunctiva, and the eyelid margin, all well evaluated with a physical examination. Histologically, however, seven structures [1] are identified in both eyelids, of which the deep structures are not amenable to physical evaluation. The most anterior structure of each eyelid is the skin. Behind the skin, there is the first layer of loose connective tissue. The third layer is the orbicularis oculi muscle, composed of skeletal muscle fibers. The fourth layer, lying behind the orbicularis oculi muscle, is a second layer of loose connective tissue. The fifth layer of each eyelid is a fibro-elastic layer, centrally formed by the tarsal plate and peripherally formed by the orbital septum. The tarsal plate is a firm plate composed of dense connective tissue that helps to maintain the eyelid shape but also containing sebaceous glands called the meibomian glands. The superior tarsus is 8–12 mm in height and attaches to the superior tarsal muscle. The inferior tarsus is smaller, only 3–4 mm in height, and attaches to the inferior septum and inferior tarsal muscle. The orbital septum maintains the intraorbital fat in place and is involved in the ocular and palpebral movements [2]. The orbital septum of both superior and inferior eyelids attaches peripherally to the orbital rim bone, where it is continuous with the periosteum [3]. Centrally the orbital septum attaches to the junction of the inferior tarsal muscle to the tarsal plate in the lower eyelid and to the levator palpebrae aponeurosis in the upper eyelid [1]. Inferiorly to its attachment to the superior orbital septum, the levator palpebrae aponeurosis fuses with the anterior aspect of the superior tarsal plate [4]. Posteriorly, on the most cranial part of the levator palpebrae aponeurosis and at its junction with the levator palpebrae muscle [4], lies the “V” shaped superior transverse (Whitnall) ligament. The sixth layer of the eyelids consists of the tarsal muscles, composed of smooth muscle fibers, acting as eyelid retractors. The superior tarsal muscle, also known as the Müller’s muscle, inserts superiorly at the junction of the levator palpebrae aponeurosis and levator palpebrae muscle and attaches inferiorly to the superior margin of the superior tarsal plate [1]. The inferior tarsal muscle inserts superiorly at the junction of the inferior tarsal plate and inferior septum, and inferiorly attaches to the fascia surrounding the inferior rectus muscle [1]. The most posterior layer of the eyelid is the palpebral or tarsal conjunctiva. The conjunctiva will reflect on the eyeball as bulbar conjunctiva, which is not part of the eyelid (Figure 1).

Eyelid malignancies can arise from any of the eyelid structures, but most are of cutaneous origin [5]. The most common skin eyelid tumor is the basal cell carcinoma (BCC), followed by squamous cell carcinoma (SCC), sebaceous cell carcinoma, Merkel cell carcinoma, and malignant melanoma [5–7]. Eyelid malignancies require specific deliberations as the functional and esthetical impact of surgical treatment can be devastating [6].

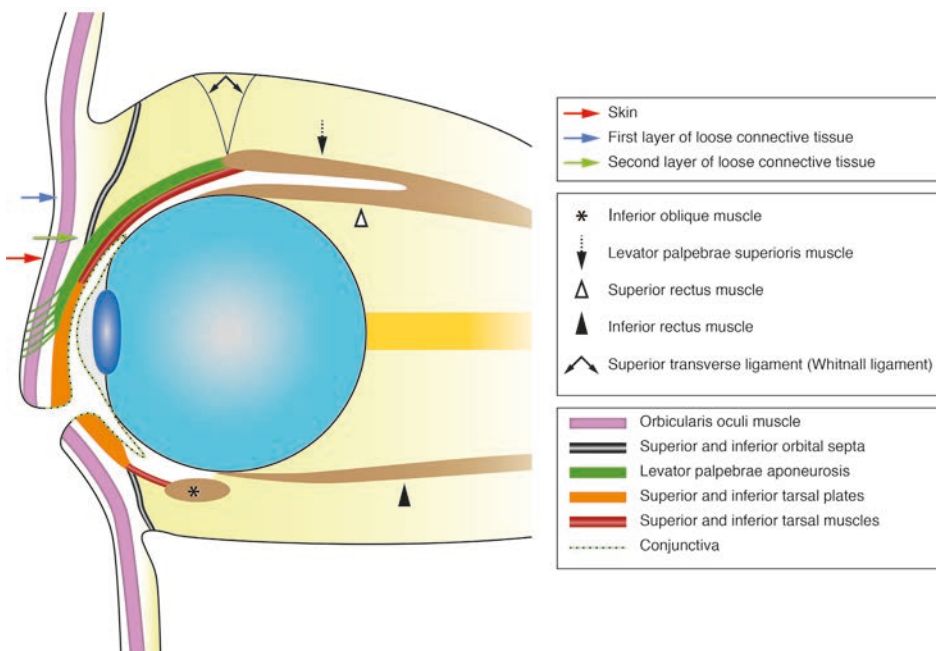


Fig. 1.
Schematic cross-section of the eyelids and anterior orbital anatomy.

Accurate staging of an eyelid tumor is based on the Tumor, Node and Metastasis (TNM) classification, and it is important, among others, to help the clinician in the planning of treatment [8,9]. The T-staging of eyelid tumors encompasses determination on whether there is an invasion of the eyelid structures such as the tarsal plate and orbital septum [8,9], which are not clinically accessible and, therefore, imaging can be crucial [10] for an accurate evaluation.

To our knowledge, eyelid anatomy has never been described on CT, and only a few descriptions are available on MRI [2,11–18]. Similarly, we are not aware of any radiological study depicting which anatomic eyelid structures are invaded by a tumor. The purpose of this manuscript is twofold: 1) To identify the normal anatomy of the eyelid both on MRI and CT, especially the tarsal plates and the orbital septa, 2) To apply this knowledge in tumor patients, comparing imaging data with pathology.

MATERIAL AND METHODS

Patient population

This single-center retrospective study was carried out according to the Code of Ethics of the World Medical Association (Declaration of Helsinki) for experiments involving humans and

in accordance with the recommendations of the local Ethics Committee (CME LUMC, Leiden University Medical Center, Project number P16.186). Three different groups of patients were evaluated in a total of 41 patients.

In Group 1, normal eyelid anatomy was assessed on MRI by evaluating MR-images of 19 patients with uveal melanoma (UM) (Table 1). Only the side with UM had been imaged. As the eyelids of these patients were not affected by the UM, they provided a representative view of the healthy anatomy. In 68% of the cases, the right eyelids were evaluated. Both the superior and inferior eyelids of the side available were assessed. Fourteen of the subjects were male (74%), and the median age of the group was 63 years (range 23 to 90).

In Group 2, normal eyelid anatomy was assessed on CT in 19 patients who received CT scans, including the orbits, with at least one healthy orbit (Table 2). Only the eyelids of one side were assessed, either the eyelids of the non-pathologic orbit or in the case of bilateral normal orbits, one was randomly chosen to be evaluated. In 63% of the cases, the right eyelids were

Table 1. Normal eyelid MRI anatomy Group (Group 1) patients' data regarding studied eyelid, slice plane evaluated and visualization score of the superior and inferior tarsal plates and of the superior and inferior orbital septa (1: not identified; 2: ill-defined; 3: well-defined; NP: not possible to evaluate - when the structures to be evaluated were not totally included in the planned slices).

Patient	Studied eyelid	Slice plane	Superior tarsus	Inferior tarsus	Superior septum	Inferior septum
1	OS	Axial	3	2	2	1
2	OD	Axial	2	3	NP	NP
3	OD	Sagittal	1	1	3	2
4	OD	Sagittal	3	3	3	3
5	OD	Sagittal	2	2	3	3
6	OD	Axial	3	3	3	NP
7	OD	Sagittal	3	3	3	2
8	OS	Sagittal	3	3	3	3
9	OD	Sagittal	2	3	3	3
10	OS	Sagittal	3	3	3	2
11	OS	Axial	3	NP	3	NP
12	OD	Axial	3	3	NP	NP
13	OD	Axial	3	3	NP	2
14	OD	Axial	NP	2	NP	NP
15	OD	Axial	3	3	3	NP
16	OS	Axial	3	3	NP	NP
17	OD	Sagittal	3	2	3	2
18	OS	Axial	3	2	NP	NP
19	OD	Sagittal	3	3	3	2

OS: oculus sinister; OD: oculus dexter

Table 2. Normal eyelid CT anatomy Group (Group 2) patients' data regarding studied eyelid and visualization score of the superior and inferior tarsal plates and of the superior and inferior orbital septa both on the sagittal and axial planes (1: not identified; 2: ill-defined; 3: well-defined; NP: not possible to evaluate - when the structures to be evaluated were not totally included in the planned slices).

Patient	Studied eyelid	Superior tarsus		Inferior tarsus		Superior septum		Inferior septum	
		Sag	Ax	Sag	Ax	Sag	Ax	Sag	Ax
1	OD	2	3	2	2	2	2	2	2
2	OD	3	3	2	2	2	3	1	1
3	OD	2	2	2	2	3	3	2	2
4	OS	2	3	2	3	2	3	2	3
5	OD	3	3	3	3	3	3	1	1
6	OS	1	2	1	1	2	2	1	1
7	OS	1	2	2	2	3	3	2	3
8	OD	3	2	1	1	2	2	1	2
9	OS	1	2	1	1	3	3	2	2
10	OD	2	3	2	2	1	1	1	1
11	OD	2	3	2	3	2	3	2	2
12	OS	2	2	2	3	2	2	2	2
13	OS	3	3	3	3	1	2	1	1
14	OD	1	2	1	2	2	2	1	2
15	OD	2	3	2	3	2	1	1	1
16	OD	2	3	2	3	2	2	1	2
17	OD	2	3	2	3	2	3	2	2
18	OD	2	2	3	3	3	3	2	2
19	OS	3	3	2	3	1	1	2	2

OS: oculus sinister; OD: oculus dexter; Sag: sagittal; Ax: axial.

evaluated. Both the superior and inferior eyelids of the side evaluated were assessed. Eleven of the subjects were female (58%). The median age was 45 years (range 19 to 79).

Group 3 consisted of three consecutive patients with different eyelid tumors, who were planned to be treated surgically. These patients received an MRI protocol that had been optimized for the evaluation of eyelid tumors. When available, the CT images were included in the evaluation (Table 3). Two of the subjects were female. The median age was 72 years (range 62 to 81). Patient 1 had a squamous cell carcinoma (SCC) of the palpebral and bulbar conjunctiva at the medial aspect of the left inferior eyelid involving the medial canthus. Clinically, there was evidence of orbital invasion due to abnormal eye movements. Patient 2 had a recurrent SCC of the skin at the medial aspect of the right inferior eyelid, involving the medial canthus and with minimal superior eyelid extension. Clinically, there was no evidence of orbital invasion. Patient 3 had residual melanotic melanoma (MM) at the palpebral conjunctiva of the left superior eyelid, discovered 4 weeks after surgical resection of a MM of medial bulbar conjunctiva of the left inferior eyelid. Clinically there was no evidence of orbital invasion.

Table 3. Group 3 patients' data regarding pathologic eyelid, clinical tumor localization, final pathology, presence of septum invasion and presence of tarsal invasion.

Patient	Pathologic Eyelid	Tumor Localization (Clinical)	Pathology	Septum Invasion (Imaging)	Tarsal Invasion (Imaging)
1	OS	Medial inferior eyelid palpebral and bulbar conjunctiva	SCC	Yes	Yes
2	OD	Medial inferior and superior eyelid skin	SCC	No	Suspected
3	OS	Superior eyelid palpebral conjunctiva	MM	No (tumor not seen)	No (tumor not seen)

OS: oculus sinister; OD: oculus dexter; SCC: squamous cell carcinoma; MM: melanotic melanoma.

MRI protocol

All MRIs were performed at a 3T MRI (wide bore Ingenia 3T, Philips Healthcare, Best, The Netherlands), using the setup we developed to scan the eyes of UM patients as described in reference [19]. A 4.7 cm surface receive coil (Philips Healthcare, Best, The Netherlands) was used, and the head was supported by a radiotherapy support (MaxSupport™, Medeo, Schöftland, Switzerland). All patients were asked to close their eyes and try to minimize their eye movements. The eyelids of the patients with eyelid tumors were covered with wet gauze to reduce the susceptibility artifacts due to the tissue-air interface.

In Group 1 patients, for the evaluation of the healthy eyelid anatomy, the 2D multi-slice (MS) sequences, with 2 mm thickness and an in-plane resolution of at least 0.5 x 0.5 mm² were used [19]. These included T1 (TE/TR:8/718 ms) and T2 (TE/TR:90/1331 ms) weighted-images (WI) and a contrast-enhanced T1-WI (8/764 ms) with spectral presaturation with inversion recovery (SPIR) fat signal suppression. For the analysis of the eyelid anatomy, both sagittal and axial sequences, perpendicular to the eyelid axis, need to be acquired. However, since these scans were primarily acquired to assess the UM, only one of the orientations was available. Based on the dedicated eye MRI protocol we use for UM patients [19], an optimized protocol for eyelid tumors was developed and used for the evaluation of Group 3 patients. Details of the dedicated eyelid MRI protocol were addressed in Table 4. In this protocol, a 3D T2-weighted scan was performed first and was used as an anatomical reference. Secondly, 2D multi-slice (MS) anatomical sequences were acquired in the sagittal and axial planes, both perpendicular to the main eyelid axis at the level of the tumor. These 2D MS scans consisted of T1-weighted and T2-weighted images, both with and without SPIR fat signal suppression and contrast-enhanced T1-weighted images with SPIR fat signal suppression. Finally, functional sequences were acquired, including diffusion-weighted imaging (DWI) and a dynamic contrast enhanced (DCE) scan with fat signal suppression. The DWI was performed in the sagittal and axial planes, both perpendicular to the main axis of the eyelid at the level of the tumor, while the DCE was acquired in the axial plane but not necessarily perpendicular to

Table 4. Scan parameters of the sequences of the dedicated eyelid protocol. Both the multi-slice (MS) and the diffusion-weighted imaging (DWI) sequences are planned perpendicular to the eyelid at the location of the tumor, while the Dynamic Contrast Enhanced (DCE) scan is acquired not necessarily perpendicular to the eyelid at the location of the tumor.

Scan Name	Voxel Size (mm ³)	FOV (mm ²)	Echo Train Length	TE(ms)/TR(ms)/Flip or Ref. Angle (Deg)	Fat Supr.	Avg.	Scan Time (m:ms)	Additional Parameters
3DTSE T2 SPIR	0.8x0.8x0.8	50x81x40	117	293/2500/35	SPIR	2	03:35	4 REST slabs to prevent foldover
MS TSE T1	0.5x0.5x2.0	100x100x24	6	8/400/180	-	1	0:43	50mm foldover suppression
MS TSE T2	0.4x0.4x2.0	100x100x24	17	90/1131/120	-	2	01:12	
MS TSE T1 SPIR	0.5x0.5x2.0	100x100x24	6	8/458/180	SPIR	1	0:50	50mm foldover suppression
MS TSE T2 SPIR	0.4x0.4x2.0	100x100x24	17	90/1249/120	SPIR	2	01:20	
DWI (TSE)	1.25x1.4x2.4	100x100x24	single shot	64/5759/50	SPIR	5	03:21	B=0, 800 s/mm ² 24mm foldover suppression
DCE	1.0x1.0x2.0	78x78x40	single shot	2.5/4.8/13	PROSET11	1	4:33	3s/dynamic using TWIST

TWIST: Time-resolved angiography With Interleaved Stochastic Trajectories [20]

the main axis of the eyelid at the level of the tumor. The susceptibility artifacts at the outer eyelid interface were not completely removed by the wet gauze. Therefore, localized volumetric shimming was applied for the patients of Group 3.

CT protocol

All CT scans in all Group 2 patients and in patient #1 from Group 3 were performed at a Toshiba Aquilion ONE 320. Volumetric acquisitions of the face, orbits, or paranasal sinuses were acquired, therefore, all including the orbits, without contrast, using the following parameters: a scan range from 40 to 160 mm, 1 rotation per 0.5 seconds, a reconstruction field of view (FOV) ranging from 171 to 227 mm but mostly of 220 mm, a FC02, FC07, or FC08 filter and a FC30 filter, 120 kV tube voltage, a tube current ranging from 140 to 244 mA but mostly of 200 mA, and a CTDI volume from 12.4 to 15.9 mGy measured on a 16 cm phantom. The normal eyelid anatomy in Group 2 was evaluated using 1 mm soft tissue reconstructions both on the axial and sagittal planes perpendicular to the main axis of the eyelid. On patient #1 from Group 3, the evaluation of the bones was performed using 0.5 mm bone reconstructions both on the axial and coronal planes.

Image analysis

Images were evaluated by a Neuro and Head and Neck Radiologist with more than 20 years of experience and by a Neuroradiologist-in-Training with 4 years of experience.

In Group 1, normal eyelid anatomy on MRI was assessed in a total of 38 eyelids (19 superior eyelids and 19 inferior eyelids). This was evaluated on the axial plane in 53% of the cases and on the sagittal plane in 47% of the cases. In Group 2, normal eyelid anatomy was evaluated on CT in a total of 38 eyelids (19 superior eyelids and 19 inferior eyelids), both in the sagittal and axial planes. These MRI and CT images were compared with histologic slices of normal eyelids. Particular attention was paid to the identification of the superior and inferior tarsal plates and superior and inferior orbital septa, for which a score was created: 1: Not identified; 2: Ill-defined; 3: Well-defined; NA: Non-applicable—in cases where the structure was not included in the available slices (Table 1; Table 2).

In the 3 patients with different eyelid tumors, Group 3, the tumor localization, and invaded adjacent structures, with special attention for the tarsal plate and orbital septum, were assessed on both sagittal and axial planes and compared with the histopathologic examination after surgery (Table 3). Additionally, in one patient, the standard orbit protocol was compared with the dedicated eyelid protocol.

The final decision regarding the evaluation in all 3 groups was achieved by consensus.

RESULTS

In Groups 1 and 2, we evaluated normal eyelid anatomy on MRI and CT, respectively. On MRI, this was best achieved on the T1 and T2 sequences without fat suppression and without contrast. All eyelid layers could be identified, except for the tarsal muscles on CT and for the conjunctiva both on CT and MRI. The skin was isointense or slightly hyperintense to muscle on T1-WI and T2-WI and isodense on CT. Behind the skin, the layer with loose connective tissue had fat signal intensity and density on MRI and CT, respectively, not always being visualized on CT. The orbicularis oculi muscle was well recognized on MRI [17] and CT and seen extending peripherally beyond the edge of the anterior orbital rim. The second layer of loose connective tissue lying behind the orbicularis oculi muscle had the same imaging characteristics as the first connective tissue layer. The fifth layer of each eyelid was formed centrally by the tarsal plate and peripherally by the orbital septum. The superior and inferior tarsal plates appeared as a posterior concave or crescent-shaped line with several dots with signal intensity [15] and density of fat on MRI and CT, respectively, due to the sebaceous

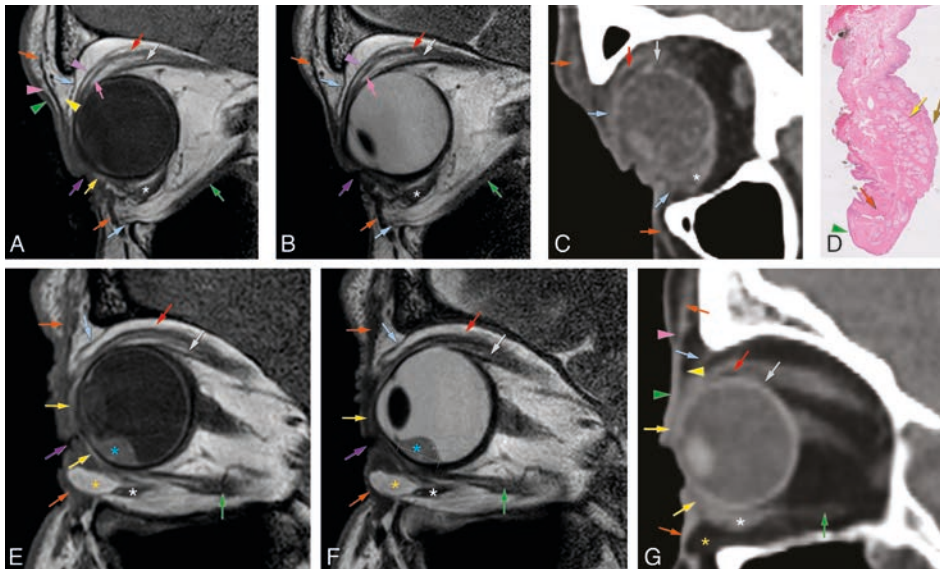


Fig. 2.

A-D - Normal eyelid anatomy on the sagittal plane on MR T1-WI (A) and T2-WI (B), on CT (C), and on pathology (D) (1x) obtained from an orbit exenteration with skin preservation.

E-G - Normal eyelid anatomy with increasing age changes on the sagittal plane on MR T1-WI (E) and T2-WI (F), and on CT (G). Notice the anterior protrusion of the orbital fat of the inferior eyelid (yellow asterisk), often occurring in older people. Further notice the uveal melanoma (blue asterisk), located inferiorly, at E and F.

Purple arrow: palpebral fissure; green arrowhead: skin; pink arrowhead: first layer of loose connective tissue; orange arrow: orbicularis oculi muscle; yellow arrowhead: second layer of loose connective tissue; yellow arrow: superior and inferior tarsal plates; blue arrow: superior and inferior orbital septa; pink arrow: superior tarsal muscle; brown arrow: conjunctiva; purple arrowhead: levator palpebrae aponeurosis; red arrow: levator palpebrae muscle; grey arrow: superior rectus muscle; white asterisk: inferior oblique muscle; green arrow: inferior rectus muscle; yellow asterisk: inferior eyelid fat protrusion; blue asterisk: uveal melanoma.

content of the meibomian glands. Although this characteristic pattern with several dots was more readily visible on MRI, it can be recognized on CT. On MRI, the superior and inferior orbital septa appeared as hypointense on T1-WI and hypointense on T2-WI, contrasting with the surrounding hyperintense fat [2,13]. On CT, they were hyperdense, in opposition to the adjacent hypodense fat. The sixth layer of the eyelids consists of the tarsal muscles, identified on MRI [2,17] and not identified on CT. The most posterior layer of the eyelid, the conjunctiva, was not seen either on MRI or on CT (Figures 2–4).

In Group 1, the visibility of the superior and inferior tarsal plates and orbital septa was scored on MRI (Table 1). Both the superior and inferior tarsal plates were identifiable in 94% of the subjects, being the superior tarsal plate well-defined in 78% and the inferior tarsal plate well-defined in 67% of the subjects. The superior tarsus was easier to identify on the axial plane. The inferior tarsus was equally well visible on the axial and sagittal planes (Figure 2A, 2E–F, and Figure 3A–D). The superior septum was always visible, being well-defined in 92% of the subjects. The inferior septum was visible in 91% of the subjects, but it was well-defined in only 36% of the subjects. The superior and inferior septa were easier to identify on the sagittal plane (Figure 2A–B, E–F, and Figure 4A–D). Orbital septa and tarsal plates were more difficult to identify when the slices were not acquired perpendicular to the main axis of the eyelid, and when movement artifacts were present. In Group 2, and similarly to Group 1, the superior and inferior tarsal plates and orbital septa were scored (Table 2). The superior tarsus was always visible, being well-defined in 63% of the subjects. The inferior tarsus was visible in 84% of

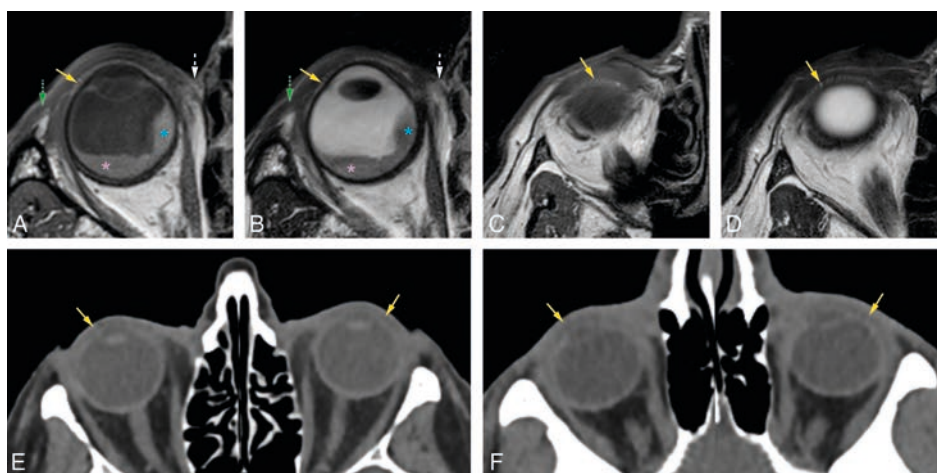


Fig. 3.

A, B and E- Normal superior tarsal plate (yellow arrow) on the axial plane on MR T1-WI (A), T2-WI (B), and on CT (E). Notice, at A and B, the uveal melanoma with associated retinal detachment, impossible to differentiate on non-contrast enhanced sequences.

C, D and F- Normal inferior tarsal plate (yellow arrow) on the axial plane on MR T1-WI (C), T2-WI (D), and on CT (F).

Yellow arrow: superior and inferior tarsal plates; green dashed arrow: lateral palpebral ligament region; white dashed arrow: medial palpebral ligament region; blue asterisk: uveal melanoma; pink asterisk: retinal detachment.

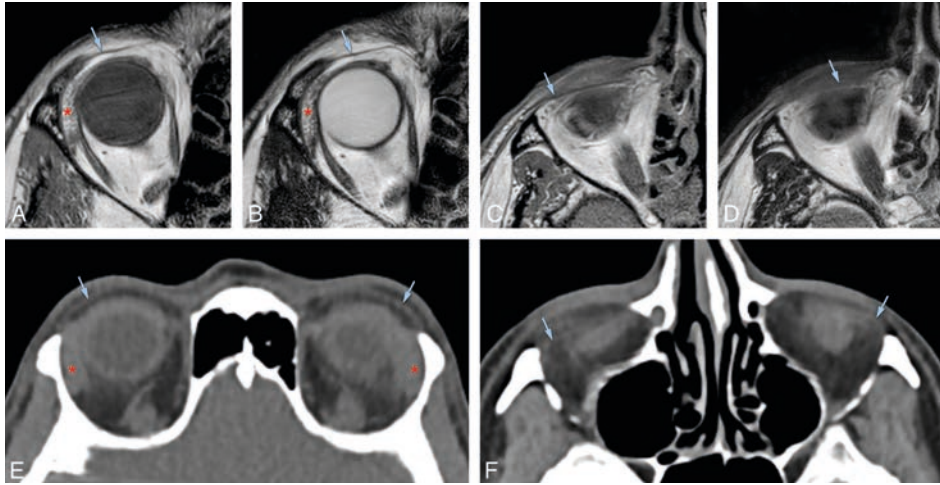


Fig. 4.

A, B and E - Normal superior orbital septum (blue arrow) on the axial plane on MR T1-WI (A), T2-WI (B), and on CT (E).

C, D and F- Normal inferior orbital septum (blue arrow) on the axial plane on MR T1-WI (C), T2-WI (D), and on CT (F).

Blue arrow: orbital septum; red asterisk: lacrimal gland.

the subjects and was well-defined in 53% of the subjects. Both the superior and inferior tarsal plates were better depicted on the axial plane than on the sagittal plane (Figure 2G and Figure 3E and F). The superior septum was visible in 89% of the subjects and well-defined in 47% of the subjects. The inferior septum was visible in 68% of the subjects, but well-defined only in 11% of the subjects. The superior and inferior septa were easier to identify on the axial plane (Figure 2C and G and Figure 4E and F) than on the sagittal plane.

In Group 3, tumor extension of 3 patients with different eyelid tumors was determined through image analysis, both on MRI and CT. The MRI of patient #1 was performed with the dedicated eyelid protocol. It showed a heterogeneous enhancing lesion of the medial aspect of the inferior eyelid on the left (Figure 5). The inferior tarsal plate (Figure 5A–B, D and F) and inferior septum (Figure 5A–B and F) were invaded, and so was the medial palpebral ligament region (Figure 5D–E). The tumor grew posteriorly, invading the orbit and reaching the region of the insertion of the inferior rectus muscle at the globe (Figure 5A–C). Due to the location of the tumor, adjacent to the medial orbital bony wall, a CT scan was also performed, but no bone invasion was noticed either on CT or on MRI. CT was able to demonstrate septal and orbital invasion as well, but underperformed compared to MRI and could not depict tarsal invasion. Due to the presence of orbital invasion, both clinically and radiologically, an eyelid-skin sparing orbital exenteration was performed. The final histopathological examination revealed a well-differentiated squamous cell carcinoma at the epithelium of the palpebral conjunctiva, growing anteriorly invading the septum and posteriorly into the intraorbital fat, surrounded by a diffuse inflammatory infiltrate. No perineural or angioinvasive extension was seen (Figure 5H–I).

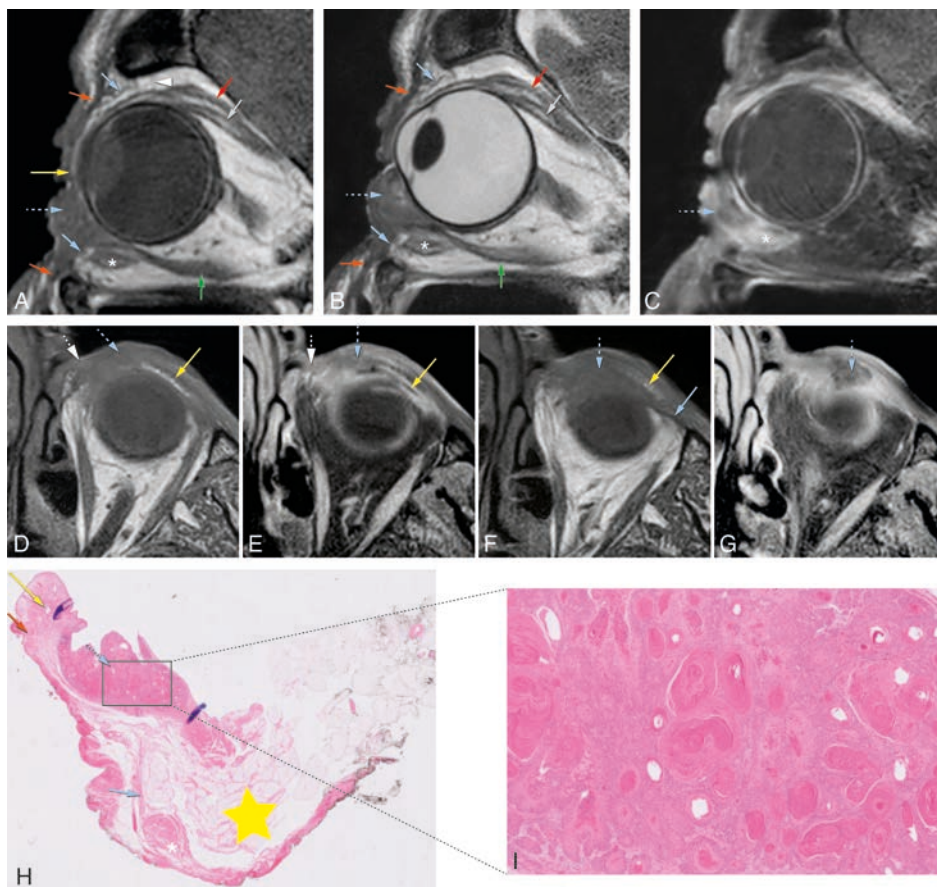


Fig. 5.

A-I - Patient #1 of Group 3 with a squamous cell carcinoma (SCC) of the left inferior tarsal and bulbar conjunctiva (dedicated eyelid protocol).

A-C - Sagittals T1-WI (A), T2-WI (B) and contrast-enhanced T1-WI with fat signal suppression (C) showing the tumor (blue dashed arrow) invading the orbit and reaching the region of insertion of the inferior rectus at the globe. D-G - Axials T1-WI (D and F) and contrast-enhanced T1-WI with fat signal suppression (E and G) at the level of the inferior eyelid (slices D and E are superior to slices F and G). Notice the tumor (blue dashed arrow) invading the medial inferior tarsal plate (yellow arrow) and medial palpebral ligament region (white dashed arrow) (D and E), and inferiorly growing behind the septum limit (blue arrow) (F and G).

H-I - Pathology hematoxylin and eosin stain (H&E) (0,5x) (H) and pathology H&E stain (5x) (I). Notice the tumor (blue dashed arrow) at the epithelium of the palpebral conjunctiva growing anteriorly invading the septum and posteriorly into the intra-orbital fat (H). Well-differentiated SCC (I).

Blue dashed arrow: tumor; orange arrow: orbicularis oculi muscle; yellow arrow: superior and inferior tarsal plates; blue arrow: superior and inferior orbital septa; white dashed arrow: medial palpebral ligament region; yellow star: intra-orbital fat; white arrowhead: superior transverse ligament (Whitnall ligament); red arrow: levator palpebrae muscle; grey arrow: superior rectus muscle; white asterisk: inferior oblique muscle; green arrow: inferior rectus muscle.

In patient #2, initially, a MRI with a standard orbit protocol was performed, followed four days later by a MRI with a dedicated eyelid protocol (Figure 6). Both showed an enhancing lesion at the medial aspect of the inferior right eyelid. With the dedicated MRI protocol invasion of the inferior tarsal plate and medial palpebral ligament region was suspected (Figure 6A–C). The relation of the tumor with the inferior tarsal plate was much more difficult to assess with the standard orbit protocol (Figure 6D–F). The medial wall of the orbit was intact on MRI. Tumor excision was performed with direct defect closure. The final histopathological examination revealed a good/moderately differentiated squamous cell carcinoma of the skin of the eyelid, with free surgical excision margins. No perineural or angioinvasive extension was found (Figure 6G–H).

In patient #3, the MRI with a dedicated eyelid protocol (Figure 7) showed post-surgical changes at the medial inferior left eyelid (not shown), due to resection of a melanotic melanoma of the bulbar conjunctiva of the medial inferior eyelid, performed 4 weeks earlier. MRI failed to show the residual/recurrent tumor at the palpebral conjunctiva of the superior left eyelid, depicting intact tarsal plate and orbital septum (Figure 7A–C). The second surgery included removal of the total palpebral conjunctiva, tarsal plate, and margin of the upper eyelid, preserving the upper eyelid skin and part of the orbicularis muscle. Histopathology showed epithelioid cell melanoma confined to the conjunctival epithelium, with free margins (Figure 7D–F). Further surgery was then performed one week later with eyelid reconstruction using a free tarsoconjunctival graft from the contralateral eyelid.

DISCUSSION

Staging of an eyelid tumor is based on the TNM classification and is a critical element in determining the appropriate treatment, a key factor defining prognosis, and will assist in the evaluation of the results of the treatment [8,9,21,22]. Regarding eyelid tumors, different T-stagings are applied depending on the type of tumor and on the layer of origin of the tumor within the eyelid. Eyelid carcinomas, including the basal cell carcinoma, squamous cell carcinoma, sebaceous carcinoma, and other rare carcinomas such as all varieties of sweat gland carcinoma, have a T-staging. Eyelid melanomas, depending on whether they arise within the skin or the conjunctiva, are staged according to the classification for skin melanoma or conjunctival melanoma, respectively. Merkel cell carcinoma is staged using the Merkel cell carcinoma staging system. These different T-stagings encompass determination of tumor dimensions and evaluation of nearby structures' invasion, namely the tarsal plate, orbital septum, orbit, globe, lacrimal sac/nasolacrimal duct, orbital walls, paranasal sinuses, and the brain [8,9]. Both dimensions and evaluation of nearby structures' invasion are not always possible through physical examination alone [6,23], with imaging needed for an accurate assessment [9]. On the one hand, according to the American Joint Committee on

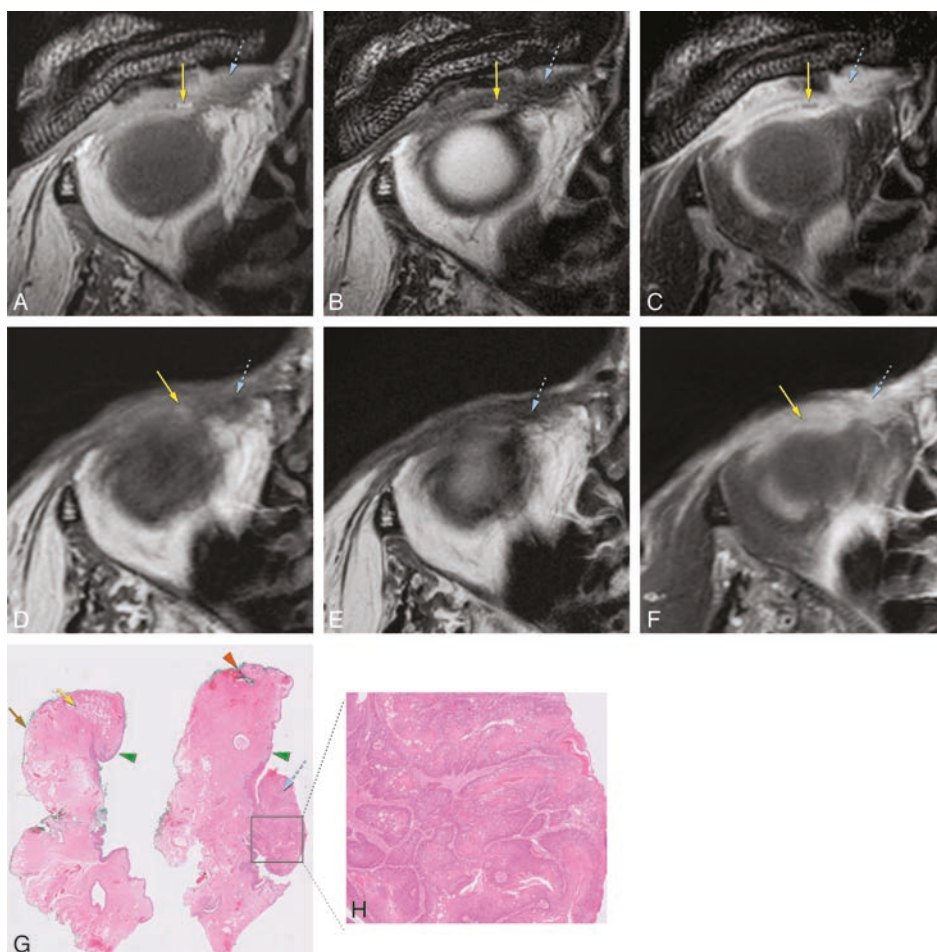


Fig. 6.

A-H - Patient #2 of Group 3 with a SCC of the skin of the right medial inferior eyelid. Comparison between a dedicated eyelid MRI protocol with a standard orbit MRI protocol and with pathology.

A-C – Dedicated eyelid protocol with axials T1-WI (A), T2-WI (B) and contrast-enhanced T1-WI with fat signal suppression (C) at the level of the inferior eyelid, showing the tumor (blue dashed arrow) involving the medial corner of the eye, with dubious involvement of the inferior tarsal plate (yellow arrow).

D-F – Standard orbit protocol with axials T1-WI (D), T2-WI (E) and contrast-enhanced T1-WI with fat signal suppression (F) at the level of the inferior eyelid. Notice the much more difficult identification of the inferior tarsal plate (yellow arrow) and its relation with the tumor (blue dashed arrow).

G and H - Pathology H&E stain (0,5x) (G) and pathology H&E stain (5x) (H). There was no slice available containing simultaneously the tumor and the tarsal plate and therefore it was difficult to evaluate tarsal invasion by the tumor. Notice that on G the left slice includes normal tarsal plate tissue (yellow arrow) but no tumor is seen, while the right slice shows the exophytic tumor (blue dashed arrow) arising from the skin but no tarsal plate tissue is seen. Skin cell proliferation compatible with good/moderately differentiated SCC (H).

Blue dashed arrow: tumor; green arrowhead: skin; yellow arrow: tarsal plate; brown arrow: conjunctiva; orange arrowhead: eyelid margin.

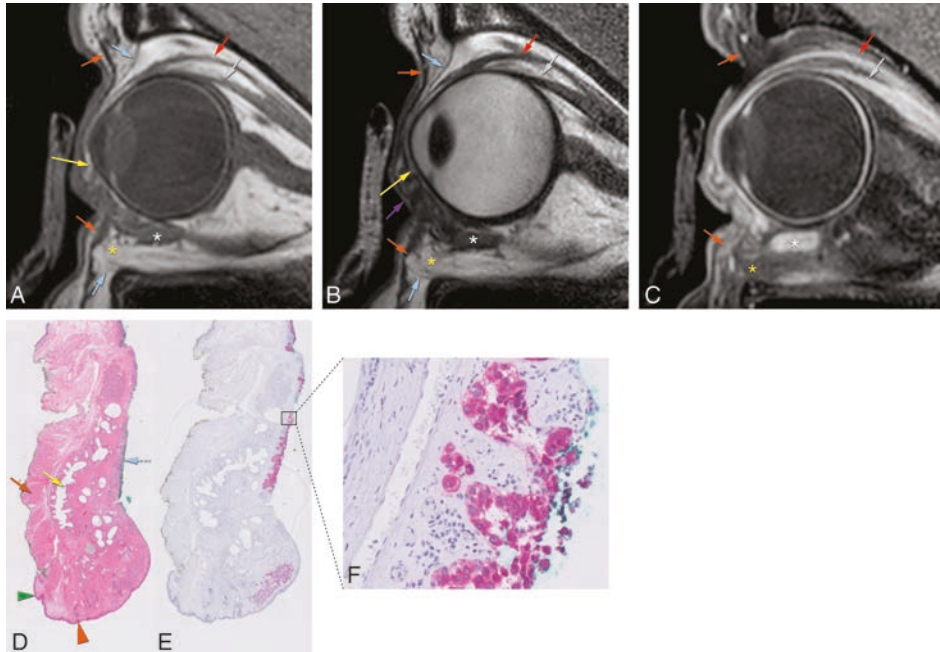


Fig. 7.

A-F - Patient #3 of Group 3 with a melanotic melanoma of the left superior tarsal conjunctiva (dedicated eyelid protocol).

A-C – Sagittals T1-WI (A), T2-WI (B) and contrast-enhanced T1-WI with fat signal suppression (C). It is not possible to visualize the tumor as it is too superficial in the conjunctiva.

D-F - Pathology H&E stain (1x) (D), pathology Melan-A stain (1x) (E) and pathology Melan-A stain (40x) (F). Notice the epithelioid cell melanoma (blue dashed arrow) confined to the conjunctiva epithelium.

Blue dashed arrow – tumor; purple arrow: palpebral fissure; green arrowhead: skin; orange arrow: orbicularis oculi muscle; yellow arrow: superior and inferior tarsal plates; blue arrow: superior and inferior orbital septa; orange arrowhead: eyelid margin; red arrow: levator palpebrae muscle; grey arrow: superior rectus muscle; white asterisk: inferior oblique muscle; yellow asterisk: inferior eyelid fat protrusion.

Cancer (AJCC) Cancer Staging Manual Eighth Edition [9], T-staging of eyelid tumors is assessed through clinical evaluation and/or after biopsy, but with imaging also playing a role in specific situations to assess invasion of the orbit, of the periorbital structures, and perineural spread. On the other hand, according to the Union for International Cancer Control (UICC) TNM Classification of Malignant Tumours Eighth Edition [8], T-staging of eyelid malignancies is assessed only by physical examination or after excision, with no mention of imaging. Although the AJCC considers imaging in some situations regarding the T-staging of eyelid carcinomas and conjunctival melanomas, imaging evaluation of the tarsal plates and orbital septa is never specifically mentioned [8,9].

While imaging characterization of orbital tumors often includes mention of the integrity of the globe, orbital bone walls, paranasal sinuses, and the brain [24–27], one seldom finds references to the eyelid [2,17,18]. To evaluate tumoral invasion of the eyelid structures, in particular of

the tarsal plate and orbital septum, which have important therapeutic implications [28,29], accurate knowledge of the complex eyelid anatomy is, therefore, required.

Normal eyelid anatomy has scarcely been a subject of published material, both in MRI [2,11–17] and CT. To our knowledge, there has been no publication addressing this subject on CT. For the correct analysis of MR and CT data, sagittal and axial images should be obtained, perpendicular to the main eyelid axes. A standard orbit MRI protocol, acquired with a head coil, has a suboptimal resolution, as shown in patient #2 of Group 3, and, therefore, a dedicated eyelid MRI protocol should be employed. One of the main elements of such a protocol is the use of a surface coil, which allows for high-resolution imaging, with an in-plane resolution of $<0.5 \times 0.5 \text{ mm}^2$. On CT, a slice thickness reconstruction of 1 mm is suitable for the evaluation of the eyelids.

Our evaluation showed that all eyelid layers could be identified, except for the tarsal muscles on CT and for the conjunctiva both on MRI and CT.

Evaluation of invasion of the tarsal plate and the orbital septum is part of the T-staging of most eyelid tumors, and their invasion has direct therapeutic implications. On the one hand, in a tumor confined to the eyelid, which is treated with local resection and reconstructive surgery [6,28,30], knowledge about the presence of tarsal invasion preoperatively is indispensable in planning surgical reconstruction, and adequate information cannot be obtained solely by physical examination. On the other hand, when the orbital invasion is present, an orbital exenteration must be considered [27,29,31]. Notice that in tumors arising from an eyelid layer in front of the orbital septum, such as tumors of the skin of the eyelid, orbital invasion occurs via invasion of the orbital septum, while tumors of the conjunctiva will have direct access to the intraorbital contents since the conjunctiva is located behind the septum limit. Although orbital invasion can be suspected clinically, for example, when signs of eye muscle involvement, such as strabismus or diplopia [30,32], are present, image-based evaluation is necessary, especially in case of non-clinical suspected orbital invasion [25,32]. The recognition of the tarsal plates and orbital septa, both on MRI and CT, is, therefore, crucial in order to evaluate whether they are invaded by an eyelid tumor and, therefore, their visualization on MRI and CT was scored. Although MRI has a higher soft-tissue resolution, the results using CT were positively surprising.

Regarding the tarsal plates, our results show that they are visible most of the time on both CT and MRI, although with a better definition on MRI. The superior tarsal plate was visible in 94% of the subjects on MRI and was always visible on CT. This was probably due to the fact that the patients of Group 1 were not scanned specifically to assess the eyelids, resulting in suboptimal MR-images for their evaluation, with only either axial or sagittal images available and not always perpendicular to the main axes of the eyelid. On the contrary, on CT, both axial and sagittal reformats perpendicular to the main axes of the eyelid were available. The inferior tarsal plate was always easier to depict on MRI, even when suboptimal MR-images were used. Axial planes should be chosen over sagittal planes to identify the tarsal plates, with

the superior tarsal plate being more readily recognizable due to its larger size. The superior and inferior tarsal plates continue laterally to the orbital bone rim as medial and lateral palpebral ligaments, both possible to identify on MRI [13,14] (Figure 3A–B).

Regarding the orbital septa, our results show both to be mostly visible on MRI and CT, but a better definition was generally achieved on MRI. The superior and inferior orbital septa were easier to identify on the sagittal plane on MRI, while on CT, their identification was easier on the axial plane. Both on MRI and CT, the inferior septum is more difficult to see than the superior septum. This is not only due to its smaller size, but also because the shape of the inferior orbital septum changes with aging [33,34], with the protrusion of the intraorbital fat anteriorly displacing the inferior septum against the orbicularis oculi muscle and making it difficult to tell them apart (Figure 2E–G).

The literature on eyelid tumors mentions the role of imaging, either MRI or CT, mainly in large tumors in which orbital invasion is present [25,30]. With this work, we were able to demonstrate the potential use of MRI, and to a lesser extent of CT, in the identification of tumor invasion of small anatomical structures in the eyelid, important in the TNM classification, such as the tarsus and the orbital septum, which are not clinically accessible. Because of its superior soft-tissue contrast and spatial resolution, MRI is the modality of choice to evaluate the extension of an eyelid tumor. Moreover, with MRI, diffusion, and perfusion-weighted imaging will help to differentiate between the malignant tumor and potentially surrounding inflammation. The use of a surface coil is optimal for the evaluation of tumor extension in the eyelid, but also for the invasion of adjacent structures by an eyelid tumor. Although surface coils are less suitable for assessing the deeper aspect of the orbit, such as the orbital apex, imaging thereof is generally not necessary in the context of an eyelid tumor. The perineural spread is the exception, and, ideally, an axial contrast-enhanced T1-weighted with fat signal suppression using a head coil should be performed in order to image the orbital apex and cavernous sinus adequately. Additionally, because part of the contralateral eyelid is sometimes used to reconstruct the eyelid where the tumor had been resected [7], an additional axial T1-WI from the contralateral normal eyelid could also be acquired to aid with the surgery planning. These images could furthermore be used as a reference to better interpret the pathologic side. CT should mainly be used as a complementary technique in the evaluation of bone invasion [24,27,34]. In cases where MRI cannot be performed, CT has some potential in the evaluation of tumor extension, as it allows for the visualization of most of the eyelid structures, although further studies are needed to fully establish the clinical value of CT for eyelid tumors.

In this study, we assessed the usefulness of MRI and CT images in the delineation of eyelid tumors and their relation to the surrounding eyelid structures, by confronting image data of three patients with surgical findings and histopathology. The MR-images of patient #1 showed invasion of the inferior tarsal plate, inferior septum, and orbit as far dorsally as the insertion of the inferior rectus muscle at the globe. While septum and intraorbital invasion could also

be visualized on CT, the tarsal invasion was not evident. Histopathology confirmed both the septum and orbital invasion, but the tarsus invasion was not accessed and, therefore, could not be confirmed but also not excluded. That is because although with MRI the whole tumor is evaluated, histopathology slices can only be made in one plane, mainly planned to evaluate whether free surgical margins exist, not always matching those of imaging and not covering the whole tumor. As a result, on the evaluation of whether a specific eyelid structure is invaded by the tumor, histopathology can only act as the gold standard when positive, while when histopathology findings are negative, they do not necessarily invalidate MRI findings. Based on the MRI of patient #2, invasion of the inferior tarsal plate was suspected. This could not be confirmed on histopathology, again due to the lack of spatial correlation between imaging and histologic slices. The MRI of patient #3 did not show the tumor, clinically located at the palpebral conjunctiva of the superior eyelid, meaning that the superior tarsal plate and superior septum were intact. Histopathology confirmed that the tumor was superficial and confined to the conjunctival epithelium.

When evaluating CT or MR-images with eyelid tumors, radiologists must be familiar with both the complex eyelid anatomy and its imaging and with criteria in tumor staging. Moreover, the tumor location must be known before the MRI-exam, by seeing either the patient or the patient's photograph, in order to correctly plan the adequate MRI scans, as these small lesions are often not visible on the low-resolution images that are used to plan the higher resolution acquisitions. As in other areas of medicine, a multidisciplinary approach should be encouraged, as contributions from both radiologists and ophthalmologists may lead to better information gathering needed in treatment planning, with a positive impact on the patient's outcome.

Our study has some limitations. First, the evaluation of the healthy eyelid anatomy was done retrospectively, thus a dedicated eyelid MRI protocol was not used. As a result, only one single orientation, either sagittal or axial, was available, and these slices were sometimes not planned perpendicular to the main axes of the eyelid. Furthermore, some technical aspects of the dedicated eyelid protocol, such as the localized shimming, have not been applied to the patients of the healthy eyelid group. Secondly, the local extension of eyelid tumors was only evaluated on three patients. Finally, an accurate correlation between tomographic imaging and histopathological examination is not always possible.

CONCLUSION

Despite the small size of the various components of eyelid anatomy and although imaging the eyelid is challenging due to susceptibility and motion artifacts, the delineation of most of the eyelid structures is possible with an optimized MRI protocol, and to a lesser extent with CT. MR imaging is, therefore, important for the assessment of tumor invasion of the tarsal

plate and orbital septum, having an important contribution to the T-staging of eyelid tumors, which may improve treatment planning and may have a positive impact on both patients' short time morbidity and longtime outcome.

REFERENCES

1. Henri R, Andre D, Vincent D. *Anatomia Humana Descriptiva, Topografica Y Funcional. Tomo 1. Cabeza Y Cuello*; Elsevier Masson: Paris, France, 2005.
2. Hoffmann KT, Hosten N, Lemke AJ, Sander B, Zwicker C, Felix R. Septum orbitale: High resolution MR in orbital anatomy. *Am J Neuroradiol.* 1998 Jan;19(1): 91–94.
3. Sayoc BT. Anatomic considerations in the plastic construction of a palpebral fold in the full upper eyelid. *Am J Ophthalmol.* 1967 Jan;63(1):155–158.
4. Kakizaki H, Malhotra R, Selva D. Upper eyelid anatomy: an update. *Ann Plast Surg.* 2009 Sep;63(3):336–343.
5. Pe'er J. Pathology of eyelid tumors. *Indian J Ophthalmol.* 2016 Mar;64(3):177–190.
6. Silverman N, Shinder R. What's New in Eyelid Tumors. *Asia Pac J Ophthalmol (Phila).* 2017 Mar-Apr;6(2):143–152.
7. Pe'er J, Singh AD, Damato BE. *Clinical Ophthalmic Oncology*; Springer International Publishing: Berlin, Germany, 2019.
8. Brierley JD, Gospodarowicz MK, Wittekind C. *TNM classification of malignant tumours - 8th edition*; 2017.
9. Edge MB, Greene S, Byrd F, Brookland DR, Washington RK, Gershenwald MK, Compton JE, Hess CC, Sullivan KR, Jessup DC. (Eds) *Ajcc Cancer Staging Manual, 8th edition*; Springer International Publishing: Cham, Switzerland, 2017.
10. Sun MT, Andrew NH, O'Donnell B, McNab A, Huilgol SC, Selva D. *Periocular Squamous Cell Carcinoma: TNM Staging and Recurrence.* *Ophthalmology* 2015.
11. Goldberg RA, James C, Jesmanowicz A, Hyde JS. Eyelid Anatomy Revisited: Dynamic High-Resolution Magnetic Resonance Images of Whitnall's Ligament and Upper Eyelid Structures with the Use of a Surface Coil. *Arch Ophthalmol.* 1992 Nov;110(11):1598–1600.
12. Miyake I, Tange I, Hiraga Y. MRI findings of the upper eyelid and their relationship with single- and double-eyelid formation. *Aesthetic Plast Surg.* 1994 Spring;18(2):183–187.
13. Ettl A, Salomonowitz E, Koornneef L, Zonneveld FW. High-resolution MR imaging anatomy of the orbit: Correlation with comparative cryosectional anatomy. *Radiol Clin North Am.* 1998 Nov;36(6): 1021–1045.
14. Ettl AR, Salomonowitz E, Koornneef L. Magnetic resonance imaging of the orbit: Basic principles and anatomy. *Orbit.* 2000 Dec;19(4):211–237.
15. Georgouli T, Chang B, Nelson M, James T, Tanner S, Shelley D, Saldana M, McGonagle D. Use of high-resolution microscopy coil MRI for depicting orbital anatomy. *Orbit.* 2008;27(2):107–114.
16. Meyer DR, Linberg JV, Wobig JL, McCormick SA. Anatomy of the orbital septum and associated eyelid connective tissues: Implications for ptosis surgery. *Ophthalmic Plast Reconst. Surg.* 1991;7(2):104–113.
17. Hayman LA, Maturi RK, Pflieger MJ, Diaz-Marchan P, Horowitz B, Tang RA, Soparkar CNS, Patrinely JR. MR imaging of the eyelids: normal and pathologic findings. *Am J Roentgenol.* 1995 Sep;165(3):639–644.
18. Budak MJ, Weir-McCall JR, Yeap PM, White RD, Waugh SA, Sudarshan TAP, Zeally IA. High-resolution microscopy-coil MR-imaging of skin tumors: Techniques and novel clinical applications. *Radiographics* 2015 Jul-Aug;35(4):1077-1090.

19. Ferreira TA, Fonk LG, Jaarsma-Coes MG, van Haren GGR, Marinkovic M, Beenakker J-WM. MRI of uveal melanoma. *Cancers (Basel)*. 2019 Mar 17;11(3):377.
20. Tudorica LA, Oh KY, Roy N, Kettler MD, Chen Y, Hemmingson SL, Afzal A, Grinstead JW, Laub G, Li X, Huang W. A feasible high spatiotemporal resolution breast DCE-MRI protocol for clinical settings. *Magn Reson Imaging*. 2012 Nov;30(9):1257-1267.
21. Esmaeli B, Nasser QJ, Cruz H, Fellman M, Warneke CL, Ivan D. American joint committee on cancer T category for eyelid sebaceous carcinoma correlates with nodal metastasis and survival. *Ophthalmology*. 2012 May;119(5):1078-1082.
22. Kaliki S, Gupta A, Ali MH, Ayyar A, Naik MN. Prognosis of eyelid sebaceous gland carcinoma based on the tumor (T) category of the American joint committee on cancer (AJCC) classification. *Int Ophthalmol*. 2016 Oct;36(5):681-690.
23. Lober CW, Fenske NA. Basal cell, squamous cell, and sebaceous gland carcinomas of the periorbital region. *J Am Acad Dermatol*. 1991 Oct;25(4):685-690.
24. Glover AT, Grove AS. Orbital invasion by malignant eyelid tumors. *Ophthalmic Plast Reconstr Surg*. 1989;5(1):1-12.
25. Leibovitch I, McNab A, Sullivan T, Davis G, Selva D. Orbital invasion by periocular basal cell carcinoma. *Ophthalmology*. 2005 Apr;112(4):717-723.
26. Soysal HG, Markoç F. Invasive squamous cell carcinoma of the eyelids and periorbital region. *Br J Ophthalmol*. 2007 Mar;91(3):325-329.
27. Sun MT, Wu A, Figueira E, Huilgol S, Selva D. Management of periorbital basal cell carcinoma with orbital invasion. *Future Oncol*. 2015 Nov;11(22):3003-3010.
28. Wójcicki P, Zachara M. Surgical treatment of eyelid tumors. *J Craniofac Surg*. 2010 Mar;21(2): 520-525.
29. Costan VV, Boisteanu O, Sulea D, Popescu E. The management of skin tumors extended to the orbit. *Medial-Surg J Rev Med Chir*. 2018 122:737-743.
30. Yin VT, Merritt HA, Sniegowski M, Esmaeli B. Eyelid and ocular surface carcinoma: Diagnosis and management. *Clin Dermatol*. 2015 Mar-Apr;33(2):159-169.
31. Donaldson MJ, Sullivan TJ, Whitehead KJ, Williamson RM. Squamous cell carcinoma of the eyelids. *Br J Ophthalmol*. 2002 Oct;86(10):1161-1165.
32. Howard GR, Nerad JA, Carter KD, Whitaker DC. Clinical characteristics associated with orbital invasion of cutaneous basal cell and squamous cell tumors of the eyelid. *Am J Ophthalmol*. 1992 Feb 15;113(2):123-133.
33. de la Plaza R, Arroyo JM. A new technique for the treatment of palpebral bags. *Plast Reconstr Surg*. 1988 May;81(5):677-685.
34. Darcy SJ, Miller TA, Goldberg RA, Villablanca JP, Demer JL, Rudkin GH. Magnetic resonance imaging characterization of orbital changes with age and associated contributions to lower eyelid prominence. *Plast Reconstr Surg*. 2008 Sep;122(3):921-929.

5

**Summary, discussion,
future perspectives and conclusion**



This thesis describes the development of dedicated high-resolution MRI protocols for evaluation of the eye and of the eyelid and their application in the characterization of uveal melanoma and of the eyelid anatomy. Furthermore, it focuses on the characterization of orbital inflammation on MRI and CT, its differentiation from orbital tumors and infection, and how to distinguish the most common orbital inflammatory diseases.

It is the result of almost a decade of close work between myself, as a radiologist, a physicist, radiology technicians, ophthalmologists, pathologists, other radiologists, radiation oncologists, clinical scientists from Philips and other PhD students from different disciplines.

Solving clinical problems lies at the heart of the research described in this thesis, therefore this research improved the diagnosis and treatment of specific disease entities, with a clear benefit for the patient. This can only be done properly within a multidisciplinary team, as we have. Hippocrates:

“The health and well-being of my patient will be my first consideration”.

In: last revision of the Declaration of Geneva (2017) (World Medical Association).

Radiology is continuously evolving and improving. It involves image interpretation, but also the improvement of image quality and the development of new techniques and for the latter, radiologists need the help of physicists and of radiology technicians. In our research group, a physicist together with a radiology technician developed the high-resolution MR images, in collaboration with the radiologist, but tailored to the clinical needs understood during the close work between the different medical specialties. The different input from the different medical specialties, complementing each other, is of utmost importance.

5.1 UVEAL MELANOMA

Eye MRI protocol

Despite the challenges of susceptibility artefacts and eye motion when imaging the eye with MR, good quality multiparametric MR images of the eye and UM can be obtained.

In **chapter 2.1** an *eye 3T MRI protocol* was developed. First, several different sequences were performed in 9 uveal melanoma patients, at 3T using an eye-coil. These sequences included multi-slice (MS) sequences with 1 and 2 mm, 3D turbo spin-echo (TSE) sequences with 0.8 and 1 mm, 3D turbo field-echo (TFE) sequences with 0.8 mm, non-EPI TSE DWI with 2.4 mm and b values of 0, 400 and 800 s/mm² and apparent diffusion coefficient (ADC), and a dynamic contrast enhanced (DCE) sequence with 1.5 mm and a temporal resolution of 2 sec. In-plane images were evaluated for general image quality, contrast, identification of the sclera and tumor limits and differentiating the tumor from retinal detachment. The isotropic sequences were evaluated regarding geometrical accuracy and identification of the sclera. The DWI sequences were evaluated in terms of signal-to-noise ratio (SNR), distortion and contrast resolution. The quality of the DCE curves was assessed, in particular with respect to eye motion and consequent misregistration artefacts. After evaluation of all these sequences a dedicated eye MRI protocol was designed. This clinical protocol consisted of MS 2 mm 2D sequences (T1, T1 with fat signal saturation after contrast and T2) and a non-EPI TSE DWI (b values of 0 and 800 s/mm²) and ADC, acquired perpendicular to the main axis of the tumor. It also included isotropic 3D TSE sequences (T1, T1 with fat signal saturation before and after contrast and T2) and a DCE sequence, acquired on the axial plane non-angulated. The MS 2 mm 2D sequences have the highest in-plane resolution and are therefore the best for lesion characterization and local extension evaluation. The isotropic 3D TSE sequences allow retrospective reformatting in all directions and 3D reconstructions, and are essential to assess tumor geometry and accurate size measurements. The DWI and PWI sequences aid in the differential diagnosis, and potentially, provide prognostic information, predict treatment response and permit earlier assessment of tumor response to radiotherapy than US. Overall, this dedicated eye 3T MRI protocol provides high resolution MR-images of UM, crucial to improve its diagnosis, treatment planning and follow-up, and moreover it can also be used for other ocular lesions.

Before starting evaluating UM at 3T, we assessed them at 7T MRI because of its high-field strength, for which we had also developed an *eye 7T MRI protocol*. Our research group prospectively compared the diagnostic performance of 7T and 3T to evaluate the eye and UM. On one hand, with 7T the highest quality images could be obtained under optimal conditions. On the other hand, severe artefacts making an exam undiagnostic are more common (2D sequences of diagnostic quality on 69% on 7T, compared to 99% on 3T). On average, 2D MS

sequences image quality was better on 3T compared to 7T, and 3D SE sequences image quality and measuring tumor dimensions, were comparable between 3T and 7T [1].

Furthermore, our research group developed, both for 3 and 7 T, an *eye silicon oil MRI protocol* as an extension of the eye MRI protocol. This protocol corrects for the strong off-resonance effects caused by the silicon oil (SiOil) tamponade in patients after vitrectomy. Since the presence of intraocular SiOil prevents US imaging, these patients would generally be enucleated, as diagnosis, treatment planning and subsequent follow-up would be impossible. This dedicated protocol made possible for some patients with UM in eyes with silicon oil to save their eye and vision [2].

Finally, our research group developed, together with the HollandPTC, an *eye pre-proton beam therapy 3T MRI protocol*, for accurate measurement of the clip-tumor distances. In ocular proton beam therapy, 2.5 mm tantalum clips are surgically sutured near the UM border for clinical target volume marking. Conventionally, the clip-tumor distances are assessed peroperatively using transillumination, indentation and/or funduscopy. The protocol developed permits the assessment of the clip-tumor distances with MRI and our research group retrospectively evaluated it on 23 UM patients. Moreover, the eye biometry was evaluated with MRI and compared with conventional ophthalmic measurements. MRI turned out to be less accurate on the evaluation of the clip-tumor distances in case of flat UM, because the limits of these tumors are more difficult to determine on MRI. However, MRI was more reliable on the evaluation of the eye length, and on measuring the clip-tumor distances of anterior located and mushroom shaped tumors. MR imaging of these patients will result in more accurate target definition, thereby possibly reducing toxicity and improving probability to retain vision [3]. Although we were the first center to include an MRI for all ocular proton therapy patients, more centers are now including MRI in their workflow and using protocols which are based on ours [4].

MR imaging characteristics of uveal melanoma

In **chapter 2.2** the MR imaging anatomical and functional characteristics of 42 uveal melanomas were assessed, MR features were compared with funduscopy and ultrasound, and on 14 enucleated cases with histopathology.

UM with complex tumor-shapes, such as a mushroom configuration, should be recognized because they would benefit from special attention at the radiotherapy planning. This study showed the importance of the multiplanar reconstructions for its recognition and was consistent with the known fact that the mushroom configuration of a UM is associated with breaks in Bruch's membrane. Tumor pigmentation is important in the differential diagnosis with other intraocular masses and it may have prognostic significance [5], although the latter warrants further analysis [6]. A significant relationship between the signal intensity on T1

and pigmentation on histopathology was found ($p=0.024$). T1-hyperintense UM were always moderately or strongly pigmented on histopathology, while T1-hypointense UM were either pigmented or non-pigmented. This is valuable because the assessment of tumor pigmentation with fundoscopy is not representative in the case of heterogeneous UM and it may be difficult in case of retinal detachment. The ADC of the UM was $1.16 \pm 0.26 \times 10^{-3} \text{ mm}^2/\text{s}$. Two-thirds of the UM had a wash-out and the remaining a plateau perfusion time-intensity curve (TIC) and the mean peak intensity of UM was 1.62. An increase of tumor ADC correlated with a plateau TIC ($p=0.011$). Both the presence of monosomy 3 and of extracellular matrix patterns “loops” are important determinants of poor prognosis and they frequently coexist. The study from Kamrava et al. found a significant correlation between monosomy 3 and perfusion values such as higher k^{trans} and v_e [7]. Interestingly, in our study, it seems that UM with loops also tend to have different perfusion values than UM without loops, such as a shorter time to peak and a bigger peak intensity, consistent with the fact that extracellular matrix patterns are pseudovascular channels. Knowing the ADC and perfusion characteristics is valuable for the differential diagnosis with other intraocular masses. Furthermore, PWI looks promising on the identification of UM at higher risk of metastasis, which could serve as a substitute for histopathology in patients that undergo an eye-sparing treatment, but needs further investigation.

Assessment of tumor size is essential for the choice of treatment modality and planning of radiotherapy. MRI was limited in evaluating the basal diameter of flat tumors with a tendency to underestimate the size due to unclear tumor margins. In comparison to MR, US tends to overestimate tumor size, showing larger tumor prominence (0.5mm larger, $p=0.008$) and largest basal diameter (1.4mm larger, $p<0.001$). An increase of tumor prominence was associated with lower ADC values ($p=0.030$) and favored a wash-out TIC ($p=0.028$).

The local extension of a UM should be assessed so that it can be taken into account in the treatment plan. Moreover, the presence of extraocular growth and of optic nerve invasion is associated with an increased rate of orbital recurrence and poorer prognosis. MRI was good in diagnosing ciliary body involvement, extrascleral extension and optic nerve invasion, but contrarily to what has been previously reported, limited on identifying scleral invasion.

MR imaging follow-up of UM after brachytherapy and proton beam therapy

Foti et al showed that in UM treated with proton-beam therapy, ADC variations precede volume changes, and early change in ADC value 1 month after therapy significantly correlated with tumor regression [8]. The value of DWI and PWI in the follow-up of UM after both brachytherapy and proton-beam therapy needs to be further evaluated, which our research group is currently doing. As preliminary results, PWI especially showed favorable changes before volume changes, enabling an earlier assessment of UM response to radiotherapy than US. This is reassuring both for the clinicians and for the patients.

Clinical value and impact of MR imaging of UM

MRI enabled high quality images of the globe and UM. It is however more expensive than US and it seemed relevant to assess whether MRI would have an added economic value for UM treatment. Our research group therefore retrospectively evaluated on 60 patients whether the extra cost of an MRI generated economic benefit or change in optimal treatment. Tumor measurements are more accurate with MRI than with US and they are critical for the choice of treatment modality. Smaller tumors can be eligible for brachytherapy, while larger tumors will undergo more expensive treatments such as enucleation or proton beam therapy. Our study showed that, if only the costs of treatment are considered, an additional MRI is cost-effective for patients where there is doubt on the accuracy of US measurements, if the tumor appears to be slightly too large for brachytherapy, and in UM patients who cannot be evaluated with US and would otherwise undergo enucleation. In 10% of patients with intermediate tumor size MRI indicated a smaller tumor prominence than US, resulting in a change from PBT or enucleation to brachytherapy. This decreases the costs by €24,000, while the costs of MRI are €200-1000. Moreover, MRI adds value in terms of quality of care, as it enables for some patients to be afforded a treatment modality that spares more of their vision, the annual total economic burden of severe vision impairment associated with eye removal being €10.000 [9,3].

The LUMC is the National Reference Center for UM in The Netherlands, receiving approximately 220 UM per year [10]. The evaluation of UM with MRI brought several advantages and has changed clinical practice in our hospital. Before our research rarely a UM patient would receive an MRI before treatment. Nowadays we perform MRI in several circumstances. Firstly, whenever the ophthalmologist cannot evaluate an ocular mass, because something is obscuring the view on fundoscopy or US, either blood opacifying the ocular media or the presence of silicon oil. Secondly, whenever there is doubt about the diagnosis of UM. Thirdly, when there is doubt about measurements or local extension, as MRI is more accurate than US, in order to choose the best treatment. Fourthly, before PBT, pre-clips positioning mainly for accurate tumor and eye dimensions, post-clips placement for determination of the clip-tumor distances. Fifthly, in the early follow-up after brachytherapy and PBT in order to assess response to treatment, and we are currently evaluating the best time-point/indications. Sixthly, in the follow-up after enucleation, in particular when extra-scleral extension was known to be present. Finally, in the follow-up of UM after treatment whenever eye or orbital recurrence is suspected. On average we scan 3 to 4 UM per week. Overall MRI increased the precision of UM treatment.

Our eye 3T MRI protocol has also caught the interest of several other foreign centers, in Europe but also in the United States, and in collaboration with Philips, is now available online. Furthermore, our UM results will be part of the new edition of the WHO Classification of Tumours of the Eye Book.

Future perspectives

An important goal in ocular MR imaging in the near future is to further improve the differential diagnosis of ocular masses, where we expect MRI to have a pivotal role. We have evaluated the MR imaging characteristics of UM, the ones of retinoblastoma had already been assessed [11-16], but the MR imaging features of other common benign and malignant intraocular masses still need to be known and published, which we are currently investigating. Benign ocular lesions are expected to have higher ADCs [17] and mostly a progressive or plateau TIC at DCE, although functional evaluation of choroidal nevi can still be hampered by their very small size. In other intraocular malignant lesions, such as metastases and lymphomas, the main clues for the differential diagnosis are the lesion number, configuration and signal intensity. For example, in the study from Lemke et al. with 200 UM, no tumor had a flat-placoid shape [18], which is the predominant shape of ocular metastases.

Additionally, 3D MRI-based ocular proton therapy treatment planning, without the need for tantalum clips placement, is desirable, and our research group is currently working on this [19].

Finally, the promising value of PWI on the identification of UM at higher risk of metastasis, as noticed both in our study and in the study from Kamrava et al [7]., needs further investigation, as it could serve as a substitute for histopathology in patients that undergo an eye-sparing treatment. To this end, we have recently further improved quantification of PWI, by correcting for eye-motion and the confounding effect of tumor pigmentation [20].

5.2 ORBITAL INFLAMMATION

In **chapter 3.1** the CT and MR imaging characteristics of scleritis were retrospectively evaluated in 11 cases in which CT and/or MR imaging were performed during the active phase of the disease. The imaging findings of scleritis were scleral enhancement (100%) (may involve the whole sclera or be preferentially peripheral), scleral thickening (83%), and focal periscleral cellulitis (42%). MR imaging is the most useful examination in the diagnosis of scleritis, differentiating the sclera from the other ocular layers, but scleritis could also be accurately diagnosed on CT. Scleritis is almost invariably of inflammatory etiology – idiopathic, in the spectrum of idiopathic orbital inflammation (IOI), or in the context of a systemic disease. Infectious scleritis is rare. Scleritis can occur isolated or in association with other orbital abnormalities. It is important not to misdiagnose it for a tumor. Clues to the inflammatory (versus neoplastic) nature of the process include the presence of pain, cellulitis and the specific sclera location.

In **chapter 3.2** a literature review was carried out regarding the imaging protocols and characteristics of orbital inflammation. MR imaging is the modality of choice for the

evaluation of orbital inflammation because of its superior soft tissue contrast and spatial resolution, as well as its ability to generate functional images such as diffusion and perfusion weighted imaging, crucial for distinguishing benign from malignant lesions. The specific radiological characteristics of inflammation affecting the various orbital structures, such as of scleritis, uveitis, dacryoadenitis, optic perineuritis and optic neuritis, myositis and orbital cellulitis, were described. Furthermore, the imaging characteristics of specific inflammatory diseases, such as of IOI, sarcoidosis, thyroid-associated orbitopathy (*Graves Disease*), Immunoglobulin G4-related Disease (IgG4 RD), granulomatosis with polyangiitis (*Wegener granulomatosis*), idiopathic sclerosing orbital inflammation (ISOI) and *Erdheim-Chester* disease were presented. Finally, different imaging and clinical clues were combined in a decision tree, that will allow one to recognize an orbital solid enhancing lesion as inflammatory, and not as infection or tumor. Subsequently, we have shown that the orbital radiological pattern found can point to an underlying inflammatory disease or at least shorten its differential diagnosis. Overall, these considerations enable the treating physician to establish an adequate treatment and at times a biopsy can be avoided.

Clinical value and impact of MR imaging of orbital inflammation

Before this research into orbital inflammation, MRI was already the exam of choice both for orbital inflammation and for an orbital tumor, and the MRI protocol in LUMC already included DWI. But it did not include PWI, and at that time, we decided to add PWI to our orbit protocol. These studies, together with the experience gained with the use of PWI, gave us much more confidence to make the differentiation between the infectious, inflammatory and malignant nature of an orbital lesion. That changed clinical practice in our hospital. Since then, whenever the MRI characteristics of an orbital lesion are suggestive of inflammation, the clinical symptoms and laboratory results are consistent and if the lesion is not of easy access with biopsy, the ophthalmologists in LUMC will consider to start medical treatment without histopathological confirmation. This is less invasive for the patient and less costly.

Future perspectives

In differentiating a benign from a malignant orbital mass, the contribution of the DWI (ADC and IVIM) has been recently further investigated in a quantitative way [21,22], and so has the value of DCE [23-25]. However, the specific diffusion and perfusion characteristics of the different orbital tumors and orbital inflammation should still be a focus of attention, which will further help in the differential diagnosis of orbital masses.

5.3 EYELID

In **chapter 4.1** a retrospective evaluation of the normal eyelid anatomy, in terms of identification of the eyelid layers, on MRI and CT was performed, in 38 normal eyelids. Furthermore, tumor extension was assessed in three eyelid tumors and validated with histopathology. Despite the small size of the various components of eyelid anatomy and although imaging the eyelid is challenging due to susceptibility and motion artifacts, the identification of most of the eyelid structures is possible with an optimized MRI protocol, including the use of a surface coil, and to a lesser extent with CT. Axial planes should be chosen over sagittal planes to identify the tarsal plates, with the superior tarsal plate being more readily recognizable due to its larger size. The superior and inferior orbital septa were easier to identify on the sagittal plane on MRI, while on CT their identification was easier on the axial plane. Both on MRI and CT the inferior septum is more difficult to see than the superior septum. MRI is the modality of choice to evaluate the extension of an eyelid tumor due to the high resolution and with diffusion and perfusion weighted imaging helping to differentiate between the malignant tumor and potentially surrounding inflammation. A surface coil is optimal for the evaluation of tumor extension in the eyelid, but also for the invasion of adjacent structures by an eyelid tumor. CT should mainly be used as a complementary technique in the evaluation of bone invasion. The application of the image eyelid anatomy knowledge on the evaluation of eyelid tumors extension was limited, since only 3 patients were evaluated, and because an accurate correlation between imaging and pathology is not possible and therefore pathology cannot always act as the gold standard for the evaluation of the MRI findings. As the assessment of tumor invasion of the tarsal plate and orbital septum is not always possible through physical examination, imaging can contribute significantly to the T-staging of eyelid tumors, improving treatment planning and therefore will have a positive impact on both patients' short-term morbidity and longtime outcome.

Clinical value and impact of MR imaging of the eyelid

This research in the eyelid also changed clinical practice in LUMC. Previous to this research, an MRI was only made to check whether an eyelid tumor was invading the orbit. This study allowed a better understanding of the potential role of MRI in the evaluation of an eyelid lesion. In particular, we now know that most eyelid layers are visible on MRI, making the evaluation of the local extension of an eyelid tumor in the eyelid possible, which was previously impossible. It also made it possible to evaluate orbital invasion with more confidence. As a consequence, we more regularly perform MRI for evaluation of an eyelid tumor, to define its extension and sometimes for the diagnosis. Regarding the diagnosis, at the moment, the role of MRI is mainly to differentiate a benign from a malignant tumor, and only in a few cases being able to make the specific diagnosis.

Our MR images of the eyelid also caught the attention of foreign centers, with current interest in including them in the new edition of the WHO Classification of Tumours of the Eye book.

Future perspectives

The accuracy of MRI to evaluate the local extension of an eyelid tumor should be further assessed in a large group of eyelid tumors.

Finally, a good characterization with MRI of the most common benign and malignant eyelid tumors seems also important, as occasionally, mainly in children, the diagnosis of an eyelid mass is the main question for the MRI.

CONCLUSION

The work described in this thesis opened new perspectives in the diagnosis of several ophthalmologic pathologies, allowing for better treatment results and therefore contributing for the patient's well-being. Moreover, together with the previous MR works on retinoblastoma [12], it made a step in the history of ophthalmologic imaging, as it brought MR-imaging of the eye and of the eyelid to the same level as the rest of the body.

The increasing number of requests of ocular and eyelid MRI scans urge further subspecialization within neuroradiologists, as specific knowledge is required, also regarding ophthalmic imaging techniques, with close work with the ophthalmologists and related specialisms being warranted. Furthermore, it is important to further better combine the information radiologists get from MRI with the information the ophthalmologists get from the optical imaging techniques, in particular with fundoscopy and fluorescein angiography. It is my wish to continue to deepen our knowledge of eye, eyelid and orbital imaging. The current MR images of the orbital segments of the optic nerves are suboptimal and could be focus of improvement, perhaps by extending our eyelid 3T MRI protocol. This protocol uses two surface coils which provide a better SNR posterior to the globe. However, similar to our eye 3T MRI protocol special attention will be needed for the eye movement artefacts. The eyelid 3T MRI protocol should subsequently be compared with our current orbit 3T MRI protocol, to check for added value in terms of SNR, but also to evaluate whether sufficient resolution is achieved at the level of the cavernous sinuses. An improved MRI protocol, together with further knowledge of specific diffusion and perfusion characteristics of the different orbital tumors and orbital inflammation, would further help in the differential diagnosis of orbital masses.

It is also my wish to continue to disseminate our knowledge, so that worldwide other centers can improve their clinical practice in this area. Ideally, international workgroups could be created to improve imaging protocols and develop best practices regarding the diagnosis of different ophthalmologic areas and diseases.

REFERENCES

1. Tang MCY, Jaarsma-Coes MG, Ferreira TA, Fonk LZ-G, Marinkovic M, Luyten GPM, Beenakker J-WM. A comparison of 3T and 7T MRI for the clinical evaluation of uveal melanoma. *J Magn Reson Imaging*. 2022 May;55(5):1504-1515.
2. Jaarsma-Coes MG, Ferreira TAG, van Haren GR, Marinkovic M, Beenakker J-WM. MRI enables accurate diagnosis and follow-up in uveal melanoma patients after vitrectomy. *Melanoma Res*. 2019 Dec;29(6):655-659.
3. Jaarsma-Coes MG, Ferreira TA, Marinkovic M, Vu THK, van Vucht L, van Haren GR, Rodrigues MF, Klaver YLB, Verbist BM, Luyten GPM, Rasch CRN, Beenakker J-WM. Comparison of magnetic resonance imaging-based and conventional measurements for proton beam therapy of uveal melanoma. *Ophthalmol Retina*. 2022 Jul 13;S2468-6530(22)00339-6.
4. OPTIC workgroup meeting, PTCOG, Miami, 2022.
5. Lemke AJ, Hosten N, Bornfeld N, Bechrakis NE, Schüller A, Richter M, Stroszczynski C, Felix R. Uveal melanoma: correlation of histopathologic and radiologic findings by using thin-section MR imaging with a surface coil. *Radiology* 1999 Mar;210(3):775-783.
6. Berus T, Halon A, Markiewicz A, Orłowska-Heitzman J, Romanowska-Dixon B, Donizy P. Clinical, histopathological and cytogenetic prognosticators in uveal melanoma – a comprehensive review. *Anticancer Res*. 2017 Dec;37(12):6541-6549.
7. Kamrava M, Sepahdari AR, Leu K, Wang P-C, Roberts K, Demanes DJ, McCannel T, Elligson BM. Quantitative multiparametric MRI in uveal melanoma: increased tumor permeability may predict monosomy 3. *Neuroradiology*. 2015 Aug;57(8):833–840.
8. Foti PV, Longo A, Reibaldi M, Russo A, Privitera G, Spatola C, Raffaele L, Salamone V, Farina R, Palmucci S, Musumeci A, Caltabiano R, Ragusa M, Mariotti C, Avitabile T, Milone P, Ettorre GC. Uveal melanoma: quantitative evaluation of diffusion-weighted MR imaging in the response assessment after proton-beam therapy, long-term follow-up. *Radiol Med*. 2017 Feb;122(2):131–139.
9. Fonk LG, Ferreira TA, Webb AG, Luyten GPM, Beenakker J-WM. The economic value of MR-imaging for uveal melanoma. *Clin Ophthalmol*. 2020 Apr 28;14:1135–1143.
10. Integraal Kankercentrum Nederland (IKNL).
11. de Graaf P, Barkhof F, Moll AC, Imhof SM, Knol DL, van der Valk P, Castelijns JA. Retinoblastoma: MR imaging parameters in detection of tumor extent. *Radiology*. 2005 Apr;235(1):197-207.
12. de Graaf P, Görlicke S, Rodjan F, Galluzzi P, Maeder P, Castelijns JA, Brisse HJ, European Retinoblastoma Imaging Collaboration (ERIC). Guidelines for imaging retinoblastoma: imaging principles and MRI standardization. *Pediatr Radiol*. 2012 Jan;42(1):2-14.
13. de Graaf P, Pouwels PJW, Rodjan F, Moll AC, Imhof SM, Knol DL, Sanchez E, van der Valk P, Castelijns JA. Single-shot turbo spin-echo diffusion-weighted imaging for retinoblastoma: initial experience. *Am J Neuroradiol*. 2012 Jan;33(1):110-118.
14. Rodjan F, de Graaf P, van der Valk P, Moll AC, Kuijer JPA, Knol DL, Castelijns JA, Pouwels PJW. Retinoblastoma: value of dynamic contrast-enhanced MR imaging and correlation with tumor angiogenesis. *AJNR Am J Neuroradiol*. 2012 Dec;33(11):2129-2135.

15. Brisse HJ, de Graaf P, Galluzzi P, Cosker K, Maeder P, Göricke S, Rodjan F, de Jong MC, Savignoni A, Aerts I, Desjardins L, Moll AC, Hadjistilianou T, Toti P, van der Valk P, Castelijns JA, Sastre-Garau X, European Retinoblastoma Imaging Collaboration (ERIC). Assessment of early-stage optic nerve invasion in retinoblastoma using high-resolution 1.5 Tesla MRI with surface coils: a multicentre, prospective accuracy study with histopathological correlation. *Eur Radiol.* 2015 May;25(5):1443-1452.
16. de Jong MC, de Graaf P, Brisse HJ, Galluzzi P, Göricke SL, Moll AC, Munier FL, Popovic MB, Moulin AP, Binaghi S, Castelijns JA, Maeder P, European Retinoblastoma Imaging Collaboration (ERIC). The potential of 3T high-resolution magnetic resonance imaging for diagnosis, staging, and follow-up of retinoblastoma. *Surv Ophthalmol.* 2015 Jul-Aug;60(4):346-355.
17. Sepahdari AR, Politi LS, Aakalu VK, Kim HJ, Razek AAKA. Diffusion-weighted imaging of orbital masses: multi-institutional data support a 2-ADC threshold model to categorize lesions as benign, malignant, or indeterminate. *Am J Neuroradiol.* 2014 Jan;35(1):170-175.
18. Lemke AJ, Hosten N, Wiegel T, Prinz RD, Richter M, Bechrakis NE, Foerster PI, Felix R. Intraocular metastases: differential diagnosis from uveal melanomas with high-resolution MRI using a surface coil. *Eur Radiol.* 2001;11(12):2593-2601.
19. Fleury E, Trnková P, Erdal E, Hassan M, Stoel B, Jaarsma-Coes M, Luyten G, Herault J, Webb A, Beenakker J-W, Pignol J-P, Hoogeman M. Three-dimensional MRI-based treatment planning approach for non-invasive ocular proton therapy. *Med Phys.* 2021 Mar;48(3):1315-1326.
20. Jaarsma-Coes MG, Ferreira TA, van Houdt PJ, van der Heide UA, Luyten GPM, Beenakker J-WM. Eye-specific quantitative dynamic contrast-enhanced MRI analysis for patients with intraocular masses. *MAGMA.* 2022 Apr;35(2):311-323.
21. Hiwatashi A, Togao O, Yamashita K, Kikuchi K, Kamei R, Yoshikawa H, Takemura A, Honda H. Diffusivity of intraorbital lymphoma vs inflammation: comparison of single shot turbo spin echo and multishot echo planar imaging techniques. *Eur Radiol.* 2018 Jan;28(1):325-330.
22. Lecler A, Duron L, Zmuda M, Zuber K, Bergès O, Putterman M, Savatovsky J, Fournier L. Intravoxel incoherent motion (IVIM) 3T MRI for orbital lesion characterization. *Eur Radiol.* 2021 Jan;31(1):14-23.
23. Sun B, Song L, Wang X, Li J, Xian J, Wang F, Tan P. Lymphoma and inflammation in the orbit: diagnostic performance with diffusion-weighted imaging and dynamic contrast-enhanced MRI. *J Magn Reson Imaging.* 2017 May;45(5):1438-1445.
24. Xu X-Q, Hu H, Liu H, Wu J-F, Cao P, Shi H-B, Wu F-Y. Benign and malignant orbital lymphoproliferative disorders: differentiating using multiparametric MRI at 3.0T. *J Magn Reson Imaging.* 2017 Jan;45(1):167-176.
25. Hu H, Xu X-Q, Liu H, Hong X-N, Shi H-B, Wu F-Y. Orbital benign and malignant lymphoproliferative disorders: differentiation using semi-quantitative and quantitative analysis of dynamic contrast-enhanced magnetic resonance imaging. *Eur J Radiol.* 2017 Mar;88:88-94.

Nederlandse samenvatting
Acknowledgements
List of publications
Curriculum Vitae



NEDERLANDSE SAMENVATTING

Dit proefschrift beschrijft de ontwikkeling van speciale hoge-resolutie MRI (magnetic resonance imaging) -protocollen voor evaluatie van het oog en het ooglid en de toepassing ervan in de karakterisering van het oogmelanoom en de anatomie van het ooglid. Verder richt het zich op de karakterisering van orbitale inflammatoire aandoeningen op MRI en CT (computed tomography), het onderscheiden tussen orbitale inflammatie, orbitale tumoren en infectie, én het onderscheiden van tussen de meest voorkomende orbitale inflammatoire ziekten.

Het oplossen van klinische problemen vormt de kern van de in dit proefschrift beschreven onderzoek. De resultaten van dit onderzoek heeft de diagnose en behandeling van specifieke ziekten verbeterd, met een duidelijk voordeel voor de patiënt. Dit kan alleen goed gebeuren binnen een multidisciplinair team, zoals wij dat hebben, waarbij de verschillende inbreng van de verschillende medische specialismen, die elkaar aanvullen, van het grootste belang is.

Oogmelanoom

MRI-protocol voor het oog

In **hoofdstuk 2.1** is een *3T MRI-protocol voor de evaluatie van het oog* ontwikkeld, na uitgebreide evaluatie van verschillende sequenties bij 9 patiënten met oogmelanoom. Het protocol maakt gebruik van een oppervlaktespoel en bestaat uit MS (multi-slice) 2 mm 2D sequenties (T1, T1 met vetsuppressie na contrast en T2) en een non-EPI (echo-planar imaging) TSE (turbo spin-echo) DWI (diffusion-weighted imaging) (b-waarden van 0 en 800 s/mm²) en ADC (apparent diffusion coefficient), verkregen loodrecht op de hoofdas van de tumor. Het omvatte ook isotrope 3D TSE-sequenties (T1, T1 met vetsuppressie voor en na contrast en T2) en een DCE (dynamic contrast-enhanced) -sequentie, verkregen in het axiale vlak zonder angulatie. De MS 2 mm 2D sequenties hebben de hoogste “in-plane” resolutie en zijn daarom het beste voor laesie karakterisering en evaluatie van lokale uitbreiding. De isotrope 3D TSE-sequenties maken retrospectieve reconstructie in alle richtingen mogelijk, en zijn essentieel voor de beoordeling van de tumor geometrie en nauwkeurige omvangmetingen. De DWI- en PWI (perfusion-weighted imaging) -sequenties helpen bij de differentiële diagnose. Daarnaast biedt deze techniek mogelijk prognostische informatie en maken mogelijk een eerdere beoordeling van de tumorrespons op radiotherapie mogelijk dan echografie. Over het algemeen levert dit 3T MRI-protocol voor het oog hoge resolutie MR-beelden van oogmelanoom, die van cruciaal belang zijn voor een betere diagnose, planning van de behandeling en follow-up. Daarnaast kan het ook worden gebruikt voor andere intra-oculaire laesies.

Voordat we oogmelanoom op 3T gingen evalueren, beoordeelden we ze op 7T MRI vanwege de hoge veldsterkte, waarvoor we ook een *7T MRI-protocol om het oog te evalueren* hadden

ontwikkeld. Onze onderzoeksgroep vergeleek prospectief de diagnostische prestaties van 7T en 3T om het oog en oogmelanoom te evalueren. Enerzijds konden met 7T onder optimale omstandigheden beelden van de hoogste kwaliteit worden verkregen. Anderzijds komen op 7T ernstige artefacten die een onderzoek niet diagnostisch maken vaker voor.

Bovendien heeft onze onderzoeksgroep, zowel voor 3T als voor 7T, een *MRI-protocol om ogen met siliconenolie te evalueren* ontwikkeld, waardoor sommige patiënten met een oogmelanoom hun oog en gezichtsvermogen konden behouden. Voordat dit specifieke MRI-protocol was ontworpen, zou het oog van deze patiënten over het algemeen worden verwijderd, omdat de diagnose, de planning van de behandeling en de daaropvolgende follow-up van oogmelanoom onmogelijk zouden zijn, omdat de aanwezigheid van intra-oculaire siliconeolie de beeldvorming met echografie verhindert.

Ten slotte heeft onze onderzoeksgroep, samen met het Holland PTC, een *3T MRI-protocol voor de evaluatie van ogen vóór de protonentherapie* ontwikkeld. Dit specifieke protocol maakt een nauwkeurige beoordeling mogelijk van de clip-tumor afstanden en van de oogbolafmetingen, beide belangrijk bij de protonentherapie planning. Bovendien werden deze MRI-metingen vergeleken met conventionele methodes. MRI bleek minder nauwkeurig te zijn bij de evaluatie van de clip-tumor afstanden in het geval van vlakke oogmelanomen. MRI was echter betrouwbaarder bij de evaluatie van de ooglengte en bij het meten van de clip-tumor afstanden van anterieur gelegen en paddenstoel-vormige tumoren. MR-beeldvorming van deze patiënten zal leiden tot een nauwkeurigere doelbepaling, waardoor de toxiciteit mogelijk wordt verminderd en de kans op behoud van het gezichtsvermogen toeneemt. Hoewel wij het eerste centrum waren dat een MRI opnam voor alle oculaire protonentherapie patiënten, nemen nu meer centra MRI op in hun workflow en gebruiken zij protocollen die op de onze zijn gebaseerd.

MRI kenmerken van oogmelanoom

Voor het onderzoek beschreven in **hoofdstuk 2.2** werden de anatomische en functionele MRI kenmerken van 42 oogmelanomen beoordeeld. De MRI kenmerken werden vergeleken met fundoscopie en echografie, en op 14 verwijderde ogen met histopathologie.

Oogmelanoom met complexe tumorvormen, zoals een paddenstoel configuratie, moeten worden herkend omdat zij speciale aandacht verdienen bij de planning van de radiotherapie. Er werd een significant verband gevonden tussen de signaalintensiteit op T1 en de pigmentatie op histopathologie. De ADC van oogmelanomen was $1,16 \pm 0,26 \times 10^{-3} \text{ mm}^2/\text{s}$. Twee derde van oogmelanomen had een wash-out en de overige een plateau perfusie time-intensity curve (TIC). De gemiddelde peak intensity (PI) van oogmelanomen was 1,62. Kennis van de ADC- en perfusiekenmerken is waardevol voor de differentiële diagnose met andere intra-oculaire massas. Bovendien lijkt PWI veelbelovend voor de identificatie van oogmelanoom

met een hoger risico op metastase, die mogelijk kan dienen als vervanging voor een biopsie bij patiënten die een oogsparende behandeling ondergaan.

Beoordeling van de tumorgrootte is essentieel voor de keuze van de behandelingsmodaliteit en de planning van radiotherapie. MRI was beperkt in de beoordeling van de basale diameter van vlakke tumoren, aangezien MRI de tendens had de grootte van de basale diameter te onderschatten als gevolg van onduidelijke tumormarges. In vergelijking met MRI heeft echografie de neiging om de tumorgrootte te overschatten, waarbij grotere tumor prominentie en grootste basale diameter worden getoond.

De lokale uitbreiding van een oogmelanoom moet worden beoordeeld, zodat er in het behandelplan rekening mee kan worden gehouden. Bovendien wordt de aanwezigheid van extraoculaire groei en invasie van de oogzenuw geassocieerd met een verhoogd percentage van orbitaal recidief en een slechtere prognose. MRI was goed in het diagnosticeren van betrokkenheid van het corpus ciliare, extra-sclerale uitbreiding en oogzenuw-invasie, maar in tegenstelling tot wat eerder is gerapporteerd, beperkt in het identificeren van sclerale infiltratie.

MRI follow-up van oogmelanoom na brachytherapie en protonetherapie

Onze onderzoeksgroep evalueert momenteel de waarde van DWI en PWI in de follow-up van oogmelanoom na brachytherapie en protonetherapie. De voorlopige resultaten tonen vooral PWI gunstige veranderingen vóór volumeveranderingen, waardoor de respons van oogmelanoom op radiotherapie eerder kan worden beoordeeld dan met de conventionele echografie. Dit is geruststellend voor zowel de clinici als de patiënten.

Klinische waarde en impact van MRI van oogmelanoom

MRI maakt beelden van hoge kwaliteit mogelijk van het oog en oogmelanoom. Het is echter duurder dan echografie en het leek relevant te beoordelen of de extra kosten van een MRI economisch voordeel of verandering in de optimale behandeling zouden opleveren. Onze onderzoeksgroep evalueerde dit en toonde aan dat een extra MRI kosteneffectief is voor patiënten bij wie twijfel bestaat over de nauwkeurigheid van de echografie-metingen, als de tumor iets te groot lijkt voor brachytherapie en bij oogmelanoom-patiënten die niet met echografie kunnen worden geëvalueerd en anders enucleatie zouden ondergaan. Bovendien heeft MRI een toegevoegde waarde voor de kwaliteit van de zorg, omdat het voor sommige patiënten mogelijk maakt een behandelingsmodaliteit toe te passen die meer van hun gezichtsvermogen spaart.

Het LUMC is het nationale referentiecentrum voor oogmelanoom in Nederland en ontvangt ongeveer 220 oogmelanomen per jaar. De evaluatie van oogmelanoom met MRI bracht verschillende voordelen met zich mee en heeft de klinische praktijk in ons ziekenhuis veranderd. Vóór ons onderzoek kreeg een oogmelanoom-patiënt zelden een MRI.

Tegenwoordig maken we vóór de behandeling een MRI als er twijfel is over de diagnose, en voor de planning van de behandeling. Wij maken ook een MRI in de vroege follow-up na radiotherapie om de respons op de behandeling te beoordelen, en in de follow-up na de behandeling wanneer een recidief van het oog of orbitaal wordt vermoed. Gemiddeld maken wij 3 tot 4 MRI-scans per week. In het algemeen heeft MRI de precisie van de oogmelanoom-behandeling verhoogd.

Ons 3T MRI-protocol voor ogen heeft ook de belangstelling gewekt van verschillende andere buitenlandse centra, en is in samenwerking met Philips nu online beschikbaar. Bovendien zijn onze oogmelanoom-resultaten worden opgenomen in de nieuwe editie van het “WHO Classification of Tumours of the Eye” boek.

Toekomstperspectieven

Momenteel werken wij aan: verdere verbetering van de differentiële diagnose van oculaire massas, door evaluatie van de MRI kenmerken van andere goedaardige en kwaadaardige intra-oculaire massas; de ontwikkeling van een 3D MRI-gebaseerde oculaire protonentherapie planning, zonder de noodzaak om markers te plaatsen; en verdere evaluatie van de waarde van PWI voor de identificatie van oogmelanoom met een hoger risico op metastase, aangezien het zou kunnen dienen als vervanging van een biopsie bij patiënten die een oogsparende behandeling ondergaan.

Orbitale inflammatoire aandoeningen

In **hoofdstuk 3.1** werden de CT- en MRI kenmerken van scleritis retrospectief geëvalueerd in 11 patiënten waarin CT- en/of MRI werd verricht tijdens de actieve fase van de ziekte. De beeldvormende bevindingen van scleritis waren aankleuring van de sclera, verdikking van de sclera en focale perisclerale cellulitis. Ten opzichte van CT bleek MRI het nuttigste onderzoek voor de diagnose van scleritis, maar scleritis kon ook nauwkeurig worden gediagnosticeerd op CT. Scleritis is bijna altijd van inflammatoire oorsprong, of idiopathisch of in de context van een systemische inflammatoire ziekte. Scleritis kan geïsoleerd voorkomen of in combinatie met andere orbitale afwijkingen. Het is belangrijk de diagnose niet te verwarren met die van een tumor. Aanwijzingen voor de inflammatoire (versus neoplastische) aard van het proces zijn de aanwezigheid van pijn, cellulitis en de specifieke locatie van de sclera.

In **hoofdstuk 3.2** is een literatuurstudie verricht naar de beeldvormingsprotocollen en de kenmerken van orbitale inflammatoire aandoeningen. MRI is de modaliteit bij uitstek voor de evaluatie van orbitale inflammatoire aandoeningen vanwege het superieure contrast en spatiele resolutie en de mogelijkheid om functionele beelden te genereren zoals DWI en PWI, die van cruciaal belang zijn om goedaardige van kwaadaardige laesies te onderscheiden. De specifieke radiologische kenmerken van inflammatie van de verschillende orbitale structuren, zoals scleritis,

uveitis, dacryoadenitis, perineuritis en neuritis optica, myositis en orbitale cellulitis, werden beschreven. Voorts werden de beeldvormingskenmerken van specifieke ontstekingsziekten gepresenteerd, zoals die van idiopathische orbitale inflammatie (IOI), sarcoidose, schildkliergeassocieerde orbitopathie (ziekte van Graves), immunoglobuline G4-gerelateerde ziekte (IgG4 RD), granulomatose met polyangiitis (Wegener-granulomatose), idiopathische scleroserende orbitale inflammatie (ISOI) en de ziekte van Erdheim-Chester. Ten slotte werden verschillende beeldvormende en klinische aanwijzingen gecombineerd in een beslisboom, die het mogelijk maakt een orbitale laesie te herkennen als inflammatoir, en te differentiëren van een infectie of tumor. Vervolgens hebben wij aangetoond dat het gevonden radiologische patroon in de orbita kan wijzen op een onderliggende inflammatoire ziekte of ten minste de differentiële diagnose ervan kan verkorten. In het algemeen stellen deze overwegingen de behandelend arts in staat een adequate behandeling vast te stellen en kan soms een biopsie worden voorkomen.

Klinische waarde en impact van MRI bij inflammatoire aandoeningen

Dit onderzoek naar orbitale inflammatoire aandoeningen heeft de klinische praktijk in ons ziekenhuis veranderd. Nu kunnen de oogartsen, als de MRI-kenmerken van een orbitale laesie wijzen op inflammatie, de klinische symptomen en laboratoriumresultaten consistent zijn en als de laesie niet gemakkelijk toegankelijk is met een biopsie, overwegen een medische behandeling te starten zonder histopathologische bevestiging. Dit is minder ingrijpend voor de patiënt en minder kostbaar.

Toekomstperspectieven

In de nabije toekomst moet de evaluatie van de specifieke diffusie- en perfusiekenmerken van de verschillende orbitale tumoren en orbitale inflammatoire aandoeningen nog aandacht krijgen, omdat dit verder zou helpen bij de differentiële diagnose van orbitale massa's.

Ooglid

In **hoofdstuk 4.1** werd een retrospectieve evaluatie van de normale anatomie van het ooglid, in termen van identificatie van de ooglidlagen, op MRI en CT uitgevoerd bij 38 normale oogleden. Voorts werd bij drie ooglidtumoren de tumoruitbreiding beoordeeld en gevalideerd met histopathologie. Ondanks de kleine omvang van de verschillende ooglidlagen en hoewel beeldvorming van het ooglid een uitdaging is vanwege susceptibiliteit en bewegingsartefacten, is de identificatie van de meeste ooglidstructuren mogelijk met een geoptimaliseerd MRI-protocol, inclusief het gebruik van een oppervlaktespoel, en in mindere mate met CT. MRI is de modaliteit bij uitstek om de uitbreiding van een ooglidtumor te evalueren, dankzij de hoge resolutie en de diffusie- en perfusiegevoegen beeldvorming die helpt om onderscheid te maken tussen de kwaadaardige tumor en omringende ontsteking. CT moet vooral worden gebruikt als aanvullende techniek bij de evaluatie van botinvasie. Aangezien de beoordeling van de tumorinvasie van het tarsus en het orbitale septum niet altijd mogelijk is via lichamelijk onderzoek, kan beeldvorming

een belangrijke bijdrage leveren aan de T-stadiëring van ooglidtumoren, waardoor de planning van de behandeling wordt verbeterd en dus een positief effect kan hebben op zowel de korte termijn morbiditeit als het lange termijn resultaat van patiënten.

Klinische waarde en impact van MRI van het ooglid

Dit onderzoek maakte de evaluatie van de lokale uitbreiding van een ooglid tumor in het ooglid mogelijk, wat voorheen onmogelijk was. Het maakte het ook mogelijk de orbitale invasie met meer vertrouwen te evalueren. Als gevolg daarvan voeren wij vaker MRI uit voor de evaluatie van ooglid tumoren. Onze MR-beelden van het ooglid trokken ook de aandacht van buitenlandse centra, en zijn opgenomen in de nieuwe editie van het “WHO Classification of Tumours of the Eye” boek.

Toekomstperspectieven

De nauwkeurigheid van MRI om de lokale uitbreiding van een ooglid tumor te evalueren moet verder worden geëvalueerd in een grotere groep ooglid tumoren. Ten slotte lijkt ook een goede karakterisering met MRI van de meest voorkomende goedaardige van kwaadaardige ooglidtumoren van belang, omdat soms, vooral bij kinderen, de diagnose van een ooglidmassa de primaire reden is voor de MRI.

Conclusie

Het in dit proefschrift beschreven werk opende nieuwe perspectieven in de diagnose van verschillende oogheelkundige ziekten, waardoor betere behandelingsresultaten mogelijk zijn en dus wordt bijgedragen aan het welzijn van de patiënt. Samen met de eerdere MR-werkzaamheden voor het retinoblastoom betekende het bovendien een stap in de geschiedenis van de oftalmologische beeldvorming, omdat het de MRI van het oog en het ooglid op hetzelfde niveau bracht als de rest van het lichaam.

Het toenemende aantal aanvragen voor oculaire en ooglid-MRI-scans noopt tot verdere subspecialisatie bij neuroradiologen, omdat het specifieke kennis vereist. Verder is het van belang om de informatie die radiologen uit MRI halen nog beter te combineren met de informatie die oogartsen halen uit de optische beeldvormingstechnieken, met name met fundoscopie en fluoresceïne-angiografie.

Het is mijn wens om onze kennis van oog-, ooglid- en orbitale beeldvorming te blijven verdiepen, maar ook om onze kennis te blijven verspreiden, zodat wereldwijd andere centra hun klinische praktijk op dit gebied kunnen verbeteren. Idealiter zouden internationale werkgroepen kunnen worden opgericht om beeldvormingsprotocollen te verbeteren en beste praktijken te ontwikkelen met betrekking tot de diagnose van verschillende oogheelkundige gebieden en ziekten.

ACKNOWLEDGEMENTS

I am grateful to several people who, directly or indirectly, contributed to this work.

Jan-Willem, thank you for bringing the different medical specialties together in our research group, which is of utmost importance, and I appreciate your dedication, enthusiasm, initiative and flexibility. I thank you for your always availability and help, and I believe we make a good and complementary team.

Prof. Webb, dear Andrew, during most of my PhD trajectory you were the head of the C.J. Gorter MRI Center, so no wonder there is such a good and inspiring atmosphere within this large research group. Thank you for your orientation, flexibility and of course for your good vibe.

Prof. Luyten, dear Gre, how I admire you as an ophthalmologist, and value our discussions about clinical cases, where your opinion is important for my imaging interpretation. Thank you for the trust and support you had given me, and lately, you also impressed me as a culinary chef.

I want to thank Mark van Buchem for suggesting the uveal melanoma research and the Radiology Department of LUMC for facilitating me doing this PhD.

I would like to thank my colleagues from Ophthalmology, Radiology, Pathology and Radiation Oncology Departments of LUMC.

Marina, Stijn, Khanh and Martine, just as with Gre, your clinical input and knowledge is so valuable to me, and made me grow as an orbit and eye radiologist. And, I truly value your openness for new imaging modalities.

Research team co-workers from the C.J. Gorter MRI Center, including Myriam, Lorna, Michael and Lisa. I appreciated your help so much, with scanning the patients, image analysis and solving technical issues, and the good atmosphere.

Guido, Wouter and, Pascal Koolhof and Paul de Bruin from Philips, your help was so important to achieve our beautiful MRI protocols. I would also like to acknowledge our MRI technicians: Benjamin, Esther, Fred, Jeannette, Mani, Olaf, Sonja and Tina, thank you for your openness to learning to perform the eye scans which are often not as straightforward to plan as many other anatomies.

Berit, thank you for making part of our research team, and for your important role in the pre-proton beam therapy planning of uveal melanomas at the HollandPTC.

Menno, I appreciate your motivation and easiness to learn new things, and helping in the evaluation of uveal melanoma MRIs.

Acknowledgements

Rob and Sjoerd, how I value your histopathology input in our research, making it so much more complete.

Gerrit, I thank you for your technical support in the development of the articles.

Mariana Diogo, Paulo Saraiva and Carolina Pinheiro, I am grateful for your precious collaboration in some of the articles. Paulo Saraiva, I would have never become the Neuro and Head and Neck radiologist I am today had I not had you as my tutor. Your knowledge and accuracy always impressed me, and still do.

Of course, I am grateful to all patients that accepted to participate in the different studies.

Alexandra Borges, thank you for in 2008 inviting me to give a lecture about MRI of the orbit and eye on the Erasmus Course on Magnetic Resonance Imaging, which was held in Lisbon. It was definitely the beginning of my subspecialization in orbital imaging.

And I would never have finished my thesis without the support and love from my family and friends.

My education and my principles I owe to my dear mother and father, and I am so grateful for their always love and support.

Herman and Josien, thank you for your support and motivation. Dear Herman, I am so sorry you are not with us anymore to be able to attend my PhD Defense, as you have certainly been my greatest PhD admirer!

Catarina and Ana, thank you for your wise advice and for motivating me to finish this thesis. Sara, I am so grateful you designed the Cover of my PhD book, including what will be my logotype in the future. To my brother Mario, thanks for your critical help. Manuel, thank you for helping with the design of my PhD book.

To my husband August, whose love and support are making it easier to live a happy life. And finally, to my sons Lorentz, Martim and Simon, who are so precious.

LIST OF PUBLICATIONS

1. Matias S, Ferreira T, Vilela P, Secca M, Goulão A. Magnetic resonance imaging of aqueductal flow in patients with normal hydrocephalus pressure. *Acta Med Port.* 2001 Jan-Feb;14(1):13-20.
2. Ferreira TG, Guarda CS, Monteiro JPO, Fonseca MJC, Saraiva PF, Constâncio AG. Corpus callosum agenesis. *Rev Neurol.* 2003 Apr 16-30;36(8):701-706.
3. Ferreira T, Shayestehfar B, Lufkin R. Narrow, duplicated internal auditory canal. *Neuroradiology.* 2003 May;45(5):308-310.
4. Ferreira T. Comments on Castelijns and van den Brekel: imaging of lymphadenopathy in the neck. *Eur Radiol.* 2003 Sep;13(9):2236.
5. Ferreira T, Verbist B, van Buchem M, van Osch T, Webb A. Imaging the ocular motor nerves. *Eur J Radiol.* 2010 May;74(2):314-322.
6. Beenakker J-WM, Ferreira TA, Soemarwoto KP, Genders SW, Teeuwisse WM, Webb AG, Luyten GPM. Clinical evaluation of ultra-high-field MRI for three-dimensional visualisation of tumour size in uveal melanoma patients, with direct relevance to treatment planning. *MAGMA.* 2016 Jun;29(3):571-577.
7. Diogo MC, Jager MJ, Ferreira TA. CT and MR imaging in the diagnosis of scleritis. *Am J Neuroradiol.* 2016 Dec;37(12):2334-2239.
8. Ferreira TA, Saraiva P, Genders SW, van Buchem M, Luyten GPM, Beenakker J-W. CT and MR imaging of orbital inflammation. *Neuroradiology.* 2018 Dec;60(12):1253-1266.
9. Ferreira TA, Fonk LG, Jaarsma-Coes MG, van Haren GGR, Marinkovic M, Beenakker J-WM. MRI of uveal melanoma. *Cancers (Basel).* 2019 Mar 17;11(3):377.
10. Jaarsma-Coes MG, Ferreira TA, Luyten GPM, Beenakker J-WM. Reaction on "Ocular ultrasound versus MRI in the detection of extrascleral extension in a patient with choroidal melanoma". *BMC Ophthalmol.* 2019 Aug 27;19(1):193.
11. Jaarsma-Coes MG, Ferreira TAG, van Haren GR, Marinkovic M, Beenakker J-WM. MRI enables accurate diagnosis and follow-up in uveal melanoma patients after vitrectomy. *Melanoma Res.* 2019 Dec;29(6):655-659.
12. Ferreira TA, Pinheiro CF, Saraiva P, Jaarsma-Coes MG, van Duinen SG, Genders SW, Marinkovic M, Beenakker J-WM. MR and CT imaging of the normal eyelid and its application in eyelid tumors. *Cancers (Basel).* 2020 Mar 12;12(3): 658.
13. Fonk LG, Ferreira TA, Webb AG, Luyten GPM, Beenakker J-WM. The economic value of MR-imaging for uveal melanoma. *Clin Ophthalmol.* 2020 Apr 28;14:1135-1143.
14. Jaarsma-Coes MG, Ferreira TA, van Houdt PJ, van der Heide UA, Luyten GPM, Beenakker J-WM. Eye-specific quantitative dynamic contrast-enhanced MRI analysis for patients with intraocular masses. *MAGMA.* 2022 Apr;35(2):311-323.
15. Tang MCY, Jaarsma-Coes MG, Ferreira TA, Fonk LZ-G, Marinkovic M, Luyten GPM, Beenakker J-WM. A comparison of 3T and 7T MRI for the clinical evaluation of uveal melanoma. *J Magn Reson Imaging.* 2022 May;55(5):1504-1515.
16. Ferreira TA, Jaarsma-Coes MG, Marinkovic M, Verbist B, Verdijk RM, Jager MJ, Luyten GPM, Beenakker J-WM. MR imaging characteristics of uveal melanoma with histopathological validation. *Neuroradiology.* 2022 Jan;64(1):171-184.

List of publications

17. Islamaj E, van Vught L, Jordaan-Kuip CP, Vermeer KA, Ferreira TA, De Waard PWT, Lemij HG, Beenakker J-WM. Magnetic resonance imaging reveals possible cause of diplopia after Baerveldt glaucoma implantation. *PLoS One*. 2022 Oct 20;17(10).
18. Jaarsma-Coes MG, Ferreira TA, Marinkovic M, Vu THK, van Vught L, van Haren GR, Rodrigues MF, Klaver YLB, Verbist BM, Luyten GPM, Rasch CRN, Beenakker J-WM. Comparison of Magnetic Resonance imaging-based and conventional measurements for proton beam therapy of uveal melanoma. *Ophthalmol Retina*. 2023 Feb;7(2):178-188.

CURRICULUM VITAE

Teresa A G Gonçalves Ferreira was born in Lisbon, Portugal on January 28, 1972.

From 1977 until 1986 she attended most of her primary and secondary school at St. Julian's School in Carcavelos, Portugal.

In 1990 she started her medical training at the Medical University of Lisbon, Portugal, which she finished in 1995.

In 1998 she entered the neuroradiology residency programme at Hospital Garcia de Orta in Almada, Portugal (Prof Dr A Goulao and P Saraiva). In 1999, while being a resident in neuroradiology, she finished the United States Medical Licencing Examination (USMLE). In 2001-2002 she spent part of her neuroradiology training as a visiting fellow at the University of California, Los Angeles, USA (Prof Dr R Lufkin and Prof Dr P Vilablanca). In 2003, after completing her residency, she started working as a neuroradiologist in Hospital Garcia de Orta, Almada, Portugal, until 2005.

Due to a special interest in neurosciences, already in 1993, during her university studies, she began teaching neuroanatomy at the Medical University of Lisbon, Portugal, which she did until 2005. Later, from 2000 until 2003 she was also appointed as the neuroanatomy teacher in the Speech Therapy Course of the Egas Moniz University in Almada, Portugal.

In 2006 she moved to The Netherlands and started working as a neuroradiologist in LUMC, Leiden, where, from 2008 until 2012, she joined the radiology residency (Prof Dr JL Bloem and Dr Šramek). Since 2012 she is appointed as a radiologist in LUMC with a subspecialization in neuroradiology, and in 2013 she took the European Board in Head and Neck Radiology Diploma (EBiHNR) examination.

In 2015 she started working in close cooperation with the Ophthalmology Department, under the supervision of Dr J-W M Beenakker, Prof Dr G Luyten and Prof Dr A Webb, being involved in research projects, which culminated in this thesis.

She is married to August Brester and they have three sons: Lorentz, Martim and Simon.

